A Review of Multimaterial Additively Manufactured Electronics and 4-D Printing/Origami Shape-Memory Devices: Design, Fabrication, and Implementation

This article presents a comprehensive review of the emerging 3-D/4-D printing and origami techniques using multimaterial (conductive and dielectric materials) and shape-memory materials for designing functional electronic components and devices.

By Yang Yang, *Senior Member IEEE*, Zhiwei Yin, *Graduate Student Member IEEE*,
Xuyi Zhu, *Student Member IEEE*, Hani Al Jamal, *Graduate Student Member IEEE*,
Xiaojing Lv, *Member IEEE*, Kexin Hu, *Student Member IEEE*,
Marvin Joshi, *Graduate Student Member IEEE*, Nathan Wille, *Member IEEE*,
Mengze Li, *Member IEEE*, Bing Zhang, *Senior Member IEEE*, Zhen Luo,
Shlomo Magdassi, and Manos Tentzeris, *Fellow IEEE*

Yang Yang, **Zhiwei Yin**, and **Xiaojing Lv** are with the School of Electrical and Data Engineering, University of Technology Sydney, Ultimo, NSW 2007, Australia (e-mail: yang.yang.au@ieee.org).

Xuyi Zhu is with the College of Electronics and Information Engineering, Sichuan University, Chengdu 610065, China, and also with the School of Electrical and Data Engineering, University of Technology Sydney, Ultimo, NSW 2007, Australia.

Hani Al Jamal, **Kexin Hu**, **Marvin Joshi**, **Nathan Wille**, and **Manos Tentzeris** are with the School of Electrical and Computer Engineering, Georgia Institute of Technology, Atlanta, GA 30332 USA.

Mengze Li is with the School of Microelectronics, Nanjing University of Science and Technology, Nanjing 210094, China.

Bing Zhang is with the College of Electronics and Information Engineering, Sichuan University, Chengdu 610065, China.

Zhen Luo is with the School of Mechanical and Mechatronic Engineering, University of Technology Sydney, Ultimo, NSW 2007, Australia.

Shlomo Magdassi is with the Institute of Chemistry, The Hebrew University of Jerusalem, Jerusalem 91904, Israel.

ABSTRACT | Emerging additive manufacturing (AM) technologies, specifically additively manufactured electronics (AME), 4-D printing, and origami, are reshaping the design capabilities and functionalities of contemporary electronic devices. Cutting-edge 3-D/4-D printing technologies facilitate the prototyping and realization of complex electronic functions that are challenging to conventional methods. This article provides a comprehensive overview of the evolving techniques in AME, 4-D printing, and origami, employing multimaterials (conductive and dielectric materials) and shape-memory materials (SMMs) to fabricate functional electronic components and devices. Additionally, the overview delves into the state-of-the-art AME and 4-D-printed electronic components across diverse fields, including biomedical electronics, space engineering, and the advancements in the next-generation wireless communications and sensing.

KEYWORDS | 3-D-printed electronics; 4-D printing; additively manufactured electronics (AME); origami; shape-memory alloy (SMA); shape-memory polymer (SMP).

I. INTRODUCTION

The 3-D-printed electronics, also called additively manufactured electronics (AME), have received a surge of interest in recent years due to the advancement of additive manufacturing (AM) technology over the last decade. The advantages of fast prototyping, low entry costs, and in-house short-run manufacturing empower millions of startups and companies with demanding customization needs and accelerated innovation. As an emerging innovative technology and production system, AME is one of the game changers that could completely disrupt the electronics manufacturing value chain by meeting the exceptional requirements expected in the fourth industrial revolution [1]. This article distinguishes itself by discussing multimaterial 3-D printing using conductive and dielectric materials, 4-D printing with shape-memory materials (SMMs), and other origami-inspired designs.

A. History of 3-D Printing

The development history of multimaterial 3-D printing can be traced back 50 years, as shown in Fig. 1, when the 3-D prototyping concept was first introduced by David Jones in the 1974 New Scientist Column [2]. In 1981, Kodama [3] from Japan published an article on rapid prototyping technology, the first article to describe the layer-by-layer stacking method employed by 3-D printing. Three years later, Alain Le Méhauté, Olivier de Witte, and Jean Claude André applied for a patent on stereolithography (SLA), a technique that uses light to cure resin into 3-D models [4]. Almost simultaneously, Charles Hull [5] from the United States founded 3-D systems and obtained the patent for SLA, the first commercialized 3-D printing technology. Fused deposition modeling (FDM) was invented by Crump et al. [6] from the United States in 1988. FDM is a technique that uses thermoplastic materials to stack layers through a heated extruder head. Due to the open source of the patents, it has become one of the most popular and low-cost technologies, which can be implemented through a wide range of printing mechanisms and materials. In the same period, Charoo et al. [7] and Beaman and Deckard [8] invented selective laser sintering (SLS), which uses a laser beam to form powder materials into 3-D objects. After all this, in 1995, multijet modeling was further advanced into a complex process that uses multiple nozzles to print different materials or colors simultaneously [9]. Although the invented system only covers the insulator materials, it advanced the processing techniques from single-material to multimaterial printing. Motivated by the evolution of 3-D printing in insulator material, the first metallic prototype implemented by 3-D printing was announced in 1998 [10]. These technologies were all developed for rapid prototyping purposes, and they mainly used plastics, resins, or metals to create 3-D models but were not intended for electronic components or circuits.

The 3-D printing was first applied for prototyping electronic components in the early twenty-first century when access to 3-D printers became possible for researchers and engineers [11]. In the early 2000s, the AM technique could only print single-material (conductive or dielectric materials) circuit components for metal-only or dielectric-only electronic devices. Postprocessing, such as metal coating or plating, created circuit structures when both conductive and dielectric materials were required. In the 2010s, conductive and dielectric multimaterial printing techniques emerged along with a few successful commercialized printing systems taking advantage of the matured printing techniques, such as FDM, aerosol jet printing (AJP), piezoelectric inkjet (PI), and thermal inkjet printing (TIP). One notable advancement during this time was the introduction of technologies that allowed for the deposition of multiple materials in a single print job. The world's first 3-D printer for electronics appeared at the Consumer Electronics Show in 2015 [12]. The demonstrated Voxel8 3-D Electronic Printer uses fused filament fabrication (FFF) techniques for multimaterial 3-D-printed electronics. The filament materials include stainless steel, polylactic acid (PLA), acrylonitrile butadiene styrene (ABS), and other polymer materials. However, this printing system has not been available since its acquisition by Kornit Digital in 2021.

Since 2015, four commercially available multimaterial AME printing systems that can prototype printed circuit boards (PCBs) using a single machine have appeared: DragonFly, BotFactory, nScrypt, and Optomec AJX5. The 3-D-printed electronics have gained significant attention in recent years, and their standardization, known as IPC D-67 AME, is currently under development by the Institute of Printed Circuits (IPC) [13].

B. AM Versus Traditional Manufacturing

AM is also called 3-D printing. The former is widely used by industry, encompassing a broad range of manufacturing processes in an additive way. At the same time, 3-D printing emphasizes the capability of creating objects in 3-D by adding materials layer by layer. The latter is more used for application-driven circumstances, especially in consumer-oriented scenarios.

The difference between the additive and traditional manufacturing can be found in the following aspects.

1) *Prototyping mindset:* Distinguished from traditional manufacturing approaches, AM demonstrates a disruptive mindset in prototyping. It emphasizes the capability of additively fed materials to build prototypes and facilitate fabrications instead of the conventional way of removing materials from the given objects to create the desired structures. This mindset unlocks the freedom for engineers to design electronic devices in truly 3-D layouts, which is ideal for device miniaturization and circuit customization.

2) *Prototyping complex designs:* Additively building physical structures (e.g., layer by layer) provides the opportunities to achieve geometrically complex structures in a single process that could be challenging
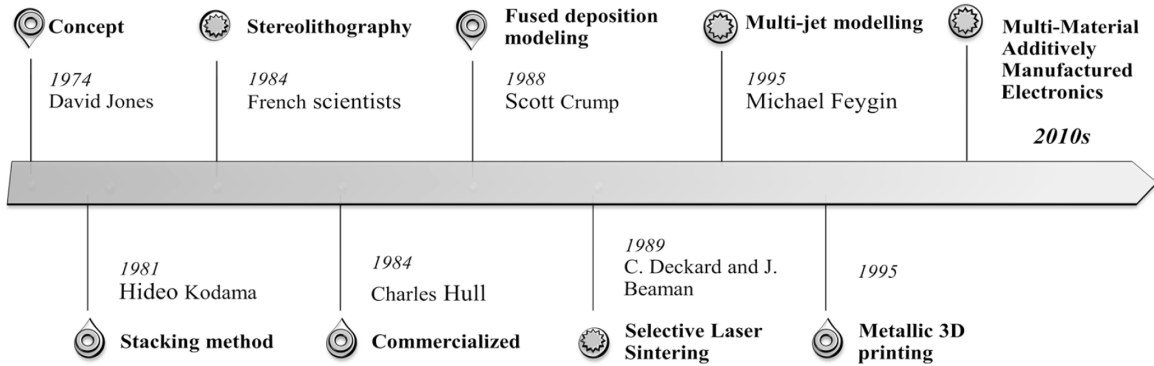
Fig. 1. *History of 3-D printing.*

or impossible to fabricate in subtractive approaches, which often requires multiple methods (e.g., milling, drilling, and assembling). Assembling high-precision electronic devices results in extra fabrication costs and misalignment issues, especially for devices requiring microscale fabrication tolerance. However, a single multimaterial AM machine can avoid complicated electronic device fabrication procedures.

In addition to the features mentioned above, AM has the merits of print-on-demand (zero material waste) and design customization for low-volume production, such as customized sensors for wearable electronics. AM is defined as a revolutionary technology in Industry 4.0. It has also been identified as a critical approach for the in-space manufacturing of electronics and avionics [14].

C. Emerging 3-D-Printed Electronics

AME is an emerging technology that leverages 3-D printing techniques to create electronic components using single material or multiple materials. Single-material 3-D-printed electronic devices include waveguide components [15], [16], [17], [18], [19], [20], [21], [22], [23], [24], [25], [26], [27], [28], [29], [30], filters [31], [32], [33], [34], [35], [36], [37], [38], [39], [40], antennas and arrays [41], [42], [43], [44], [45], [46], [47], [48], [49], [50], [51], [52], [53], [54], [55], [56], [57], [58], [59], [60], [61], [62], [63], metamaterials [64], [65], [66], [67], [68], [69], lenses [70], [71], [72], [73], [74], [75], [76], [77], [78], [79], [80], [81], [82], [83], [84], [85], frequency selective surfaces (FSSs) [86], and sensors [87]. Conductive and dielectric multimaterial printing has only appeared in recent years. The demonstrated circuit components include signal transmission lines (TLs) [88], [89], [90], inductors [91], [92], [93], filters [94], [95], [96], [97], [98], [99], antennas [100], [101], [102], electromagnetic (EM) lenses [103], [104], metasurfaces (MSs) [105], [106], [107], [108], [109], and transistors [110]. As shown in Fig. 2, AME has been proven to be a groundbreaking technology for designing complex electronic components with exceptional performance.

1) *Multimaterial AME:* Printing conductive and dielectric materials within the same processing system is the future of 3-D-printed electronics. AME overthrows how electronic circuits are manufactured and unlocks the flexibility of designing multifunctional electronic devices, which are impossible to manufacture using traditional techniques such as PCB. An ideal multimaterial AME printer has two printing heads in a single machine that can simultaneously print conductive and dielectric materials. Commercially proven systems, such as FDM, lights-out digital manufacturing (LDM), and multimaterial inkjet printing techniques, can build 3-D circuits directly embedded into the device package without postprocessing. Multimaterial AME enables electronic engineers to utilize circuit packages/spaces more efficiently than their counterparts using flat PCBs, which is ideal for miniaturization.

2) *Shape-memory AME:* As an emerging direction in electronic devices, SMMs have been explored in recent years for their applications in flexible electronics [111], [112], [113], [114], [115], electricity generation [116], super-capacitors [117], [118], digital healthcare [119], wearable sensors [120], [121], energy harvesters [122], and metamaterials [123]. SMMs are a kind of material that can remember a particular shape. When external stimuli are applied, the SMMs can return to their original shapes from the deformed states. The SMMs' shape-memory effect (SME) has been found interesting to scientists across the disciplines of electronic engineering, chemical engineering, material engineering, and mechanical engineering. The functions unlocked by the SME are crucial for intelligent electronics that can impart structural responsiveness and, ultimately, autonomous deployment in places that are difficult to access, such as the human body and space [124], [125].

The SMEs are primarily observed in certain alloys and polymers, called shape-memory alloys (SMAs) and
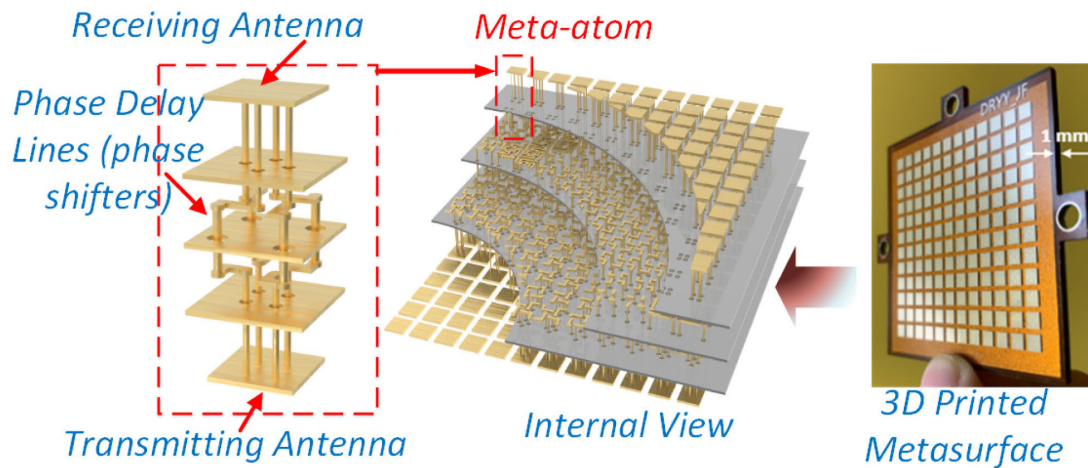
Fig. 2. *Additively manufactured metasurfaces with seven metal layers in a single substrate. Invisible vias are 3-D-printed for interconnecting phase delay lines among the transmitting and receiving antennas at the top and bottom surfaces [108].*

shape-memory polymers (SMPs). The most known SMA is nickel-titanium (NiTi), which requires metallic processing techniques for fabrication. The SMPs are polymers that are easy to fabricate using general low-temperature heating processes.

Until today, SMMs have not been widely used in electronics (e.g., flexible electronics, wearable sensors, radio frequency (RF) circuits, and antennas) due to the inadequate nature of the available processing techniques. However, these challenges have been gradually tackled by scientists and engineers taking advantage of today's maturing material processing techniques and prototyping tools. AM is gaining interest in fabricating SMM electronic devices using the AM processes, such as FDM, SLA, digital light processing (DLP), and laser powder bed fusion (LPBF) AM, which will be the dominant approaches prototyping SMM electronic components.

D. Research Opportunities and Challenges

As a new technology, AME faces several challenges to be continuously addressed, representing the future research directions across the disciplines of chemical and material engineering, electrical and electronic engineering, and mechanical and mechatronics engineering. The following are the key areas for researchers and engineers to consider.

1) *Conductive materials printing:* Printing high-conductivity metallic materials is challenging. The printable conductive materials suitable for electronic components are limited. The commonly used conductors in electronics are copper, silver, gold, and aluminum. Coppers and silvers are found to be more practical considering the required precision printed electronics and AME printing system yet there are challenges related to materials chemistry, for example, printing coppers, which suffer from rapid oxidation under air. However, developing conductive inks (CIs) compatible with precision AM processes is crucial for designing functional electronic components.

2) *Multimaterial integrated printing:* Conductive and dielectric multimaterial printing in a single print job is challenging. To keep the electrical properties of the developed AME circuits, the conductive and dielectric inks (DIs) have to be seamlessly printed to maintain the devices' structural integrity, which cannot be easily achieved.

3) *Material interface adhesion:* Multimaterial interfacing is critical for maintaining electronic devices' performance in terms of both electrical performance and mechanical strength. The challenges of building a reliable interface between conductive and dielectric materials are still outstanding for AME devices. The poor layer adhesion may cause signal transmission failure or inconsistent circuit connectivity.

4) *Printing resolution and precision:* For precision electronics, printing resolution determines the form factor of the AME system. High-resolution printers may be applied for prototyping high-frequency AME devices operating in the millimeter-wave (mm-wave)/subterahertz bands (30–300 GHz). Printing fine features, such as narrow and thin conductive traces, requires precision printing process control, which is challenging but highly expected by RF engineers.

5) *Software design tools:* Designing complex 3-D AME components relies on powerful software that can handle mechanical and electronic design aspects. Such a multipurpose simulation tool does not exist at the moment. Still, it should be developed to unlock the full potential of AME for advancing electronics research, such as flexible electronics, medical devices, intelligent sensors, and space electronics.

E. Organization of This Article

The multimaterial AME and 4-D printing SMM are comprehensively reviewed in the following way. Section II introduces the motivation of multimaterial AME, followed by the state-of-the-art multimaterial AME facilities. Section III presents the design and implementation of multimaterial AME devices, including design examples. Section IV introduces the concept of 4-D printing technology. Its applications to shape-memory electronic designs are given in Section V. Section VI discusses the design, applications, and calibration of 4-D electronic designs based on origami-inspired arrays. Section VII includes a summary and insights into future perspectives on multimaterial 4-D printing technologies.

II. MULTIMATERIAL AME

A. AME—Motivation

AME devices can be categorized into two categories based on the materials: single-material and multimaterial printed components. Most of these single-material 3-D-printed electronic devices were used to manipulate EM waves, such as waveguides [15], [16], [17], [18], [19], [20], [21], [22], [23], [24], [25], [26], [27], [28], [29], [30], filters [31], [32], [33], [34], [35], [36], [37], [38], [39], [40], antennas and antenna array [41], [42], [43], [44], [45], [46], [47], [48], [49], [50], [51], [52], [53], [54], [55], [56], [57], [58], [59], [60], [61], [62], [63], or slab-shaped periodic structures for beam shaping, such as EM lenses [64], [65], [66], [67], [68], [69], [70], [71], [72], [73], [74], [75], [76], [77], [78], [79], [80], [81], [82], [83], [84], [85], Luneburg lens [70], FSSs [86], and reflectarrays.

To enable signal transmission in circuit-based devices such as mobile electronic devices, computer, or satellites, multimaterial 3-D printing is expected to prototype signal traces, metallic vias, interconnectors, inductors (coils), capacitors, and other passive circuit components, such as filters, crossovers, phase delay lines/phase shifters, and antennas. Thus, conductive and dielectric multimaterial 3-D printers came to the commercial market and revolutionized the AME industry. Compared to single-material 3-D printers, multimaterial 3-D printers have two print heads that can simultaneously print conductive and dielectric materials. Unlike the traditional PCB process, multimaterial AME can produce multiple metal layers and complicated signal traces in the circuit substrate with flexible interlayer spacing.

Over the past decades, researchers have applied AME techniques to the design and fabrication of a wide range of electronic devices, such as TLs [88], [89], [90], lumped elements [91], [92], [93], couplers, sensors [28], filters [94], [95], [96], [97], [98], [99], antennas [100], [101], [102], metasurfaces [105], [106], [107], [108], [109], and packaging of integrated circuits, which proved the concept of multimaterial AME designing high-performance electronic components.

Recent advancements in device fabrication also enabled additive and other integrated processing techniques (e.g., coating/plating) to achieve structurally complex and functional electronic devices. For example, metal plating is performed on the AM dielectric models in [70], [126], and [127]; metal tapes are attached to the AM dielectric substrate to form circuits [55], [56]; metal parts and media parts are printed separately in [128] and [129]. They are then assembled into a complete electronic device. The combination of these processing methods enriches the diversity of multimaterial AME. There is an urgent need to improve electronic components' design flexibility and processing capability as soon as they continue to innovate.

B. State-of-the-Art AME Facilities

There are many AME systems available on the market. To choose the most suitable process, it is important to understand these commercially available 3-D printing facilities and their capabilities. There are four main 3-D printing techniques suitable for conductive and dielectric multimaterial 3-D printed electronics [130], [131]: FDM, AJP, PI, and TIP.

1) *FDM:* FDM system uses one or multiple nozzles to extrude filaments or paste-like materials onto a platform (e.g., printing bed) or the previously printed layers. Compared to other technologies, the significant merits are its accessibility, relatively low cost, and compatibility with a wide range of materials, such as ABS, PLA, polyethylene terephthalate glycol (PETG), and SMPs. These thermoplastics offer different properties, such as strength, flexibility, shape memory, and heat resistance, allowing for a versatile selection based on specific application needs. However, FDM also has some limitations and demerits. The layer-by-layer nature of the printing process can result in visible layer lines on the printed objects, requiring additional postprocessing or finishing techniques for a smoother surface finish. Material extrusion's printing speed is generally slower than other 3-D printing technologies, making it less suitable for large-scale or time-sensitive manufacturing projects. Complex geometries may require support structures, which can add complexity and increase material usage and postprocessing efforts. Material extrusion is widely utilized, which offers versatility in material selection and accessibility. Its relatively low cost and ability to produce functional parts make it popular among various industries and applications. However, it is crucial to consider its limitations regarding surface finish, printing speed, and support structures when choosing material extrusion for specific projects.

2) *Multimaterial inkjet printing:* AJP, PI, and TIP belong to the multimaterial inkjet printing family. The mechanism of multimaterial inkjet printing involves the deposition of droplets of liquid material from multiple print heads onto the build platform. The print heads

Table 1 State-of-the-Art Multimaterial AME Processing Systems for PCB Prototyping

Technology	Machine	Material	Max Size (mm³)	Number of Layers	Line/Space	Layer Thickness	Dk	Df	Ref
Fused deposition molding	Voxel8 3D Electronics Printer*	Metal and polymers	100 × 150 × 100	N.A.	475 μm	NA	2.75@ 2 GHz	0.015@ 2 GHz	[99]
Fused deposition molding + stereolithography	nScrypt 3Dn-600	Conductive paste and acrylonitrile butadiene styrene	600 × 600 × 150	Single-sided	1 μm /10 μm	0.65 μm	3 @ 2 GHz	0.03 @ 2 GHz	[90]
Piezoelectric inkjet	DragonFly IV	Optimized silver nano particles and dielectric inks	160 × 160 × 3	17-layer PCB	75 μm / 100 μm	1.18 μm	2.77 / 2.78@ 2 GHz/ 15 GHz	0.015 / 0.018 @2 GHz /15 GHz	[97]
Thermal inkjet printing	Botfactory SV2	Conductive inks and insulating inks	117 × 140 ×15.24	4-layer PCB	200 μm / 400 μm	10 μm	3.7@10 kHz	0.025@10 kHz	[141]
Aerosol jet printing	Optomec AJX5	Silver ink and polyimide	NA	Multilayer	200μm/ NA	NA	NA	NA	[140]

*Discontinued

contain tiny nozzles that highly precisely eject the droplets based on the design data. Once the droplets are deposited, they are solidified by evaporation or cured using ultraviolet (UV) light for photopolymerizable inks, forming each object layer. This process is repeated layer by layer until the complete 3-D object is created. There are several merits to multimaterial inkjet printing technology. It enables the production of highly detailed and complex geometries, making it suitable for product design, prototyping, and architectural modeling applications. The ability to utilize multiple materials in a single print creates realistic models with different colors and material properties. Multimaterial inkjet printing also offers high accuracy and repeatability, ensuring consistent results for each print. However, there are also some demerits associated with multimaterial inkjet printing. The cost of inkjet printers and materials can be relatively high, making them less accessible for some users. The printing speed may be slower than other technologies, mainly when using high-resolution settings or multiple materials. Support structures are not always required but may be needed for overhangs or complex geometries, adding to postprocessing efforts and material waste. In brief, inkjet printing technology, or material jetting, utilizes the precise deposition of liquid photopolymer materials to create 3-D objects. Its ability to produce high-resolution, detailed models with a smooth surface finish using multiple materials. However, the cost, printing speed, and postprocessing requirements are factors to consider when utilizing inkjet printing for specific applications.

Table 1 shows the state-of-the-art multimaterial 3-D printing technologies.

1) *Voxel8's 3-D electronics printer:* As an FDM technique, this printing system has multimaterial printing capabilities with a build volume of $100 \times 150 \times 100$ mm [132]. The printable materials include stainless steel, PLA, ABS, and polyesters. Voxel8 was acquired by Kornit Digital in 2021. This printing technique is no longer accessible.

2) *nScrypt 3Dn-600:* As a hybrid printing system combining FDM and SLA, nScrypt 3Dn-600 is one of the most advanced and versatile printers that prints various materials with high resolution and speed. This printer is a factory-in-a-tool (FiT) 3-D manufacturing system that can print multiple materials with high precision and speed using various materials, including metals, ceramics, polymers, composites, and biological materials. This machine also integrates other functions such as sintering, curing, laser, vision, and scanning. Aerospace, medical, and industrial sectors are some application areas of this machine, which have the apparent advantage of printing high-accuracy PCBs (single-sided) with fine-feature collector lines between 1 and 10 μm in width using silver-infused inks.

3) *DragonFly IV:* Another multimaterial AME printer, DragonFly IV, implemented by PI, is the most convenient and compact machine with the capacity to print conductive and dielectric materials simultaneously. DragonFly IV prints multilayer (~17 layers) PCB prototypes with a minimum trace width of 75 μm and a minimum trace spacing of 100 μm and embeds components such as resistors, capacitors, light-emitting

diodes (LEDs), and sensors into the multilayer structures. The defense and space industries have shown strong interest in its capability to produce complicated electronics in-house with exceptional performance, which is quickly becoming enthralled by extraordinary machines.

4) *Botfactory SV2:* Using TIP technology, Botfactory SV2, is the most affordable and accessible machine that can print conductive and insulating materials sequentially, with a maximum of four PCB layers. Although this printer's print resolution differs slightly from other contemporary printers, its cost is less than that of other devices, which makes it popular in education, research, and hobby projects due to its friendly price.

5) *Optomec AJX5:* The facility is a high-speed, high-resolution 3-D printer capable of printing inks composed of copper, silver, gold, aluminum, and nickel particles. It can print on various substrates, including glass, plastics, ceramics, and metals. It can also print nonplanar and conformal geometries, including curved surfaces, edges, and holes. AJX5 can be used for prototyping antennas, sensors, interconnects, and electromagnetic interference (EMI) shielding. It employs AJP, atomising the material into a thin mist before depositing it via the nozzles.

The AME printers mentioned above have several advantages over traditional PCB preparation processes, which use a single material and require multiple steps and processes to create PCBs [133], [134]. Multimaterial 3-D printing allows for the creating of complex and customized shapes and structures for various devices and applications. It can also print conductive, insulating, magnetic, optical, thermal, and biological materials. This permits numerous functions and attributes to be integrated into a single device. Furthermore, multimaterial 3-D printing can potentially avoid material waste, labor costs, and production time compared to traditional PCB technology. It can also enhance the performance and reliability of PCBs by minimizing the parasitic effects, interconnections, and solder joints prevalent in conventional PCB technology.

Additionally, multimaterial 3-D printing can facilitate the fabrication of novel devices with superior functionality and efficiency. However, the challenges faced by multimaterial AME are caused by different factors. The vulnerable ink nozzles, which jet different ink under diversified atmospheric pressure or temperature, expend the budget due to the special maintenance requirements. In addition, uncontrollable tension and deformation variables between the printed structure and printing platform during operation are another common problem that causes corners to warp. In the case of RF circuit design, the electrical performance suffers from a lack of extensive and specialized research on the materials, such as the dielectric constant and tangential loss at different frequency ranges.

III. MULTIMATERIAL AME DESIGN AND IMPLEMENTATION

Multimaterial AME designs can be achieved in many ways, subject to the implemented printing systems. The 3-D models of the AME designs are usually developed using computer-aided design (CAD) software, such as SolidWorks, Ansys Electronics Desktop [High-Frequency Structure Simulator (HFSS)], and Computer Simulation Technologies (CST). A file format compatible with the printing system should be exported from the circuit design software. When the 3-D model is successfully loaded into the software hosting the 3-D printer, e.g., Fusion 360, the designers can apply a slicer for optimizing the movement path and printing parameters and obtain the data file by slicing the 3-D object to be prototyped [135], [136]. The data file (e.g., .step or .stl) based on different materials will be imported to a 3-D printer to read and realize the layer-by-layer accumulation of raw materials to build the electronic devices.

A. Multimaterial Prototyping Design Flow

The design flow for AME involves several steps, from conceptualizing the design to implementing the electronic components. Here is a general overview of the process, as shown in Fig. 3.

1) *Conceptualization:* Identify the application and functionality requirements for your 3-D-printed electronic device. Define the form factor, size, and shape of the final product. Consider the materials and printing technologies suitable for the applications.

2) *Schematic design:* Create a schematic of the electronic circuit using a design tool such as CST, HFSS, SolidWorks, and Altium. Define the components, connections, and overall architecture of the circuit.

3) *PCB layout:* Transfer the schematic to a PCB layout tool to design the physical layout of the circuit. Consider the 3-D aspect by placing components in the 3-D space, considering the constraints of the 3-D printing process.

4) *Export 3-D model:* Export the 3-D model of the PCB layout from the software design tool. This model should include electronic components, traces, vias, drills, and crossovers.

5) *Material selection:* Integrate the 3-D circuit model with the mechanical setups of the electronic device. Ensure that the components fit well into the overall structure. Choose suitable materials for 3-D printing that meet the requirements of the design's mechanical and electrical considerations. Some materials may have conductive properties that are ideal for printing electronic traces.

6) *Print preparation:* Prepare the 3-D printer by loading the selected materials. Adjust printer settings, layer height, and other parameters based on the requirements of the electronics and mechanical components.
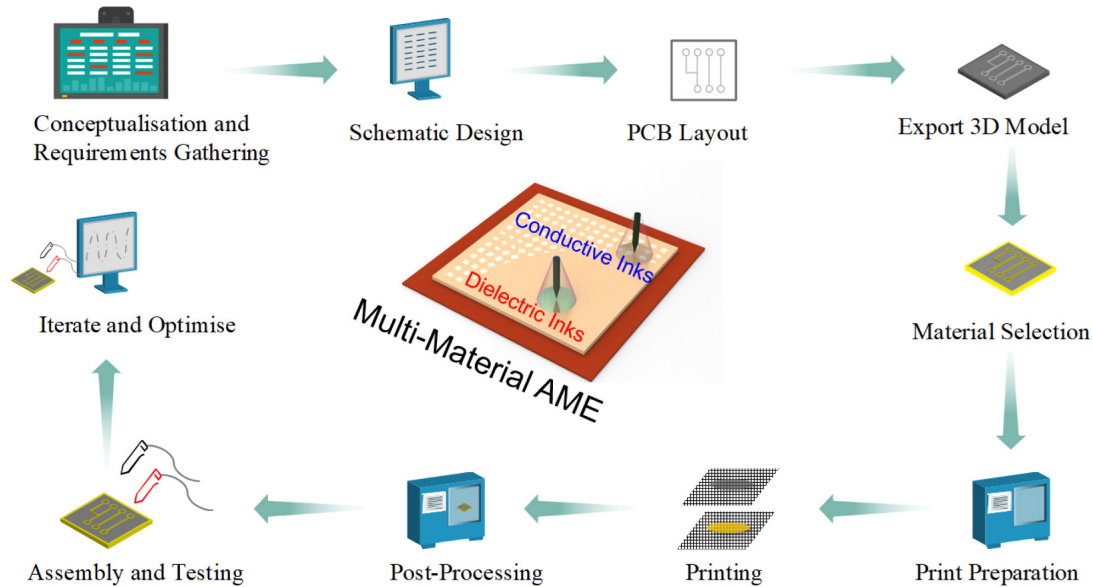
Fig. 3. *Multimaterial AME design flowchart.*

7) *Printing:* Start the 3-D printing process, layer by layer, to create the physical structure of the device. Ensure that the electronic components are embedded or placed accurately during printing.

8) *Postprocessing (if required):* Perform postprocessing steps such as cleaning, curing, or other treatments based on the selected 3-D printing technology and materials.

9) *Assembly and testing:* Assemble additional nonprinted components (if any), such as batteries, sensors, or connectors. Test the functionality and performance of the 3-D-printed electronic devices.

10) *Iterate andoptimize:* Evaluate the device's performance. Iterate through the design and printing process to optimize the final product until the requirement is met.

B. State-of-the-Art AME Designs

Although multimaterial AME is challenging, the realization of complex AME components has made breakthroughs and developments in recent years. Design examples are presented in the following based on the multimaterial AME technologies.

1) FDM: Using a Voxel8 3-D printing platform, coprinting CIs and thermoplastics created two prototypes of connected 3-D split ring resonator (SRR) sample filters [99]. An onboard pneumatic system regulates the flow of V8 Fuxi silver ink deposited through one of the nozzles. The second nozzle handles this CI prints at the required printing temperature and cures the conventional polymer filaments. The 0.25-mm nozzle size limits the printing resolution, and no extra techniques are employed in the manufacturing process to surpass this restriction. However,

the lowest horizontal air gap between conductor traces that this 3-D printer can produce with reliability must be more than 0.475 mm.

The prototype was constructed based on the design of a fourth-order bandpass filter (BPF) with a center frequency of 2.45 GHz. This was achieved using a compact SRR with a height of 2 mm, as depicted in Fig. 4(a). Fig. 4(b) presents the simulated and measured filter responses. The measured S-parameter exhibits passband width and roll-off characteristics that closely align with the numerical model. It validates that the raised SRR (3-D SRR) can significantly enhance the filter bandwidth compared with the SRR filter using conventional PCB. The mismatch between the simulation and measurement results indicates that the printer's resolution may substantially affect the performance of the high-frequency RF electronics.

Moreover, a creative thermally programmable conformal metasurface was presented by a brand-new thermal programming method based on FDM technology [137]. Fig. 5(a) depicts the planned curved metasurface carpet cloak with readily bending unit cells. The metasurface structure comprises the copper foil, PLA dielectric substrate, and tin-bismuth metal ring. The intermediate plane element surface structure was manufactured by alternating PLA and tin-bismuth dual nozzles. However, the interface properties between PLA and bismuth selenium materials in this structure are relatively weak. To address this, the flat samples undergo postprocessing with a PLA solvent, which chemically dissolves the surface layer of the PLA. Once the solvent evaporates, the PLA surface adheres more securely to the edges of the bismuth-selenium ring. Next, a spray adhesive is applied between the original surface and the curved surface mold. This ensures that stress is

(a)

(b)
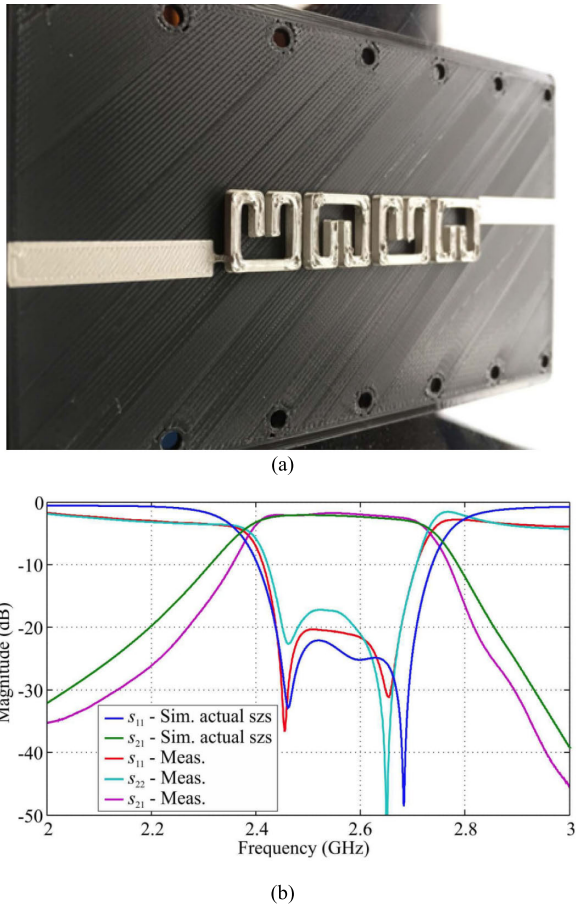
Fig. 4. *(a) 3-D-printed SRR BPF. (b) Measured and simulated reflection and transmission coefficients [99].*

evenly distributed across the PLA base material during the rubber state deformation process. Positioning correction is achieved through the positioning of holes on the edge. Following conformal programming, ethanol separates the metasurface from the mold. Subsequently, copper foil is affixed to the bottom of the element surface to serve as a complete reflective layer. The auxiliary positioning edges are then cut to yield a curved element surface carpet cloak sample.

The results shown in Fig. 5(b) above suggest that under E_x and E_y polarizations, the thermally programmed 3-D-printed element surface performs exceptionally well in stealth throughout a comparatively large bandwidth. This work offers a workable implementation technique for intricate curved element surfaces, which will significantly advance the field of conformal invisibility cloak use of multimaterial printing technology.

Moreover, the multi-3-D manufacturing system at the University of Texas used a similar embedded wire mesh structure to design a microwave patch antenna [138]. In the prototype shown in Fig. 6(a), wire and mesh are inserted into the 3-D-printed thermoplastic using thermal embedding and ultrasonic waves. RF applications

that are high-performing and efficient in volume can be made possible by the technology, which involves dipping the mesh into a conformal, geometrically complicated thermoplastic surface during the production process.

As the measurement and simulation results are shown in Fig. 6(b), the measured curve matches well with the simulated one, and the resonant frequency of the trough is nearly −14 dB at 7.5 GHz. The 3-dB beamwidth is 144°, and the maximum measurement realized gain is 5.5 dBi, as shown in Fig. 6(c).

2) FDM and SLA: In [90] and [139], the microstrip line, stripline, and vertical interconnect structures between multilayer TLs were prototyped by the nScrypt 3Dn-600 system. In the process, Dupont CB028 conductive paste directly sticks to various substrate materials, including resin ProtoTherm and thermoplastic ABS switched by different pumps. As shown in Fig. 7, several striplines and suspended microstrips are fabricated with varying combinations of conductive and substrate to calculate and compare the loss of various substrates. By calculating the corresponding parameters of each TL, the average dielectric constant and loss tangent of different printing materials were accurately achieved.

(a)

(b)
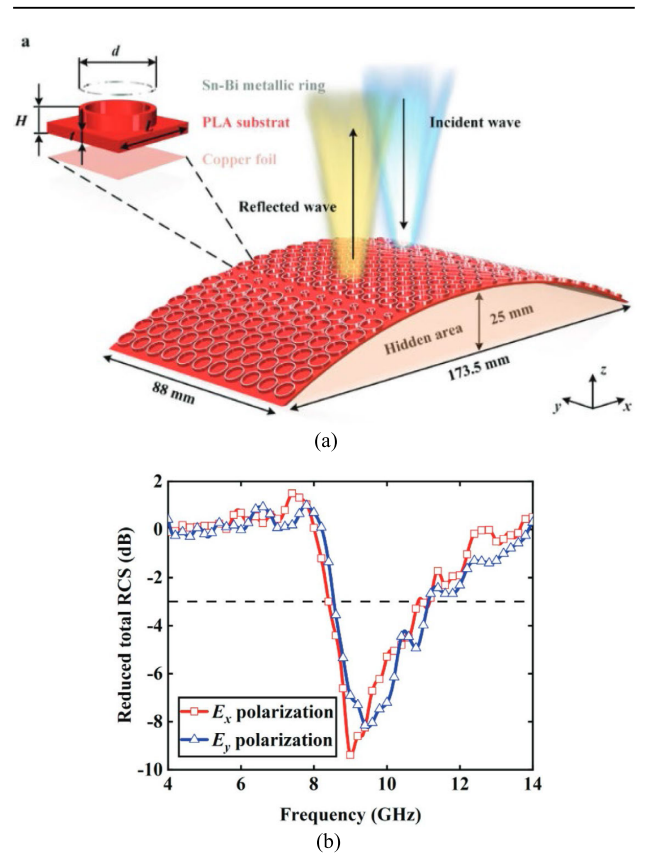
Fig. 5. *(a) Schematic of 3-D thermally programmable conformal printing metasurface and easy-bonding unit cells. (b) Polarizations at quasi-normal incidence [137].*

(a)

(b) (c)
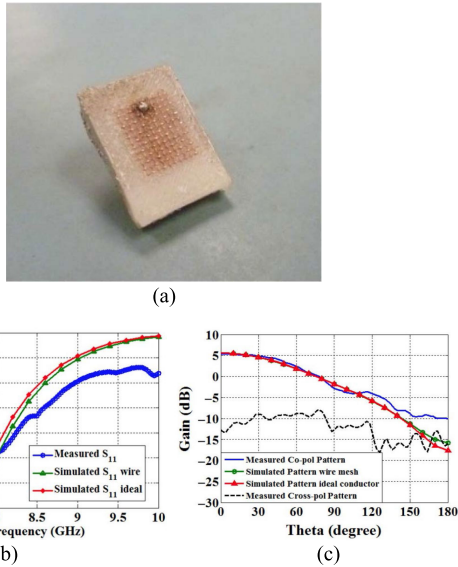
Fig. 6. *(a) Prototype of 3-D-printed patch antenna using embedded wire mesh structure. (b) Measured and simulated reflection coefficients of the proposed antenna. (c) Measured and simulated gains of the proposed antenna [138].*

3) AJP: Cai et al. [140] offer a unique 3-D structure with multilayer TLs, connecting devices, and embedded vias at high resolution up to 40 GHz using the Optomec AJP system. The structure is created using AJP to print dual materials (silver ink and polyimide). Fig. 8(a) shows the 3-D-printed TL with embedded vias for multilayer in-substrate interconnections using fabrication. Fig. 8(c) and (d) presents the TL performance in simulation and measurement. The insertion loss (IL) is around 1.2 dB at 1 GHz and 6.3 dB at 40 GHz for sample 1 (TL length = 11.4 mm). Sample 2 shows an IL of 0.9 dB at 1 GHz and 3.6 dB at 40 GHz, with a TL length of 6.4 mm.

4) TIP: Using the BotFactory SV2 thermal Inkjet PCB printer, another machine can simultaneously print conductive and DIs. In [141], laser-induced graphene sensors and their wiring and packaging were fabricated following the printing process shown in Fig. 9. To begin fabrication, each device's four sets of three alignment windows are printed onto a 125-μm-thick Kapton board. Once the 25.4-μm lenses have been loaded, aligned, and labeled Kapton, the laser ablates the traces left by laser carbonization. Furthermore, a laser was used to cut a thin rubber gasket with four external fastening holes and a central diaphragm hole (16 mm diameter). Lastly, a BotFactory SV2 printer was used to deposit the blanket insulation and silver wires. Comparable to previously attained sensitivities, the average linear sensitivity is roughly 5×10^{-5} kPa^{-1}, as shown in Fig. 10. This work reveals the possibility of producing flexible, susceptible strain gauge membranes by multimaterial 3-D printing.

5) PI: In recent years, functional AME devices (microwave filters [97], [98], couplers [98], metasurfaces

[105], [106], [107], [108], [109], [142], and antennas [102], [103]) have been significantly advanced by the DragonFly system, from microwave to terahertz frequency range [143].

6) Direct Ink Writing (DIW): DIW has become increasingly popular in electronic designs as a feasible approach to creating complex structures with customized geometries. This technique has been found to be capable of printing multiple materials, such as ceramics, polymers, and bioinks. Most recently, a direct ink-writing technique that relies on tension in the nozzle can be used to print freestanding metal structures with aspect ratios of up to 750:1 with the demonstration of AME devices without using supporting structure [144], [145].

a) Patch antenna arrays: The demonstrated AME solutions based on piezoelectric AM were used to build multiple metal layers antennas with conductive and DI at sub-6 GHz, as shown in [102]. According to the design guidelines, the minimum thickness of the conductive and dielectric layers is 2.5 and 0.3 μm, respectively. One driver patch and two stacked patches make up the three-layer patch antenna created by vertically stacking metal layers in a single substrate, as shown in Fig. 11(a). The large bandwidth and ultralow profile of the developed antenna prototype are its advantages. The antenna, whose overall thickness stays at 1.5 mm, achieves an operating bandwidth of 83% and a peak gain of 3.8 dBi, as shown in Fig. 11(b). The findings demonstrate that multimode stacked patches can boost bandwidth by utilizing a 3-D design while maintaining the same overall substrate shape, which is impossible using conventional PCB processes.

b) BPFs and couplers: In [97], a compact multilayer BPF at 12.25 GHz with a seamless structure on one substrate is realized using low-temperature (140 °C) multimaterial printing technology. The AME method utilized

(a) (b)

(c)
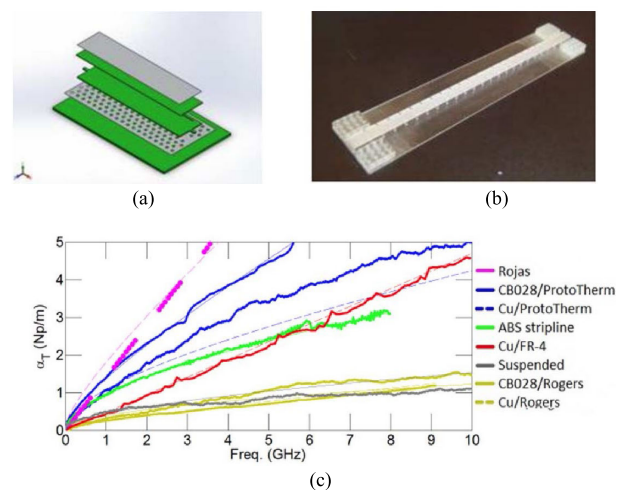
Fig. 7. *3-D-printed (a) stripline, (b) microstrip, and (c) loss comparison with different combinations of conductive and substrate [27], [29].*
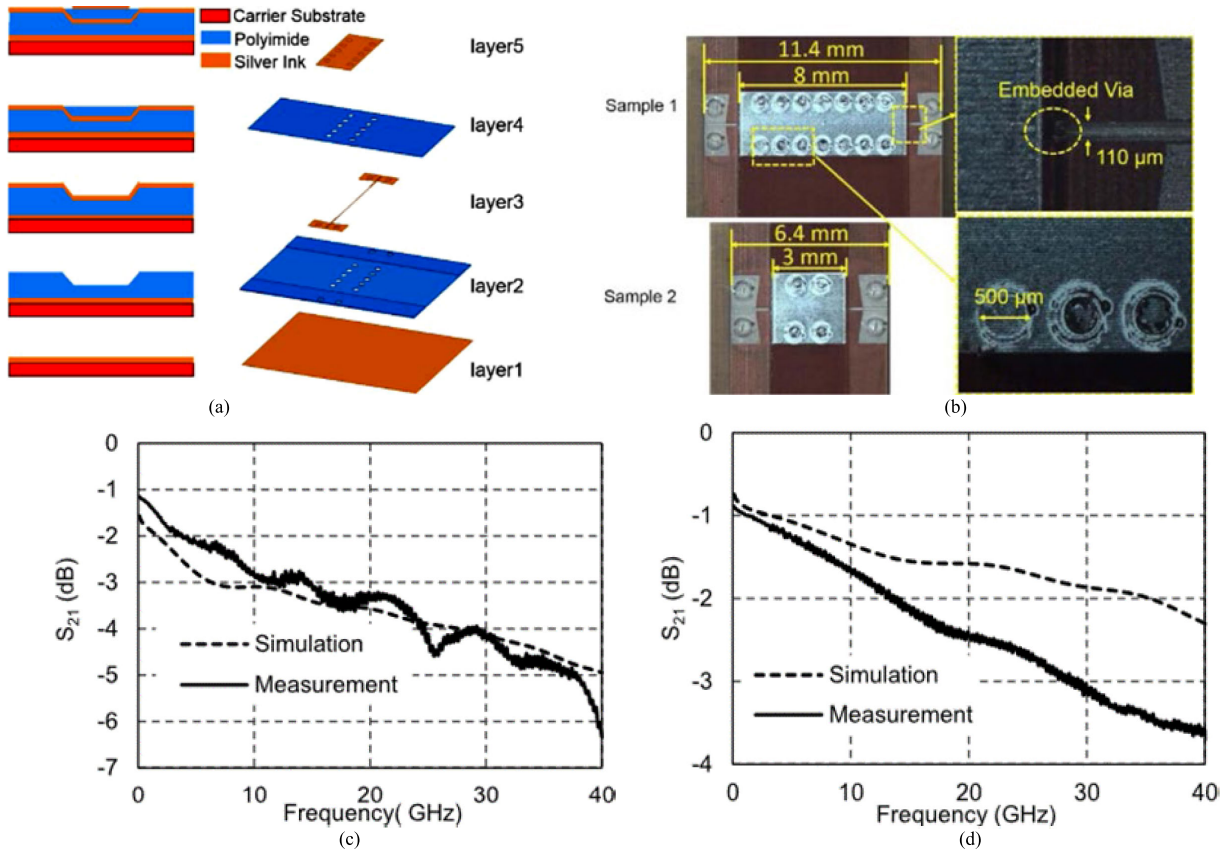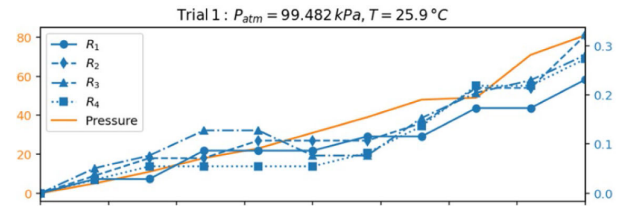
Fig. 8. *Process of (a) 3-D-printed multilayer interconnect and (b) via details of two samples. The measured and simulated transmission coefficients of (c) sample 1 and (d) sample 2 [140].*
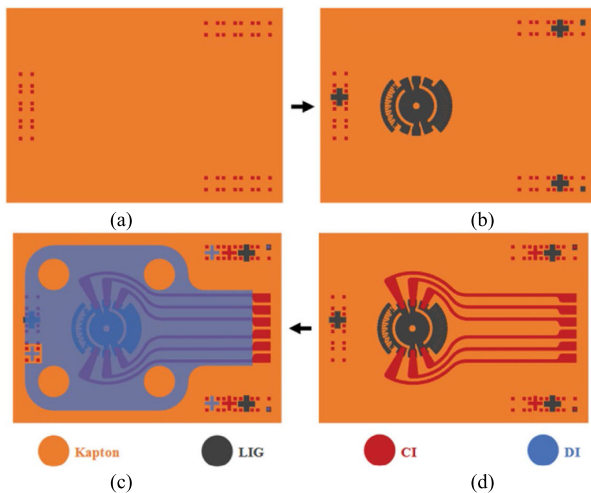

Fig. 9. *Process of printing pressure sensor by BotFactory SV2 printer. (a) Calibration by printing conductive marks. (b) Define the piezoresistors using the conductive marks. (c) Prints CI electrical patterns. (d) Prints DI patterns.*

Fig. 10. *Relationship between the percentage change in resistance of a resistor and the reduction in internal volume [141].*

Fig. 12. When the ink comes out of the nozzle during manufacturing, it is first cured using a UV lamp with a
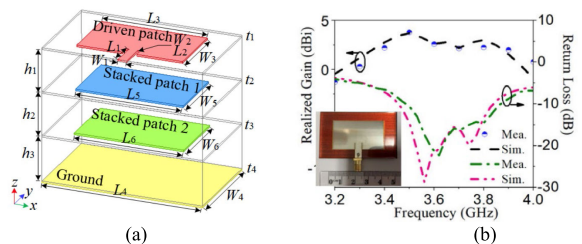
Fig. 11. *(a) Layout of the 3-D-printed multilayer patch antenna. (b) Measured and simulated return losses and gains of the proposed antenna [102].*
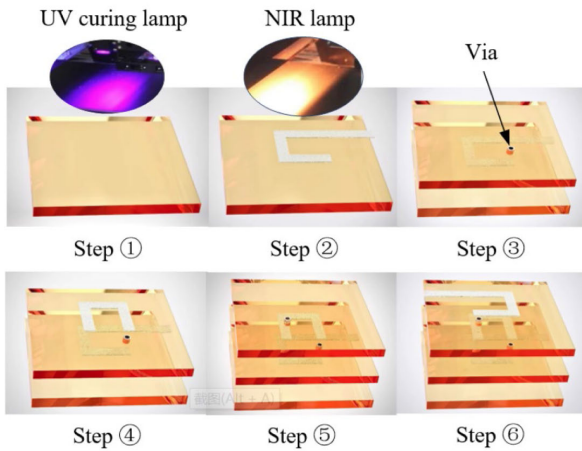
in the DragonFly LDM system allows for the simultaneous printing of acrylate inks and silver nanoparticles (SNPs). The fabrication process of a spiral inductor is shown in

Fig. 12. *Fabrication of 3-D spiral inductor [97].*

(a)

(b)

(c)

Fig. 14. *(a) Three-dimensional model. (b) Photograph of the multilayer VI-CRLH BPF. (c) Simulated and measured S-parameters of the VI-CRLH BPF [98].*

wavelength of 395 nm. After that, the acrylic layer is printed with metal strip lines. A near-infrared radiation lamp with a wavelength of 0.75–1.4 μm and a process temperature of 140 °C–170 °C is used to sinter the CI. Layers of acrylic and CI are printed repeatedly, creating a 3-D spiral inductor. Furthermore, vias can be produced concurrently in the acrylic layer to connect metal strip lines in various layers. There is no need to apply DI where vias are needed. Because the fabrication process occurs layer by layer, the silver is in the area that fills the via, and the dielectric is around the via. This solution is possible to incorporate miniaturized multilayer BPFs with a seamless structure on a substrate, as shown in Fig. 13. The developed BPF has a bandwidth from 9.58 to 14.57 GHz.
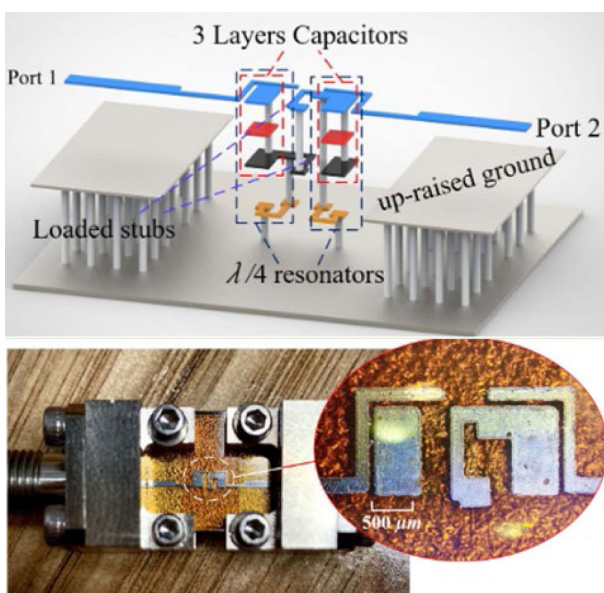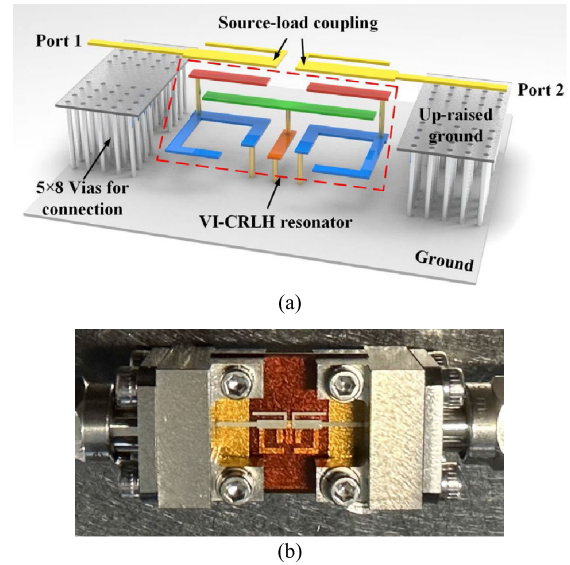
Fig. 14 shows a multilayer vertically integrated composite right/left-handed (VI-CRLH) TLs with compact size, broadband, and a balanced CRLH dispersion performance. The filter performance is shown in Fig. 14. A 3-dB bandwidth of the BPF is achieved from 4.28 to 9.03 GHz [71.4% of functional bandwidth (FBW)]. The CRLH-based coupler is shown in Fig. 15, with a ±1-dB magnitude imbalance between the through and coupled ports achieved from 4.2 to 7.4 GHz (55.2% of FBW) and excellent 90° phase balance from 4 to 8.6 GHz (73.0% of FBW) with ±3° phase imbalance between the through and coupled ports.

c) Vortex beam metasurfaces: Spin-decoupling wavefront shaping in a broadband mm-wave transmissive metasurface printed in 3-D was implemented using the DragonFly LDM and IV systems [106]. The suggested MS, which has nine layers, as shown in Fig. 16(a), is easier to build with 3-D multimaterial printing technology than conventional PCB fabrication, which can address several PCB fabrication issues. First, the bonding process required in PCB multilayer boards to guarantee strong connections between layers is not required in the Drag-


Fig. 13. *Three-dimensional view and photograph of the printed filter with connectors [97].*

(a)

(b)
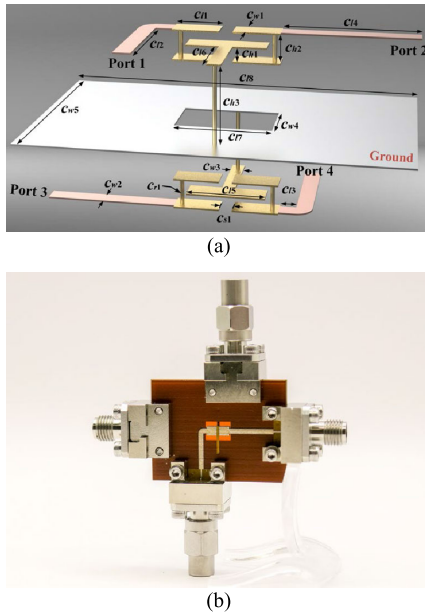
Fig. 15. *(a) Three-dimensional view and (b) photograph of the VI-CRLH coupler.*

onFly process. Second, the standard thickness of the PCB does not restrict the flexibility with which the spacing between neighboring metal layers can be chosen, thanks to the high-precision processing capacity on the height axis. Furthermore, several layers are constructed additively with solid material interface (between acrylates and silvers) connections without increasing the substrate profile as the number of layers increases. As shown in Fig. 16(b), the multilayer metasurface with the antenna–circuit–antenna complex structure exhibits the left-hand circular polarization radiation patterns from 27.85 to 31.54 GHz (*Ka*-band) with demonstrated vortex beam in different modes. Various multimaterial AME metasurfaces have been reported in recent years for mm-wave beam-shaping, polarization manipulations, and multibeam applications [105], [106], [107], [108], [109], [142].

d) Transmissive and reflective metasurfaces: AME transmissive and reflective metasurfaces with multiplexing channels for wireless communications have recently been verified through experiment [107], which demonstrates their potential beyond 5G and 6G innovative Internet of Things (IoT) applications. A five-metal-layer reflective metasurface that supports dual-band spin-decoupled quadruplex channels with independent beam shaping was presented in [102]. The samples of the reflective metasurface were prototyped using DragonFly LDM, which can be applied to the walls of buildings and convert the received incident wave from one direction to four other directions for multiple end receivers. In contrast to reflection-only metasurfaces, Zhu et al. [107] demonstrate an emerging concept of AME transmission–reflection-integrated metasurfaces for full-space quadruplex channels with independent phase modulation, which can be applied

to multichannel communication systems in future wireless networks. Fig. 17(a) shows the concept of the reflective AME metasurface and its 3-D model of the proposed meta-atom in Fig. 17(b). Fig. 17(c) shows the fabricated prototype with a left-hand circular polarized feed for device performance evaluation. Fig. 17(e) shows the application of the transmission-and-reflection AME metasurface in future wireless communications as a potential candidate for reconfigurable intelligent surfaces (RIS) deployment.

e) Lens antennas: A Fresnel zone plate (FZP) lens antenna consisting of transparent and opaque concentric rings arranged on a curve or plane was realized using AME [103]. The photograph of the fabricated multimaterial AME dual-band lens antenna is shown in Fig. 17(f). Combining two single-band FZP metal film antennas operating in separate frequency bands into a single aperture makes the suggested dual-band single-polarized FZP metal film antenna possible. One screen of the FZP lens can manipulate the *D*-band EM waves at 120 GHz, while the other controls the *E*-band EM waves at 75 GHz. The simulated and measured gains for the two frequency bands are depicted in Fig. 17(d) and (g). At 75 and 120 GHz, the measured

(a)

(b)
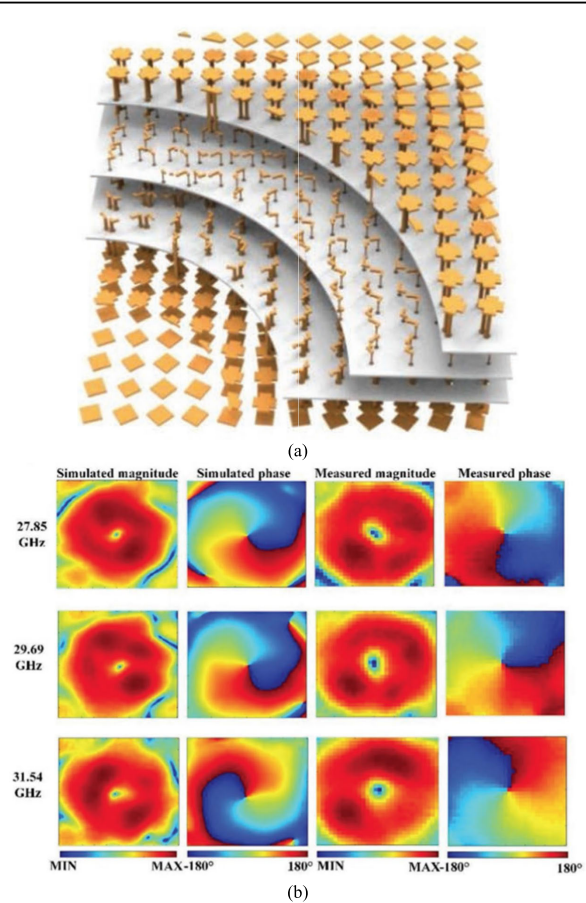
Fig. 16. *(a) Interview of the mm-wave 3-D-printed metasurface. (b) Measured and simulated intensities and phases of the proposed MS [106].*
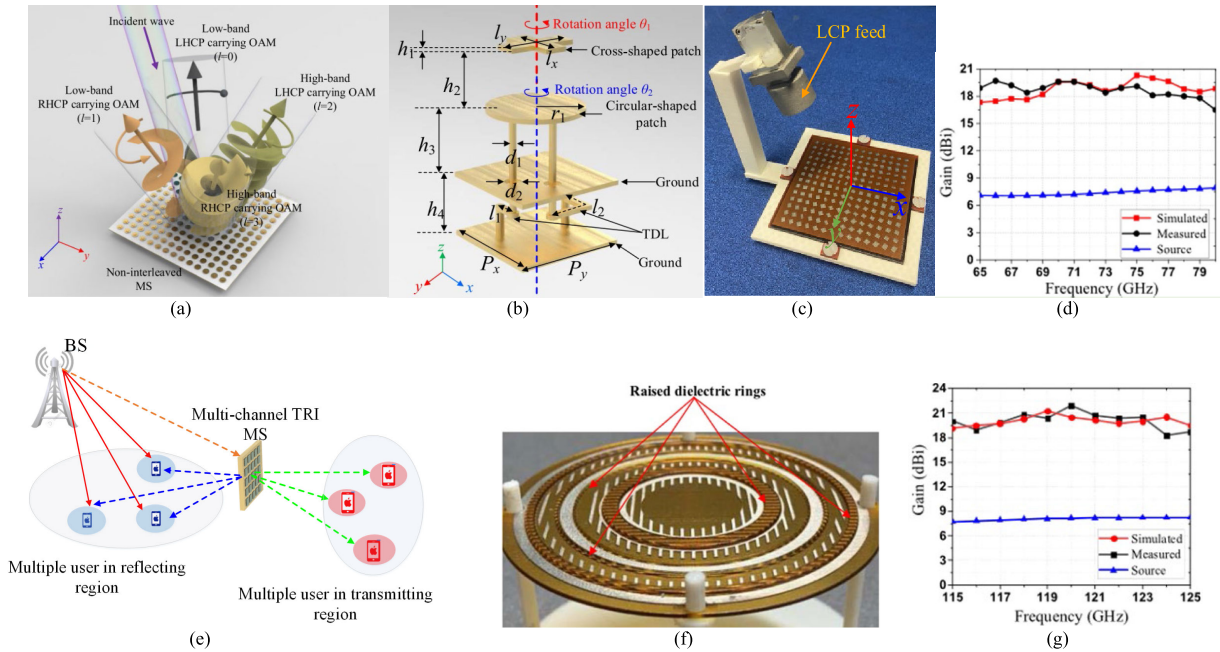
Fig. 17. *(a) Three-dimensional-printed dual-band spin-decoupled reflective metasurface for multimode orbital angular momentum (OAM) generation. (b) 3-D configuration and dimensions of the unit cell (not scaled), $h_1 = 0.035$, $h_2 = 0.43$, $h_3 = 0.535$, and $h_4 = 0.5$ unit (mm)* [107]. *(c) AME metasurface assembly with an incident signal as a feed source. (e) Application of transmission–reflection-integrated metasurfaces for multiple users in wireless communication environment* [142]. *(f) Photograph of the multimaterial AME FZP lens antenna. (d) and (g) Gain of the proposed dual-band FZP lens at 75 and 120 GHz* [103].

gains are 20.3 and 21.9 dBi, respectively. Compared to the waveguide source, the measured improvements were 12.7 and 12.9 dB, respectively, indicating that the FZP metal film antenna can collimate the beam in mm-wave and subterahertz bands.

During the past five years, the AME prototyping capabilities have been comprehensively investigated in [108], [146], [147], and [148], using the DragonFly systems, including version 2.0, Pro, LDM, and IV, for designing the multimaterial AME components. The fabrication tolerance in substrate thickness and material loss are still challenging for future high-frequency RF electronics designs.

C. Emerging Multimaterial 3-D-Printed Electronic Devices

The 3-D-printed electronic devices appeared more in flexible electronics for wearable applications, which are well-known to be the next frontier in the approaching future, supported by the multimaterial printing technology. The 3-D electronic components mentioned in the last part can be dissolved and embedded into multidimensional structures to form functional electronic devices, including sensor systems, controllable circuits, and soft electronic devices [149], [150], [151], [152]. On the other hand, multimaterial 3-D printing is also applied for batteries using super-capacitors. In [153], a microsuper-capacitor with an energy storage function was fabricated by add-free MXene inks and direct printing of high performance at

high resolution. As shown in Fig. 18, Ti3C2Tx organic ink is used for inkjet printing of various patterns. Simultaneously, mesenchymal stem cells and other designs are extrusion printed on flexible surfaces using a water-based ink called Ti3C2Tx. Furthermore, to create fully MXene-printed solid mesenchymal stem cells, a gel electrolyte of H2SO4-PVA was applied to the printed pattern and allowed to dry naturally. To reduce the number of flaws on the MXene nanosheets, the research employed a less forceful etching technique known as the "minimum dense layer delamination method." The multilayer obtained pie-shaped formation needed to be vigorously shaken in water or treated with water bath ultrasonic delamination in organic solvents because it would swell after several water washings. On the other hand, stable and concentrated flakes can be created by using appropriate organic solvents with high polarity and strong dispersion interaction strength. It is important to note that lower boiling point solvents, such as methanol, typically have lower polarity indices and, as a result, have poorer MXene nanosheet dispersion, which reduces the dispersion stability.

Furthermore, a monolithically integrated self-powered smart sensor system comprising printed gas sensors for ethanol and acetone detection [154], printable super-capacitors as an energy source, and embedded solar cells was successfully shown using inkjet printing as a proof-of-concept.
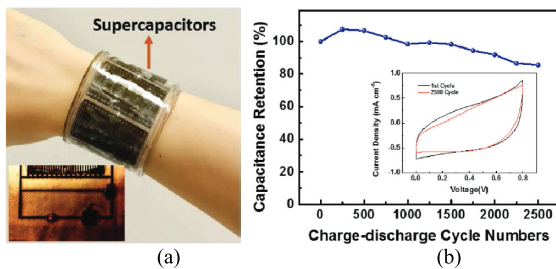
The solar energy collected in a wearable wristband, as depicted in Fig. 19(a), can either be used directly to power
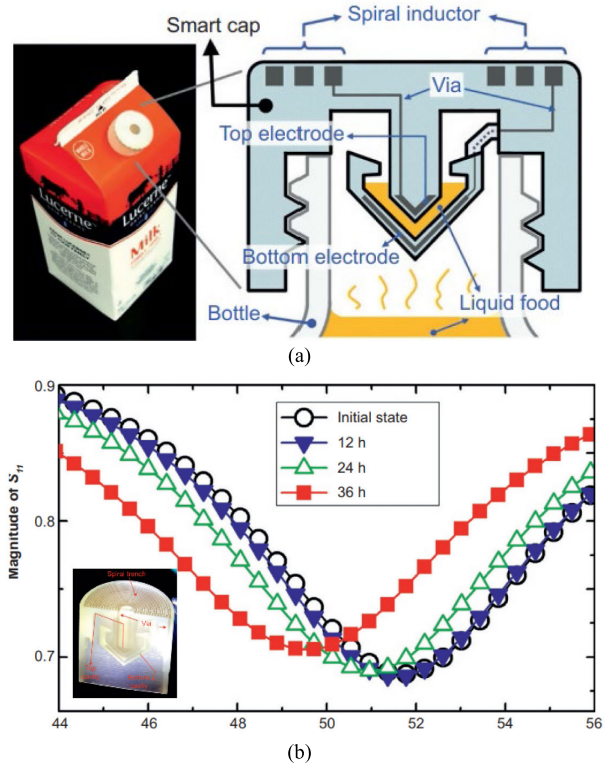
(a)

(b)
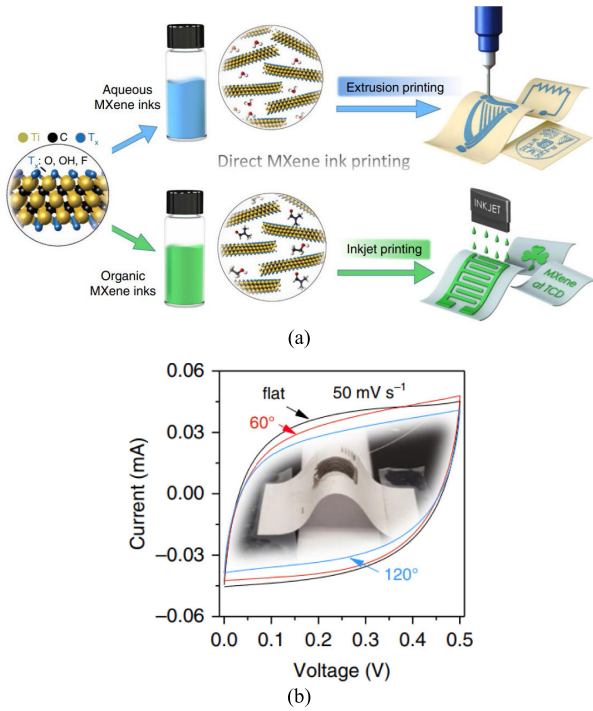
Fig. 18. *(a) Diagram of direct MXene ink printing. (b) Measured and simulated intensities and phases of the proposed MS [153].*

(a)

(b)

Fig. 20. *(a) Photograph and the diagram of wireless passive sensor system integrated into a multimaterial printed smart bottle cap. (b) Amplitude versus frequency curves of milk at 22 °C at different time intervals [155].*

the LED as a warning signal by driving the sensor, or it can be stored in a super-capacitor in standby mode to be used as a compensation for intermittent illumination. This value is relatively high compared to earlier studies on printed planar super-capacitors. Moreover, the stability of the produced device was confirmed by cycle life measurements in Fig. 19(b), which were carried out at a scan rate of 100 mV·s^{-1}. As measured after 2500 cycles, the capacitive state is still greater than 80%. The two designs mentioned above have a lot of potential for creating multimaterial printing techniques for system integration and device production.

In [155], a wireless passive sensor for wirelessly monitoring the quality of liquid foods like milk and juice is integrated into a multimaterial printed smart bottle cap. The suggested capacitor's sensing diagram, which includes

an integrated *LC* tank sensor, is depicted in Fig. 20(a). An *LC* resonant circuit is formed in this design by a planar spiral inductor and an inverted tapered capacitor. The tank is trapped in the low-concentration tank's capacitive gap when the meal package is turned upside down, serving as a dielectric substance. The liquid food's dielectric constant determines the resistance value of the liquid chromatography tank. The reaction varies as a liquid deteriorates because the dielectric constant shifts. The *LC* tank sensor generates electrical oscillations and stores energy through near-field inductive coupling by implementing a sweeping electric field in the reading coil. Because the *LC* tank absorbs most EM energy at this frequency, oscillations are most noticeable when the drive and resonant frequencies coincide. This peak can be recorded to follow the response frequency wirelessly and instantly determine the quality of the liquid food without opening the packaging. As shown in Fig. 20(b), the resonance frequency of milk kept at room temperature for 36 h had altered by 4.3%, according to the results. This work expands the use of multimaterial printed electronics in food safety by establishing a novel technique to build arbitrary 3-D systems.
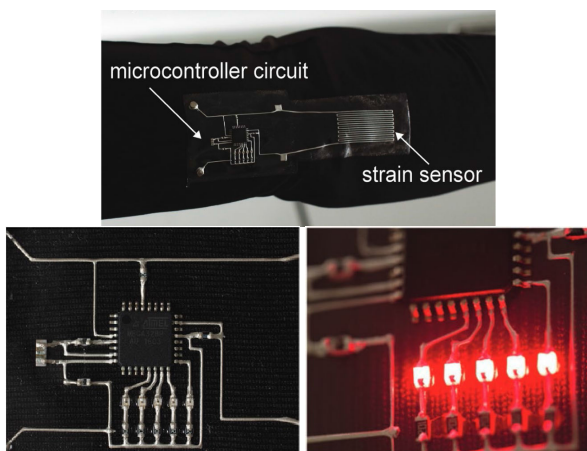
One multimaterial printed electronic device also worked as a wireless pressure and temperature sensor within a shoe's insole [156]. A range of solvents, particle loading, and binder materials are used in conjunction with
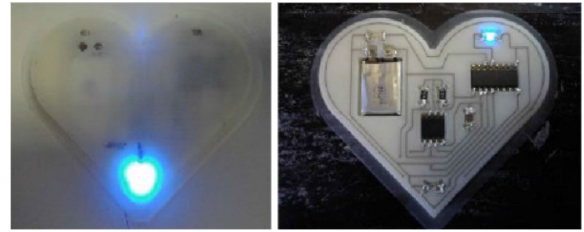

(a)

(b)

Fig. 19. *(a) Photograph of the printed wearable wristband. (b) Cycling stability test result of the proposed device [154].*

Fig. 21. *Photograph of the printed wireless pressure and temperature sensor within a shoe's insole [156].*

Fig. 23. *Photograph of the 3-D-printed heart-shaped timing circuit [158].*

inkjet, aerosol, and extrusion printheads to deposit tens of thousands of layers of material. Epoxies, acrylics, and polyurethanes—cured by heat or UV light when applied between layers—are the primary materials of interest for external structures. Conductive silver paste is extruded to create hybrid sensors in the circuit fabrication process. A 3-D-printed insole with integrated temperature and pressure sensors and a wireless communication chip for data transmission is shown in Fig. 21.

Some electronic devices were implemented by embedding active modules and *LC* components into the cascade circuits of active systems, which were conveniently and quickly fabricated by multimaterial printed technology. In [157], a microprocessor, LEDs, capacitors, resistors, and crystals were integrated into a printed circuit to form a wearable soft electronic device. The designs were prototyped using an integrated AM platform combining automated surface mount electrical component pick and place with DIW on conductive and dielectric elastomeric materials. This technique allows for the direct printing of conductive electrode inks and insulating substrates in a predetermined arrangement. Then, to create the desired electronic circuit, individual passive and active electronic
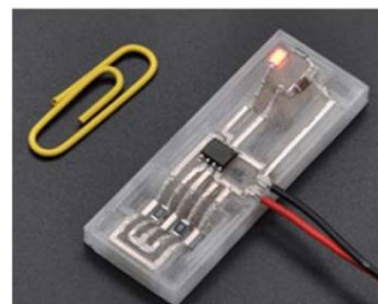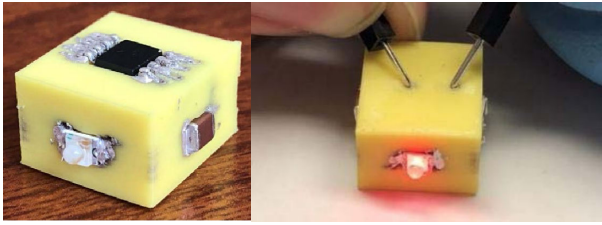
components are picked up using a blank nozzle, placed onto a substrate, and deposited into the appropriate area. Soft electrical devices are created by connecting these components using printed conductive traces. A sophisticated microcontroller device that included strain sensors and a large-area soft sensor array was produced to test the design methodology in Fig. 22. The wearable electronic system is designed using an ATMEGA328 chip to read sensor data and output the readings onto five LED indicators.

In [158], a 3-D-printed heart-shaped timing circuit was generated using the 555-timer circuit as the controller to demonstrate the reliability of printing conductive pastes and thermoplastics, as shown in Fig. 23. Since the timing circuit is made entirely digitally, a computer numerical control (CNC) printing method is employed to create a set of ready-to-print files and adjustments to future circuits in a matter of minutes, from design to fabrication to finished parts. A single machine can automatically print all the required layers in approximately 30 min. The 555 timer circuit also utilizes the manufacture of blanking LED systems with multimaterial 3-D-printed feeding networks [159]. It combines selective electroless plating, 3-D printing, and dual-material FDM. The 3-D-printed free-form plastic constructions can be selectively electroplated with thin nickel alloy coatings. In Fig. 24, the final device is displayed. Moreover, the LED blinks are achieved using a working 555 timer circuit implemented using custom software and a hybrid 3-D printing process [160]. Microdots of DuPont CB028 silver paste and FDM of ABS plastic were utilized in the circuit's fabrication. After processing, components

Fig. 22. *Photograph of the printed sophisticated microcontroller device, matrix part, and real-time function [157].*

Fig. 24. *Photograph of the 3-D-printed blanking LED systems [159].*

Fig. 25. *Image of the 3-D-printed LED system and device demonstration with power [160].*

must be manually added due to equipment restrictions. The conductive epoxy is used to join the parts. In order to illustrate the correct operation of the circuit, Fig. 25 exhibits the device attached to a power source. These above works demonstrate that the adaptable and compatible multimaterial 3-D printing technique can cooperate with active modules and *LC* components.

IV. EMERGING 4-D PRINTING TECHNOLOGY

This section begins with introducing the concept and underlying mechanisms of 4-D printing. On such a basis, SMPs and SMAs, identified as the most typical smart materials, are discussed in Sections IV-A–IV-C regarding their material properties and printing techniques.

A. Concept of 4-D Printing

Developed based on 3-D printing technology, 4-D printing further incorporates the dimension of time, thereby imparting dynamic properties to the printed structures [161], [162], [163], [164], [165], [166], [167], [168], [169], [170], [171], [172], [173], [174], [175]. Specifically, when exposed to external stimuli such as temperature, humidity, light, or electric and magnetic fields, the shape and properties of the 4-D-printed objects evolve along with time [162]. The 4-D printing is inherently characterized by implementing smart materials [167], including SMPs and SMAs, shape-memory hydrogels (SMHs), hydrogels, polymers with embedded active materials (magnetic, photothermal convertors, etc., [164], [165], [166], [167], [168], [169] and liquid crystal elastomers (LCEs) [163], which facilitate adaptation and deformation in response to specific stimuli. Due to its versatility, 4-D printing finds applications in a wide range of fields, such as aerospace [176], electronics [111], soft actuators [177], [178], [179], and biomedical sector [180], [181].

Fig. 26 illustrates the relationship between 3-D and 4-D printing technologies. The 4-D printing inherits the requisite equipment and fabrication processes as utilized in 3-D printing [182], such as FDM, SLA, DLP, and DIW. Especially in terms of AM adopting metallic materials, techniques including direct energy deposition (DED), SLS, selective laser melting (SLM), and electron beam selective melting (EBSM) are applicable for 4-D printing [161], [183].

Different printing methods exhibit distinct advantages regarding compatibility with specific hardware and

applications [169]. The choice of a feasible printing method is determined by the nature of the stimulus for the printed structure, as smart materials must be compatible with specific AM technologies. For example, FDM is a well-established printing technique extensively utilized in both industrial and laboratory settings for its relatively rapid printing speed [184], [185]; however, the FDM printer, which works by heating filaments above their melting point, can result in invalidation and degradation of temperature-sensitive composition in the filaments [186]. Printed structures that are actuated by heat stimulus are typically produced using the SLA or DLP method, which employs commercially available and laboratory-prepared materials, offering faster printing speeds and higher resolution than their counterparts [111], [187]. DIW is an AM technique featured by extruding ink through a syringe [186], with the efficiency and quality of the extrusion heavily dependent on the viscoelastic properties and curing process of the polymeric inks; thus, careful selection and configuration of printing materials, as well as the precise setting of printing parameters, are critical [188], [189]. Small molecules or nanofillers can be integrated into printing materials to induce or enhance the reactivity [186], [190]. Currently, DED and LPBF techniques (e.g., SLS, SLM, and EBSM) are widely recognized for 4-D metal AM [161], [162], [183], [191]. Printing with SMAs, such as NiTi [170], can be more challenging compared to other nonsmart metal materials, where material composition and the printing process become critical determinants of the shape memory behavior [171], [192]. Considering the lower evaporation temperature of nickel than that of titanium, a higher nickel content during the formation process is essential to secure the phase transformation behavior [193], [194]. Performing SLM printing in a chamber filled with inert gas can effectively mitigate the issue of impurities in NiTi alloys [183]. Shape preprogramming refers
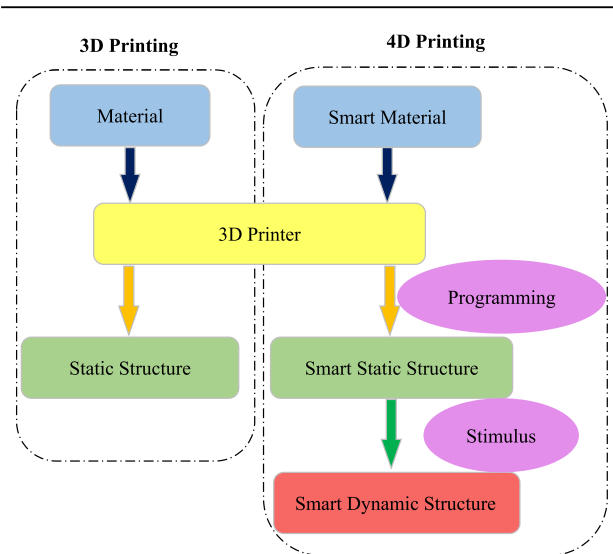
Fig. 26. *Variance of 3-D printing and 4-D printing.*

to the active control of temperature gradients and residual stresses through meticulous adjustments of the printer settings and the dimensions of printed parts. It allows precise manipulation and tailoring of the preprogrammed shape-memory behavior [195], thereby integrating the temporal dimension into the printed static structure.

The 4-D printing differs from 3-D printing in its ability to undergo structural transformation driven by external stimuli [161], [162]. This necessitates an insight into the underlying mechanisms of intelligent and dynamic structures that exhibit SMEs, which refer to the ability to revert from a deformed shape back to its original shape [162], [180]. This recurring transformation process is termed the shape-memory cycle [196], [197], [198]. While SME is not uncommon, it is difficult to either fix temporary shapes or restore fixed temporary shapes to their original states because of the low elastic deformation of most materials [198]. Conversely, materials with exceptional fix-restore transitions can be generally referred to as SMMs.

The process of cyclically transforming SMMs between temporary and permanent shapes is defined as training or programming [199], [200]. Diverse SMMs exhibit varying degrees of programmability; for example, hydrogel materials have limitations in terms of multiple reprogramming cycles [201]. In contrast, LCEs can achieve bidirectional and reversible 4-D deformation. By adjusting the polymer network, LCEs can thermally drive reversible shape changes. These properties allow LCEs to undergo complex, multidirectional transformations, making them highly effective for applications requiring repeated and adaptable shape changes. The programming mechanism is analog to a triggerable "switch" that, upon exposure to external stimuli and force distribution, activates to facilitate the transformation of the structure into a desired shape, which is effectively "frozen" in place once the stimuli are removed [199], [200], [201], [202]. In various shape-memory cycles, SMMs can temporarily stabilize in a wide and unrestricted range of forms [200]. The principles of SME in SMA and SMP are, however, different [198], [202], [203], [204], [205]. Exposed to the same external stimulus, thermally responsive SMPs and NiTi-based SMAs [206], [207] are, respectively, exemplified in Sections IV-B and IV-C.

The switching mechanism of thermo-responsive SMP typically involves a direct temperature change [208], based either on the glass transition temperature (T_g) or the melting temperature (T_m) of amorphous polymers or on the crystallization transition temperature (T_{cryst}) of semicrystalline polymers [209], [210]. Fig. 27 illustrates the shape-memory cycle of thermo-responsive SMP [180]. The permanent crosslinks (i.e., net points) can be classified into either chemical (i.e., covalent bonds) or physical (i.e., ionic or hydrogen bonds) [203]. The amorphous polymer is initially deformed at a temperature above T_g, where polymer chains exhibit greater mobility, and then cooled to below T_g while maintaining a constant deformation stress. When the external force is relieved, the molecular
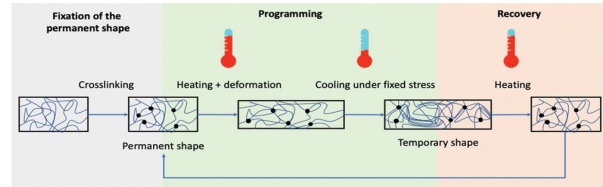

Fig. 27. *Shape-memory cycle of thermo-responsive SMP [180].*

motion of the polymer chains and segments is frozen. Thus, the temporary shape is preserved [197]. Semicrystalline polymer operates through a similar mechanism: upon cooling to below T_{cryst}, the crystalline regions form and act as additional anchoring points by crosslinking, inhibiting the polymer chains from slipping. When heated above the response temperature, SMP structures recover to their original shape as the polymer chains regain fluidity (or crystalline regions melt). SMPs can restore strains up to 300% through unloading and heating [189], [211].

Regarding NiTi-based SMAs, three crystal structures exist: twinned martensite, detwinned martensite, and austenite [212], [213], [214]. Martensite (the low-temperature stable phase) gradually transforms into austenite (the high-temperature stable phase) when heated, and the reverse process occurs upon cooling [214]. Specific temperatures are identified, as illustrated in Fig. 28 [212], including the austenite start temperature (A_s), austenite finish temperature (A_f), martensite start temperature (M_s), martensite finish temperature (M_f), and the highest temperature induced by martensite strain (M_d) [195]. The above transformation temperatures are significantly affected by the composition of NiTi-based alloys and printer settings [194]. The SMEs of SMA can be categorized into one-way SME, two-way SME, and superelasticity (SE) or pseudoelasticity (PE) [205], [214]. The one-way SME describes the ability of an SMA to "memorize" a macroscopic permanent shape in the
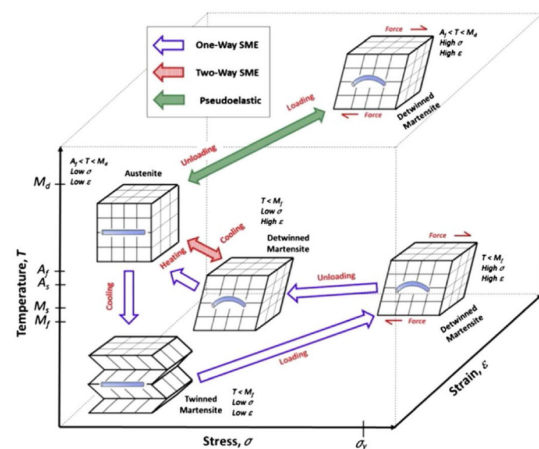

Fig. 28. *SMA phases and crystal structures [212].*

austenitic phase and to revert to it from a deformed temporary shape upon exposure to stimuli [162], [212]. Through unloading and heating, NiTi-based SMAs can recover strains of approximately 8% [214]. The remaining will lead to permanent plastic deformation [212]. The two-way SME refers to mutual transitions between two permanent shapes, respectively, memorized in martensite and austenite [214]; however, its range of recoverable strain is limited to only 3% [215], [216]. SE is the rubber-like behavior of SMA (e.g., NiTi), enabling it to revert to its original shape upon unloading even after significant deformation, whose strain capability is several times greater than ordinary metal alloys [205], [217]. However, SE only exhibits within a specific temperature range from A_f to M_d, with the maximum recovery ability occurring near A_f [212].

## B. SMPs and Printing Process

The closed-loop 4-D printing will be applied to implement SMPs, which can be programmed and deformed into temporary shapes and restored to their original shapes upon exposure to external stimuli such as heat of light. The closed-loop 4-D printing is an enabler of smart AME devices. The work presented in [177] and [178] provides detailed discussions on closed-loop 4-D printing as soft sensors and actuators that benefit the AME electronic designs. SMPs can be programmed and deformed into temporary shapes, which are subsequently restored to their original shapes upon exposure to external stimuli, such as heat or light [161], [172], [179]. The SME of SMPs can be improved or extended by precise control of the printer's settings and material compositions [161], [180]. Preprogramming, for instance, making the smart static shape curl along the printing direction, can be realized by adaptively adjusting the printer's parameters [190], [218], [219]. Further enhancement to the printer's feeding system or printing platform can facilitate the acquisition of desired shapes suitable for particular application scenarios [220], [221], [222], [223]. By configuring the composition of a smart material or blending it with other smart materials with different stimulating responses, more comprehensive or multiway SME can be achieved [199], [224], [225].

Dynamic shape transitions are primarily controlled by the printer, which can be precisely configured to mold various geometric components in the intelligent structure [186]. As shown in Fig. 29(a), four thin thermal-responsive sheets of the same size were manufactured at a uniform printing speed but distinct paths at angles of 0°, 30°, 45°, and 60°, respectively [218]. When immersed in hot water, these samples will exhibit different curved shapes along their printing paths. The characteristics and degree of bending also depend on the aspect ratio of the printed sample. Fig. 29(b) shows that thermal-responsive LCEs of different widths bend into different shapes after heating [219]. The 4-D-printed multimaterial microfixtures can remain closed during printing and then gradually
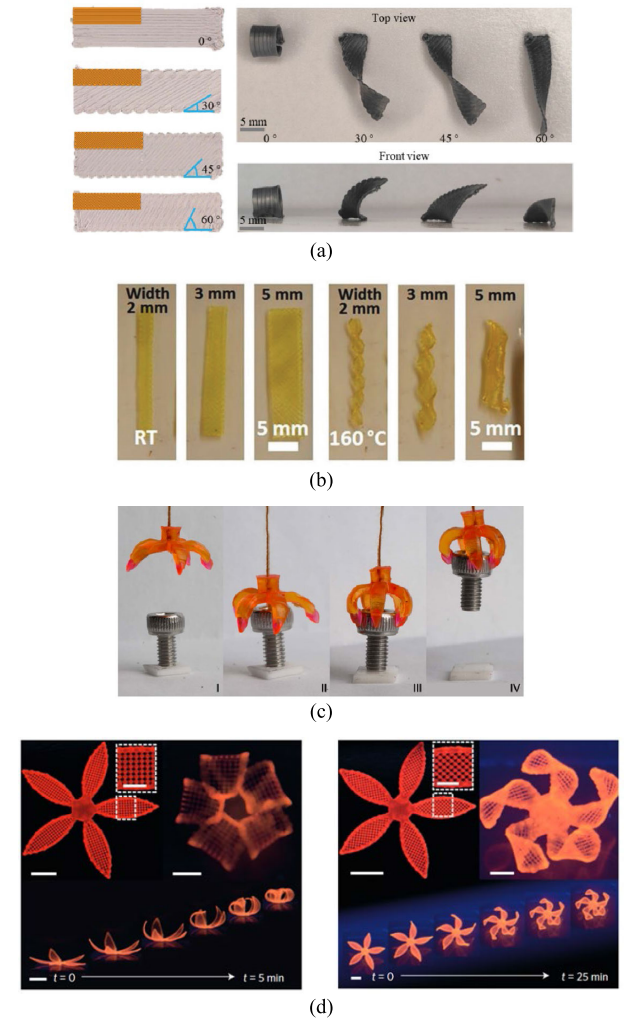
Fig. 29. *Four-dimensional-printed SMP samples deformed under temperature stimulation: (a) samples of equal size but different printing paths exhibit curved shapes [218]; (b) printed models of different widths bend into different shapes [219]; (c) process of a multimaterial grippers grabbing an object [189]; and (d) flower morphologies produced by biomimetic 4-D printing, according to the printing direction, the flowers curl (left) inward, and (right) spirally curl (scale bars: 5 mm and inset: 2.5 mm) [190].*

open after training, enabling them to grasp objects under stimulation [189], as demonstrated by the snapshots in Fig. 29(c). When exposed to environmental stimuli, the printed complex flower shapes in Fig. 29(d) can mimic the expansion process of their biological analogs in nature. These flowers are composed of double layers of 90°/0° and −45°/+45° with different orientations of the long axis of each petal. The composite hydrogel structures are designed with local anisotropic expansion properties dictated by the alignment of cellulose fibers along designated 4-D printing paths [190]. The arrangement, influenced by shear forces, and the degree of anisotropic expansion are contingent upon factors such as the nozzle's diameter and the printing speed.
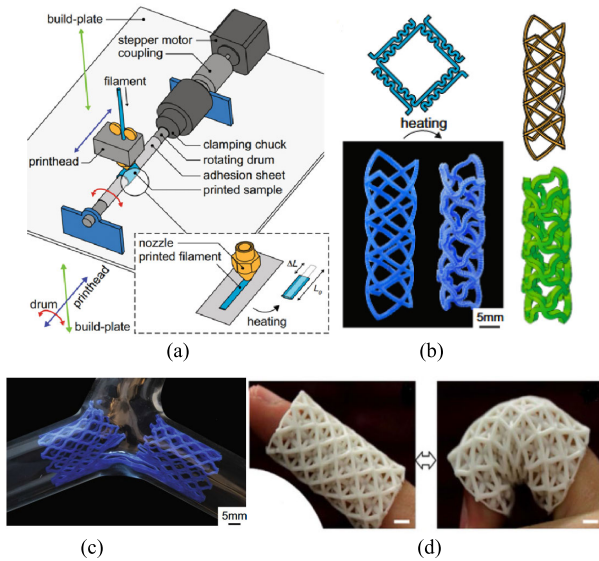
Fig. 30. *(a) Schematic of the methodology used to fabricate curved shape-shifting specimens [220]. (b) Shape-transformation behavior of cylindrical lattices with in-plane bending elements [220].*
(c) Deployment of a bifurcation stent within a model artery [220].
(d) Application in joint recovery support [221].

Samples can be fabricated layer by layer on a flat platform and programmed to form a 3-D structure, whereas they still retain 2-D characteristics. A new method for programming and manufacturing has been proposed to achieve 2-D to 3-D shape transformations, involving alterations to the construction platform that enable samples to be printed on a surface, as depicted in Fig. 30(a) [220]. By adjusting the layer thickness and printing temperature, the longitudinal shrinkage rate of the printed filament can be controlled, leading to the production of various samples for medical applications. These samples exhibited surface deformation behavior caused by buckling, as shown in Fig. 30(b). Fig. 30(c) and (d) shows the applications of these samples as supports in the arteries and around the joint [221].

Leveraging the progress in manufacturing shape-adaptive bending structures, the multiway SMPs have been explored [161]. Cold programming can be realized using grayscale digital light processing (g-DLP), which allows the deformation of a thermal-responsive SMP from its permanent shape to any temporary shape without heating [211]. On such a basis, a heterogeneous hinge module can be further included to print multiple materials by simply applying traction at room temperature. As shown in Fig. 31(a), different configurations can be encoded during the 3-D printing process by modularizing the variable distribution and orientation of hinges [211]. Thermal programming is performed in B1 and B2 regions to achieve shape recovery at 80 °C and 50 °C, while the B3 region is cold-programmed to exhibit elastic deformation [211]. Through localized adjustments to the hinge module and interlocking components with through-holes, various

complex 3-D geometries have been obtained, as shown in Fig. 31(b). An alternative approach is to use the FDM method with cold and hot programming. The testing indicates that the printed SMPs display elastic deformation at lower temperatures and exhibit SE, particularly under large deformations, at higher temperatures [222].

By incorporating different functional fillers into the polymer matrix, multifunctional shape memory composites (SMCs) can be developed with high tunability and remotely driven deformation [223]. Fe_3O_4 particles, when blended with other magnetic particles in polymers, facilitate the study of shape memory behavior that can be remotely driven through a magnetic field [223]. For example, by doping Fe_3O_4 particles into the shape memory PLA matrix, a biodegradable SMC blocker was designed and prepared [224], which can be remotely deployed under a specific magnetic field intensity. Vitro studies have also been conducted on printed SMC blockers to evaluate their feasibility in medical applications [223]. When NdFeB and Fe_3O_4 particles are added to the SMP matrix with a lower rubber modulus, SMP still has a relatively low driving modulus [225]. An adjustable T_g can be achieved by adjusting the ratio of rigid and flexible acrylic esters in magnetic shape memory polymers (M-SMPs). The magnetic induction heating of low coercivity particles softens the substrate. In contrast, high remanence particles have programmable magnetization curves that enable controllable deformation under the influence of the driving magnetic field and can lock in shape after removing the driving force [223]. Fig. 32(a) shows the working mechanism of an M-SMP cantilever in which NdFeB and Fe_3O_4 particles are embedded [225]. When exposed to a magnetic field, Fe_3O_4 particles cause the M-SMP to heat up, surpassing its T_g. By alternating the magnetic field directions, it is possible to quickly switch the bending direction of M-SMP from up to down. Then, it can lock the bending shape with high stiffness after removing B_h [225]. Moreover, the magnetization curve of M-SMP can be reprogrammed to achieve reconfigurable shape transformation through remagnetisation [223]. The magnetization curve of the four-arm M-SMP fixture is shown in Fig. 32(b), while Fig. 32(c) illustrates an M-SMP fixture lifting a 23-g lead ball.
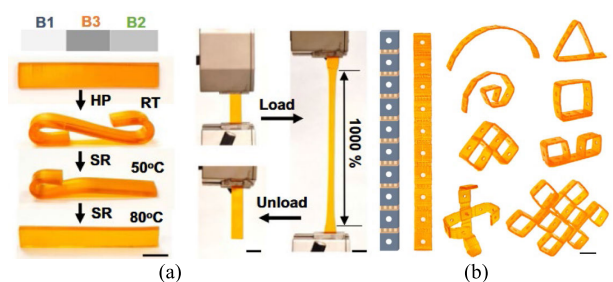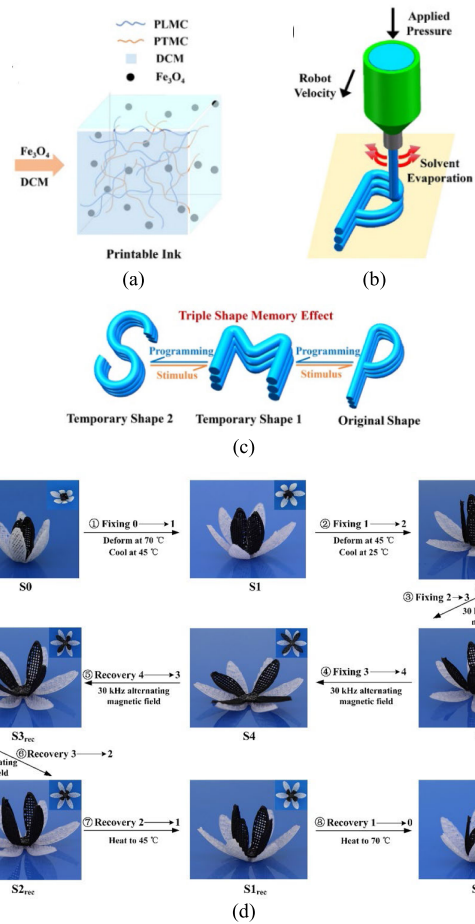

Fig. 31. *Cold-programmed shape-morphing structures (all scale bar is 1 cm). (a) B1 and B2 are thermally programmed at 80 °C and 50 °C, while B3 represents elastic deformation [211]. (b) Multiple complex adjustable hinge module configurations [211].*
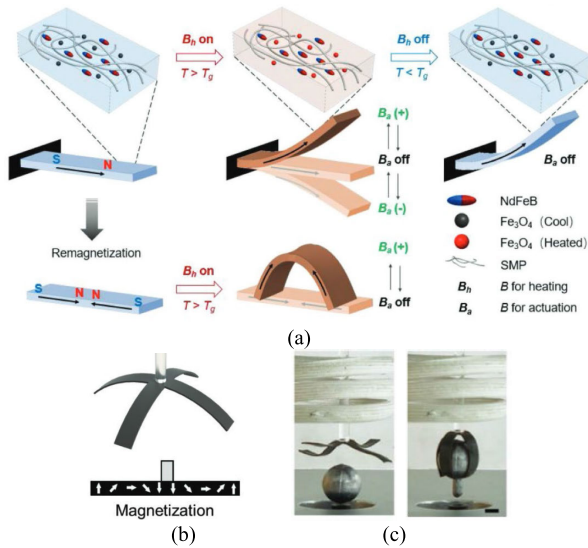
Fig. 32. *M-SMPs embedded with NdFeB and Fe$_3$O$_4$ particles [225]. (a) Working mechanism of M-SMP. (b) Magnetization curve of the four-arm M-SMP. (c) M-SMP fixture lifting a 23-g lead ball (scale bars: 5 mm).*

Fig. 33. *SMC materials have multiple SMEs [196]. (a) Composition of the printable nanocomposite ink. (b) Schematic of 4-D printing process. (c) Triple SME under an external heat stimulus, magnetic, or both. (d) Another example of multiple deformations of flower shapes printed with composite material.*

Wan et al. [196] achieved multiple deformation abilities by quantitatively characterizing shape recovery by gradually heating the composite materials. Due to the triple SME of poly(lactic-co-glycolic acid) (PLMC)/poly(trimethylene Carbonate) (PTMC) and PLMC/PTMC/Fe$_3$O$_4$, each part of the printed structure is optimized into two temporary shapes, and shape transformation is extended to five complex shapes, which have precise and local controllability under multiple stimuli [196]. Fig. 33(a) shows the composition of SMC materials with multiple deformation abilities. The SMP is printed layer by layer by placing the mixed ink material in a container and applying pressure, as shown in Fig. 33(b). Fig. 33(c) shows that through programmed 4-D printing, temporary shapes can be transformed into other letter shapes after being stimulated by heat, magnetism, or a combination of heat and magnetism [196]. Fig. 33(d) shows another example of multiple deformations of flower shapes made of 4-D-printed multiple materials under magnetic and thermal stimuli. Using the same 4-D printing method, conductive materials like carbon nanotubes were incorporated into PLMC to fabricate conductive SMCs [226], which are suitable for use in various sensors. When a voltage of 25 V is applied, the printed structure demonstrates remarkable shape-changing capabilities within 16 s, as depicted in Fig. 34 [226].

Alshebly et al. [227] present the development and applications of self-folding actuators. This article explores how single-material and multimaterial approaches can be used to create complex, shape-changing structures that respond dynamically to external light stimuli. The authors utilize a polystyrene (PS) pane to represent thermo-responsive SMPs, while the actuation hinges are made of printed chitosan hydrogel ink. Zolfagharian et al. [228] present the utilization of bio-inspired patterns in developing single-material self-morphing thermally controlled actuators.

C. SMAs and Printing Process

SMAs can also be programmed to temporarily hold specific shapes and revert to the originals when exposed to external stimuli [229]. Fig. 35(a) illustrates a superimposed image of a NiTi sample recovering its original flat
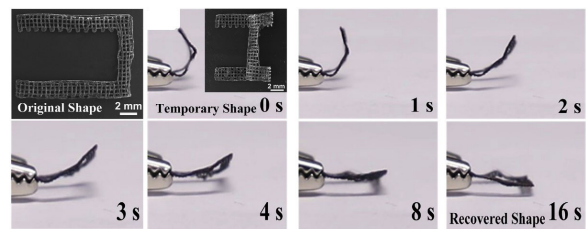
Fig. 34. *Shape recovery process of the printed folding bracket at a voltage of 25 V [226].*
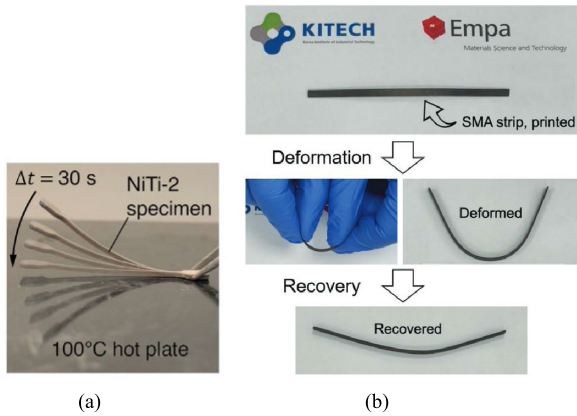
Fig. 35. *Four-dimensional-printed SMA samples. (a) Overlay diagram of NiTi SMA: bent patch on a hot plate for shape recovery [230]. (b) Shape programming and recovery process of Fe-based SMA strip [229].*

shape on a 100 °C hot plate within 30 s [230]. Similarly, Fig. 35(b) shows the shape recovery process of a Fe-based SMA strip: after programming (i.e., manual bending and deformation), the strip is heated to 300 °C using a hot air gun [229]. However, compared to SMPs, SMAs exhibit limitations in terms of printing ability and shape transition at the glass transition temperature [231]. To be specific, SMPs can achieve strains up to 300%, while SMAs typically reach a threshold of only 8% [212], [215]. Although the phase transition temperatures of SMPs are relatively lower, SMAs exhibit more significant transformation hysteresis and operate over a broader range of deformation temperatures. Moreover, SMAs boast higher stiffness and strength, surpassing SMPs by one to two orders of magnitude [232]. The elastic modulus and yield strength of SMPs typically do not exceed 1 GPa and 30 MPa, respectively. In contrast, Fe-based SMAs demonstrate a significantly higher elastic modulus of approximately 200 GPa, and higher tensile strength, potentially surpassing 1000 MPa [232]. Furthermore, SMAs also exhibit PE, which allows for the immediate reversal from deformation once external loads are removed without needing external temperature intervention [215].

LPBF is the predominant technology used for SMA-based AM [170], [171], which is not only feasible for the commonly seen NiTi, but also capable of producing high-temperature SMAs such as CuAlNi [191], iron-based SMA [229], [233], [234], [235], and magnetic NiMnGa SMA [236]. According to CAD data, this technology utilizes a high-power (HP) laser beam to selectively melt metal powder layer by layer until the final part is formed [229], and the processing flow is shown in Fig. 36(a). Fig. 36(b) presents a diagram of a novel partitioned repetitive laser scanning strategy [171], which adjusts the functional properties of NiTi alloy by resintering predesigned areas in the secondary scanning rather than through the interaction between the laser beam and powder. The characteristics

of samples manufactured by LPBF can be summarized as follows [171], [232]: 1) nonequilibrium microstructure with high supersaturation and metastable or nonstationary phases; 2) multiple process parameters can together affect heat and mass transfer processes (e.g., laser power, scanning speed, hatch spacing, and layer thickness); 3) generate high residual stress resulting in poor machinability; and 4) exhibiting lower toughness and fatigue performance. Therefore, it is critically important to investigate the microstructure and properties of NiTi samples fabricated using LPBF technology.

By examining the microstructure, chemical composition, phase transition temperature, and mechanical properties of NiTi samples manufactured with LPBF, Chen et al. [232] successfully prepared two completely dense samples using low-power (LP) and HP processing parameters. They experimentally characterized the microstructures, phase transition temperatures, damping capabilities, and storage moduli based on the obtained NiTi powder and NiTi samples produced via LPBF and then conducted a series of detailed analyses of precipitation behavior, oxygen absorption, phase transition, and mechanical properties. After necessary preprocessing procedures, scanning electron microscopy (SEM) and optical microscopy were utilized to analyze the microstructures comprehensively, differential scanning calorimetry (DSC) was employed to precisely determine the phase transition temperatures, and X-ray diffraction (XRD) was used to investigate the phase compositions. The metal element composition in the
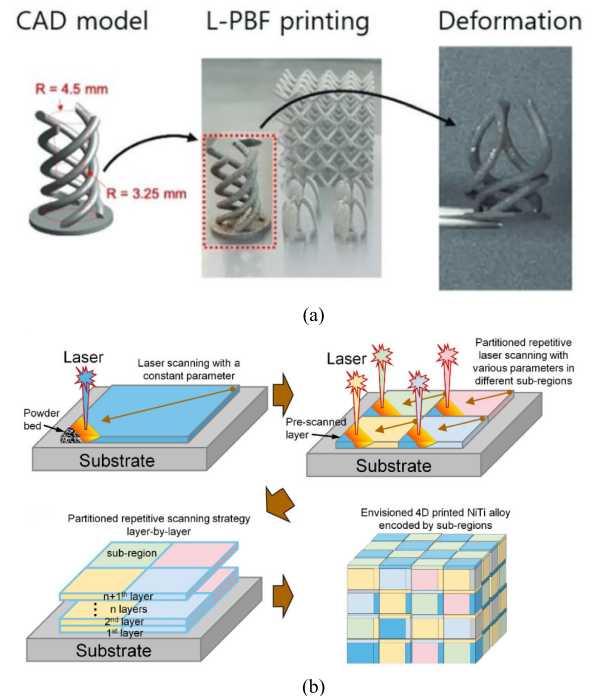
Fig. 36. *LPBF technology: (a) machining process flow [229] and (b) schematic of a partitioned repeated scanning strategy [171].*

(a)

(b)   (c)
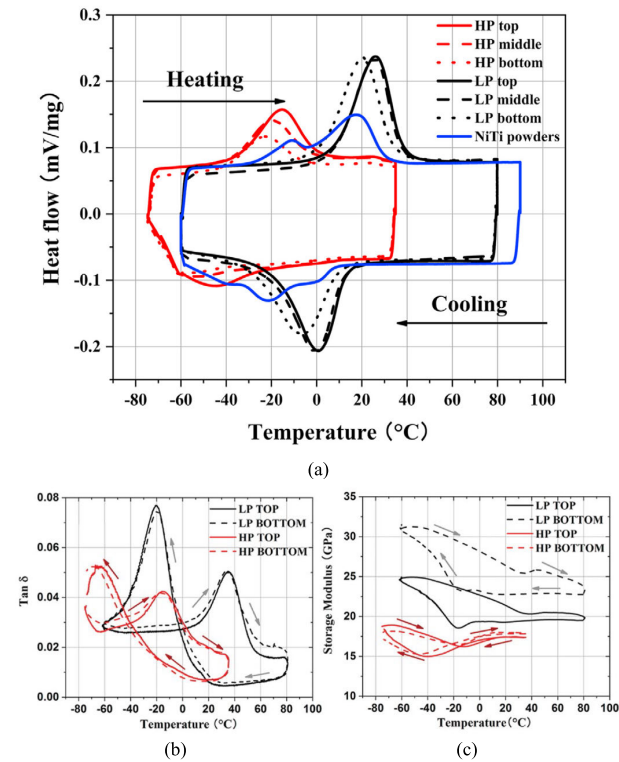
Fig. 37. *Sample characterization: (a) DSC characterization curve; (b) damping factor; and (c) storage modulus measured by the DMA approach [232].*

samples was analyzed using inductively coupled plasma atomic emission spectroscopy (ICP-AES), and the oxygen and nitrogen content were precisely determined using the Leco combustion method [232]. To evaluate the damping properties of the NiTi prepared by LPBF, a dynamic mechanical analyzer (DMA) was employed. It becomes evident that the phase transition behaviors and mechanical properties differ between SMA samples processed using LP and HP settings. As shown in Fig. 37(a), the DSC curve of NiTi powder has multiple peaks during heating or cooling, indicating multistage transformation, whereas only one peak is observed in the HP or LP sample [232]. The curves for the damping factor and storage modulus measured by DMA are shown in Fig. 37(b) and (c). The LP sample exhibits a higher amplitude in both the storage modulus valley and the internal friction peak, where the storage modulus is notably higher in the bottom portion [237]. The mechanical properties of HP samples are relatively insensitive to position. The variation in storage modulus suggests a difference in the austenite and martensite mix within the samples.

Improving the microstructure is of great significance to broadening the functions and promoting the applications of SMAs as intelligent components. In the LPBF process, employing the same energy density for various combinations of power and speed can result in variations in printing adaptability, microstructure, phase transition temperature,

and mechanical properties [170]. For example, the phase transition temperature and evaporation of Ni element are affected by scanning speed in the sample, while porosity and grain size are regulated by laser power [238]. Empirical practice at higher economic and labor costs can acquire satisfactory process parameters. Therefore, predictive models, optimization algorithms, and systematic methods are needed to obtain the optimal parameters in AM. Furthermore, the semianalytical design method, which combines experimental validation and machine learning techniques, has become one of the most effective approaches for determining the process window.

During the LPBF process, grain growth in the NiTi alloy occurs in the direction of heat dissipation. Grains grow from the boundary to the laser spot since the melting area has a higher temperature [239]. The area of the melting pool becomes wider with higher laser power input. The temperature gradient disparity between the region's periphery and interior leads to rapid nonequilibrium solidification. Lower laser power settings result in finer grain sizes in the sample and a narrower grain size distribution. Conversely, increasing the laser power gradually facilitates the formation of columnar crystals. More specifically, ultrafine honeycomb grains form at the edge of the melt pool due to the high cooling rate, while good dendritic grains form inside [239]. Appropriate scanning strategies, such as lower scanning speed and layer height, would contribute to firmer texture in NiTi parts.

The phase transition temperature of NiTi is sensitive to the alloy composition: the temperature at which martensite begins to transform will decrease by about 10 °C if the Ni content only increases by 0.1% [240]. In other words, the LPBF process window for NiTi alloy is very narrow [241]. Considering the lower boiling point of nickel (2913 °C) compared to titanium (3287 °C), the equilibrium vapor pressure of nickel is higher than that of titanium [242]. However, a slight change in alloy composition is inevitable in the LPBF, leading to significant changes in SME and mechanical properties [237]. Induced by impurities (such as O and C) and Ti-rich precipitation, the formation of the Ti-rich second phase can alter the Ni content of the main matrix, thereby affecting the phase transition temperature [239]. The presence of O can affect the grain boundary characteristics in the quasi-amorphous layer, which should be suppressed in the process-forming chamber to avoid compromising the ductility of NiTi [241].

In practice, even in the most satisfactory samples obtained through careful optimization of process parameters, local defects still can be observed upon inspection at the interlayer interface, which include transgranular fractures with small microcracks and dimples, voids, and regions at the sample's edges where a significant amount of unmelted powder accumulates [243]. Heat treatment can diminish the permanent plastic deformation resulting from dislocation slip during the stress-induced martensitic transformation, leading to near-perfect SE and nearly reversible temperature changes. The titanium oxide coating formed

Table 2 Overview of 4-D Printing Approaches, Materials, Stimuli, Response Times, and Applications

Ref.	Printing Technology	Materials	Company	Cost	Stimuli	Response Time	Applications
[219]	Direct Ink Writing (DIW)	Liquid Crystal Elastomers (LCE)	Wilshire Technologies Inc.	-	Temperature	80 ms	Actuator
[218]	Fused Deposition Modeling (FDM)	Shape Memory Polylactic Acid (SMPLA)/ Polycaprolactone (PCL)	Bing Additive Manufacturing Technology Inc., Dongguan, China	¥450 per kilogram	Temperature	2.5 s	Bio-inspired Gripper
[226]	Direct Ink Writing (DIW)	Poly (lactic-co-glycolic acid) (PLMC)/ Carbon Nanotube (CNT)	Jinan Daigang Biomatereial Co. Ltd, Aladdin Industrial Inc., Nanocyl, Sigma-Aldrich	-	Voltage	16 s	Sensors
[247]	FDM/ Inkjet Printing	Shape Memory Polylactic Acid (SMPLA)	SMP Technologies Inc.	$0.46 per gram	Temperature	50 s	Electromagnetic Device
[262]	Solvent Casting (SC)	Silver-Coated Cellulose Nanofiber/Polylactic Acid Composite (Ag@CNF/PLA CPNs)	Laboratory	-	Voltage	20 s	Multifunctional Electrical Devices
[230]	Fused Filament Fabrication (FFFm)	Nickel-Titanium (NiTi) Powder	Eckart TLS GmbH, Germany	-	Temperature	30 s	Actuator
[232]	Laser Powder Bed Fusion (LPBF)	Nickel-Titanium (NiTi) Powder	TLS Technik GmbH & Co.	A$8000 per kilogram	Temperature	-	Influence of Printing Parameters on Samples

during this process helps retain the more volatile nickel. However, increased oxygen content in the heat-treated samples leads to the formation of $Ti_4Ni_2O_x$, which consequently impacts the phase transition temperature [244].

V. 4-D PRINTING SHAPE-MEMORY ELECTRONIC DEVICES

The 4-D printing has attracted a surge of interest in recent years. The majority of research activities are about SMMs, processes, biomimetics, and biomedicine [161], [162], [163], [164], [165], [166], [167], [168], [169], [174], [181], [183], [195], [196], [197], [206], [212], [213]. However, 4-D printing shape-memory electronic devices have not yet been comprehensively investigated to address the most recent advancements, let alone provide comprehensive and systematic guidance for designers in relevant research fields. An overview of 4-D printing electronics is shown in Table 2. This section aims to guide electronic engineers/researchers in integrating 4-D printing technology into electronic component designs by providing design guidelines, showcasing design examples, and exploring the potential applications and future directions.

A. Design Considerations

SMPs and SMAs are two major materials coupled with 4-D printing. The sustainability of developing shape-memory AME devices using 4-D printing is critical, as discussed in [245] and [246]. According to the open literature, SMP-based 4-D printing designs significantly surpass those related to SMAs, which can be attributed to the distinct advantages of SMPs, such as low cost, material programmability, excellent deformation performance, and diverse external stimulation methods [172], [247]. SMPs can attain various driving modes or multipath programming of shapes by incorporating different particles, rendering them a more versatile selection for 4-D printing

than SMAs [189]. The maximum recoverable strain, as the primary feature of SMMs, is approximately 8% for SMAs, while SMPs have reached a remarkable 300% according to the existing literature records to date [212], [215]. Apart from Fe-based, Cu-based, and Ni-based materials, the variety of available SMA materials is relatively limited. Even with enhancements achieved through blending other elements, the deformation requirements of many electronic devices still pose a challenge for NiTi-based SMA, considered the best candidate among all SMAs.

Nonetheless, SMAs have unique advantages and irreplaceability in specific application scenarios. For example, SMA materials possess exceptional mechanical robustness and corrosion resistance, making them extensively utilized in the medical field for designing bone or vascular stents [181]. SMA materials are inherently conducive and thus readily available for creating electronic devices, while SMPs typically require the combination of conductive particles, metallic coatings, or liquid metal to obtain conductivity [170]. In a wide deformation range, it can be difficult for SMPs to maintain dynamic conductivity during shape changes. Therefore, to leverage the benefits of SMMs when designing 4-D-printed electronic devices, a tradeoff between the deformation capabilities of SMPs and the conductivity of SMAs becomes essential.

The relatively small number of published articles indicates that 4-D printing technology is still at the early exploration stage in electronics; however, it holds significant potential [247], [248], [249], [250], [251]. The attributes of SMPs can facilitate the design of electronic devices with features including reconfigurability, multifunctionality, frequency adjustability, function switching, beamforming, and beam-steering. These functionalities can be achieved under simple external stimuli without complex feed networks or power splitters. Nonetheless, these approaches necessitate predesign and preprogramming
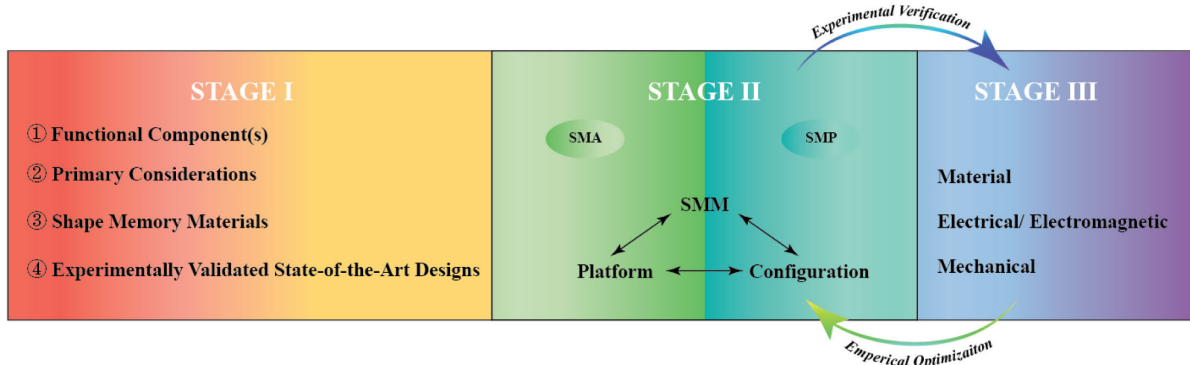
Fig. 38. *Critical stages throughout 4-D printing. Stage I focuses on the selection of SMMs. Stage II aims to properly set the printing platform with the selected SMA or SMP. Stage III includes a few tests that are significant indicators for optimizing the configurations in Stage II.*

and have limited application scenarios due to the need for specially designed shape recovery sequences with a thorough comprehension of specific materials. The differences across individual 4-D printing applications have led to a notable absence of systematic and comprehensive design guidance and processing methodologies.

In general, 4-D-printed electronic devices can be divided into three critical stages, as shown in Fig. 38: Stage I—design preparation and SMM selection, Stage II—printing configuration, device prototyping, and shape-memory training, and Stage III—shape-transformation experiment, reconfigurable functions evaluation. The experimental validation and empirical optimization iteration between Stages II and III are required to explore the most suitable printer settings for accurately replicating desirable samples.

1) *Stage I* encompasses four steps, further detailed in Fig. 39. First, ascertain whether the printed device with SMMs serves as an actuator or includes electronic functions. Priority is given to examining available stimuli sources and material characteristics for the former. SMAs are suitable for thermal, electrical, or magnetic stimuli, while SMPs can respond to heat, light, pH changes, and humidity. SMAs offer higher stiffness and more precise shape memory, whereas SMPs are more appealing regarding deformation range and cost. Balancing conductivity with deformation capabilities becomes crucial if the application extends beyond an actuator. Once the category of SMMs is decided, references can be found to the corresponding state-of-the-art examples, effectively serving as a source for emulation.

2) *Stage II* comprises three parts, as illustrated in Figs. 38 and 40(a): the selected SMMs, the accessible printing platforms, and the printer configurations, which further diverge into two paths based on the specific SMMs (i.e., SMA or SMP). The well-developed printing technologies for SMA include LPBF, DED, and binder jetting (BJ), while for SMP

FDM, SLA, and DIW are frequently used. The materials applicable to these technologies are, respectively, listed in the flowchart. The core technical configurations that influence preprogramming differ significantly between SMA and SMP in terms of SME, the material's mechanical strength, and the electrical, EM, and TL properties. It requires extensive experimental testing and experience accumulation since the parametric study may vary case-by-case in specific application scenarios. Although there is still a lack of analytical methods, the efficiency and reliability of this process have been enhanced with the advancement of artificial intelligence and machine learning.

3) *Stage III* includes three parallel validations, as shown in Figs. 38 and 40(b), to ensure that the results of 4-D printing meet expectations. The microstructural and material properties of the sample have to be examined using testing equipment. Electrical and EM features are evaluated from dielectric, conductive (either coatings or inner cores), and radiative aspects. Unlike training commercial SMMs with basic geometric shapes, the printing process can simultaneously achieve complex prototyping and functional training. The 4-D-printed samples can memorize their permanent shapes, which may or may not be the same as their temporary shapes during printing (such as compressed or folded). Given the complexity and difficulty of preprogramming, a cyclical iterative optimization process exists between Stages II and III.

Every step in the stages above is critical in designing and fabricating 4-D-printed electronic devices, as the choice of materials and the processes involved influence the SMEs. At the same time, the metallization impacts the functionality of the electronic devices. Achieving the necessary structural shape transformation and continuously optimizing the performance of the metal components to produce functional electronic devices requires meticulous control over materials and processes. Taking the following hybrid
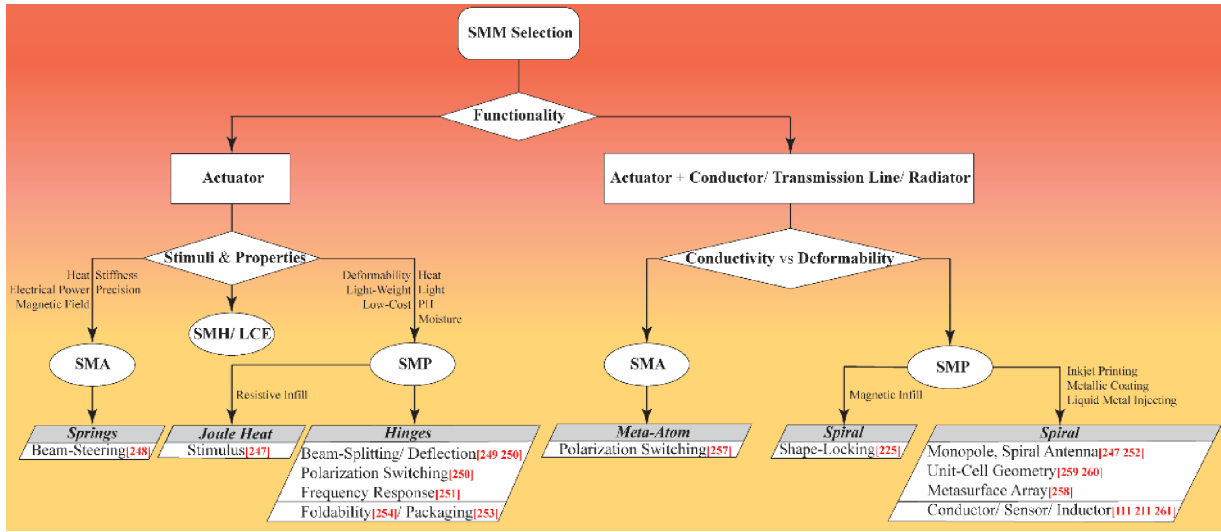
Fig. 39. *Detailed decision-making flowchart for selecting SMMs. It starts with acknowledging the functionality of the 4-D-printed sample and then figuring out the primary consideration on such a basis. Upon selecting the suitable SMM, it directs toward experimentally validated designs for further insight and information.*

4-D SMP EM device as examples [225], [247], [252], the SMP can be used as a substrate and conductive silver wires, which are printed to achieve frequency reconfiguration.

According to Stage I, printable materials should be chosen based on the shape change and stimuli involved. For instance, in [225], magnetic particles (i.e., Fe_3O_4 and

(a)

(b)
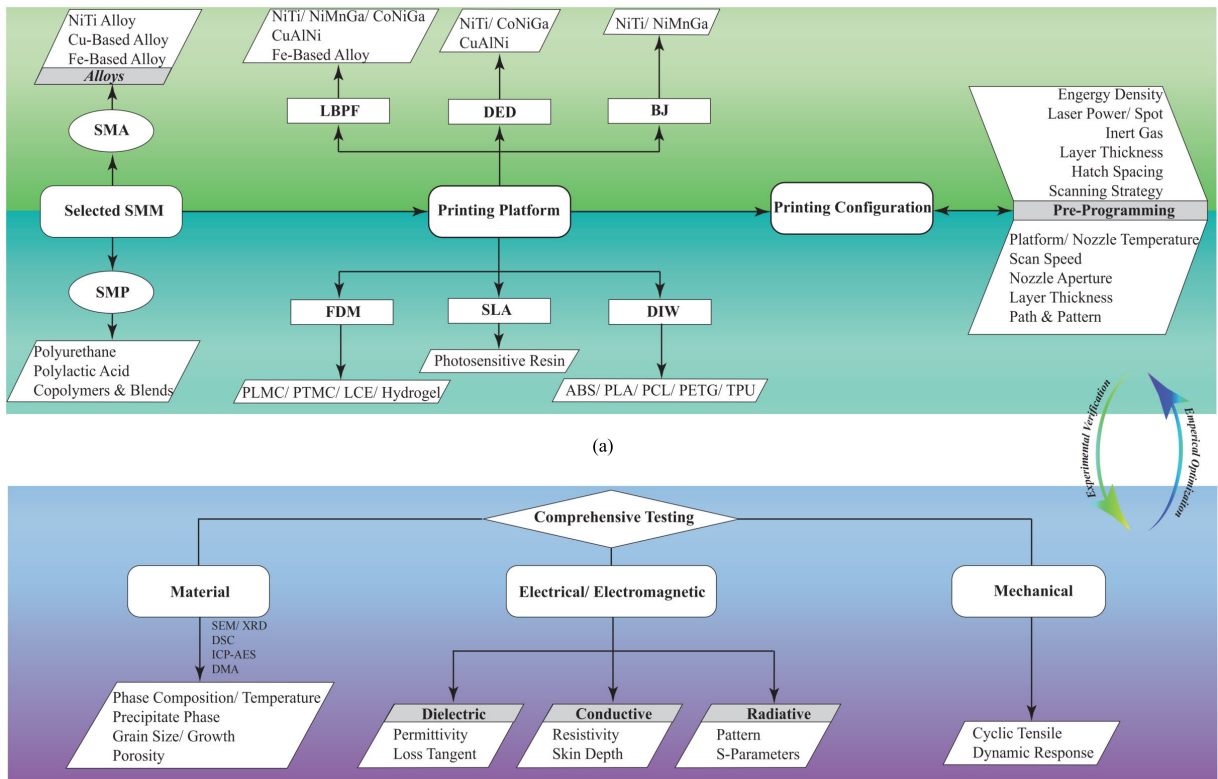
Fig. 40. *Four-dimensional printing procedures, and experimental verifications of the printed samples. (a) Stage II includes three interdependent parts, namely, SMM, printing platform, and printer settings. The printing techniques and preprogramming configurations are, respectively, listed in the upper and lower paths for SMA and SMP. (b) Stage III encompasses three parallel tests for material characteristics, electrical and EM properties as well as SME. There is an iterative optimization process between Stages II and III.*

NdFeB) were incorporated into resin to obtain magnetic materials, allowing shape changes under the influence of a magnetic field, thereby achieving gripping functionality and frequency-reconfigurable antennas. Fe_3O_4 particles are heated under a magnetic field for shape locking and unlocking, while NdFeB particles are magnetized into a predetermined distribution to achieve programmable deformation. The material preparation involves adjusting the composition ratio of rigid and flexible acrylic esters in the resin to control the glass transition temperature (T_g) to achieve the desired working temperature. Commonly used temperature-responsive materials can be obtained by purchasing commercially available materials [247]. The sintering process becomes crucial when inkjet printing conductive shapes on SMP. Two different sintering methods were used, namely, soft and hard baking, using hot plates and ovens. Soft baking can reduce substrate strain, while hard baking can ensure conductivity.

Stage II often requires accumulating a considerable amount of printing experience to obtain the optimal programming solution for achieving the desired shape memory structure. The design of shape memory deformation relies on the printing process, making precise control of nozzle aperture and printing speed crucial. The printing direction of each layer and differences in internal filling also impact the direction and degree of shape bending and the residual stress accumulation during the cooling process. A thorough investigation of the 4-D printing parameter settings under this shape memory deformation is discussed in the literature [191], [218]. When using commercial SMP as the raw material, parameters can be initially set based on the manufacturer's recommendations, which suggest a printing temperature of 210 °C, a bed temperature of 100 °C, a layer height of 0.1 mm, a bottom layer thickness of 300%, and a printing head speed of 20 mm/s [247].

Further adjustments to the material and printing parameters can be made as needed. In [247], when SMP is used as a substrate for electronic applications requiring precise physical dimensions, greater emphasis is placed on its surface roughness and flatness. These features significantly affect the print quality of conductive silver wires. Inkjet-printed dielectric buffer layers on uneven printing substrates have been adopted to reduce the surface roughness of the initial programmable 4-D printing, thereby enhancing the RF performance. The surface roughness for pure 4-D printing and printing substrates with buffer layers is 77.9 and 0.041 μm, respectively [247]. Based on experimental experience, the printed conductive shapes were achieved using a single nozzle with a bed temperature of 45 °C, a spraying voltage of 40 V, and a droplet spacing of 35 μm [247].

In Stage III, experiments and testing are conducted on the processed samples to understand the material characteristics, ensuring they meet the design requirements for shape changes and electrical or EM performance. The first aspect involves measuring the processed
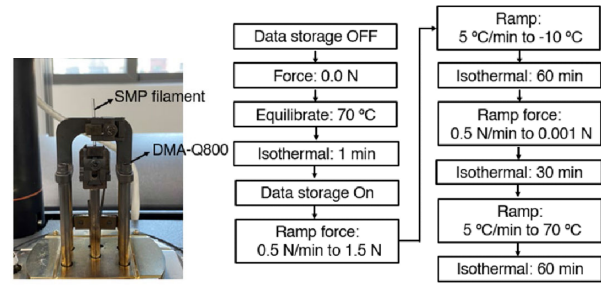

Fig. 41. *DMA device and measurement setup [247].*
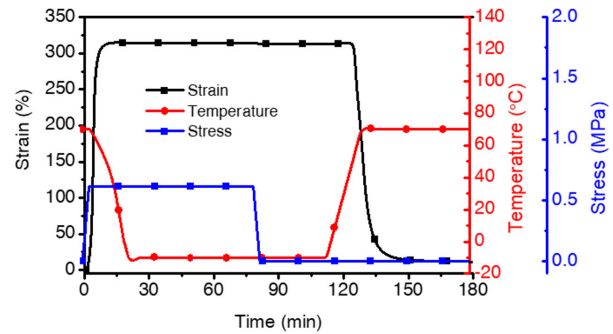
Fig. 42. *Characterization of shape memory performance of SMP using DMA [247].*

sample dimensions and conducting detailed analysis and measurements of shape changes. As shown in Fig. 41, a DMA measurement device is used to measure the shape persistence and recovery of the SMP samples, along with the measurement setup process [247]. Fig. 42 illustrates SMP's shape memory performance, which is characterized by DMA, with temperature, strain, and stress plotted as time functions within one cycle. In addition, it is necessary to measure the relevant Young's modulus, glass transition, and substrate transformation force points to analyze the mechanical deformation of 4-D-printed substrates. The substrate size and surface roughness also need to be tested and optimized to meet the high requirements of inkjet printing. Magnetized SMP's inductive heating characteristics also need to be measured, as illustrated in Fig. 43.

Fig. 43. *Schematic and measurement results of hysteresis loop measurement setup [225].*

Fig. 44. *Measurement results of electrical resistivity and conductivity of printed conductors for soft and hard baking [247].*
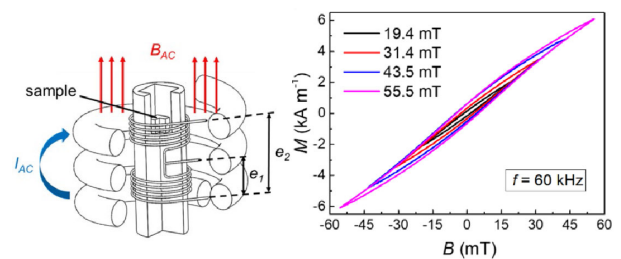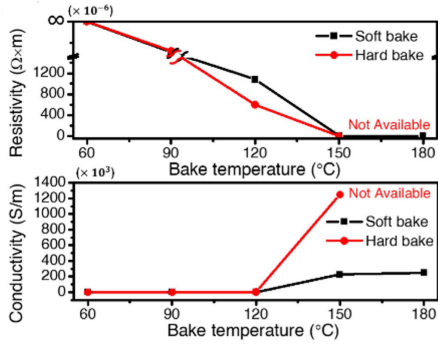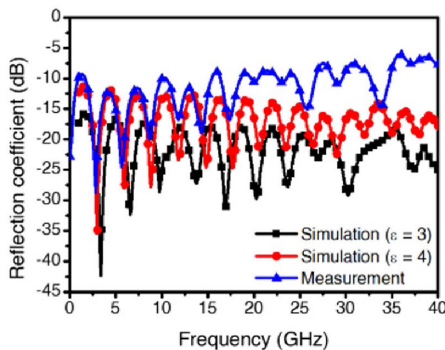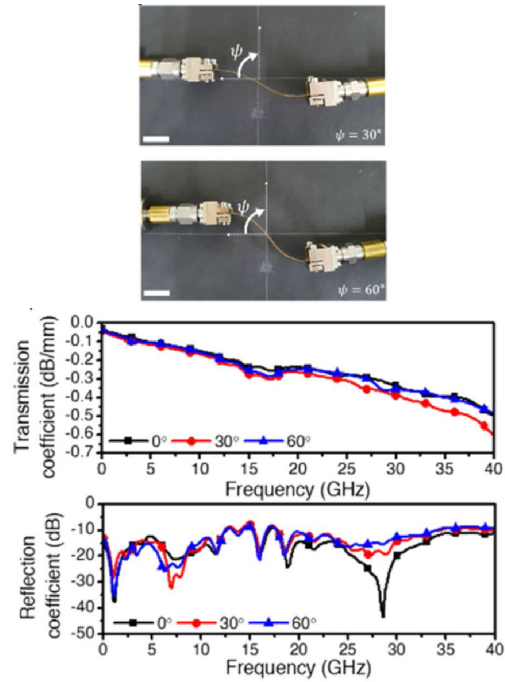
This includes measuring the high-frequency hysteresis loop, the schematic of its setup, and the hysteresis loop under different magnetic field intensities [225]. The second aspect involves measuring the electrical resistivity and conductivity of the printed structure. The electrical resistance of samples under different printing conditions is measured using a digital multimeter. This aims to achieve optimal conductivity by optimizing the baking temperature and the number of printing layers. Fig. 44 illustrates the measured conductivity relative to the baking temperature for both soft and hard bake methods under constant baking time (40 min) [247]. Next, measure the EM properties of the printed structure. EM simulation software can be used for the structure's EM simulation, but it is essential to know the electrical properties of the substrate. As shown in Fig. 45, the substrate's dielectric constant and loss tangent were measured. The transmission and reflection coefficients of the designed microstrip lines were measured at various bending angles and shapes by extracting measurement results. The schematic and measurement results of the waveform microstrip line structure are shown in Fig. 46. Furthermore, stability testing is essential to ensure the SMP electronic device functions reliably amid multiple memory shape transformations and recoveries.

Fig. 46. *Waveform microstrip line structure and measurement of transmission and reflection coefficients. Scale bar = 10 mm [247].*

The designed microstrip monopole antenna (MMA) was used to verify the memory repeatability. Fig. 47 shows that the operating frequency response of the mmA remains almost unchanged in 20 cycles compared to the initial state. However, a resonance deviation of 0.13 GHz is observed after 40 cycles [247]. Hence, they achieved electronic devices capable of consistently maintaining EM performance over 20 cycles.

B. Design Examples

Existing 4-D-printed electronic devices fall into two major categories: those that utilize SMMs exclusively for shape deformation and those where SMMs additionally function as electronic components.

Fig. 45. *Simulated and measured substrate EM characteristics results [247].*
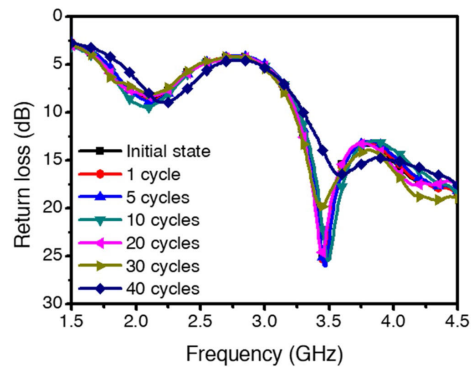
Fig. 47. *Measurement results of return loss of mmA during repetition period [247].*
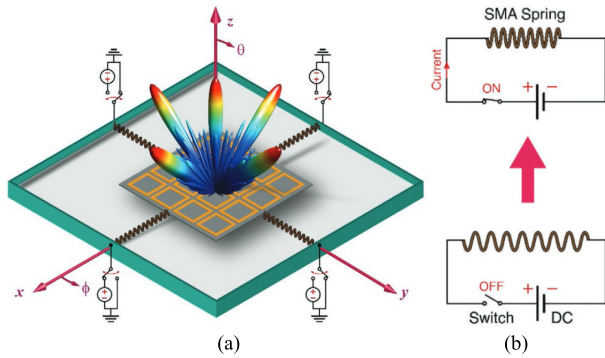
Fig. 48. *Metasurface with four independently controllable SMA actuators. (a) Electromechanically transformable beam-steering metasurface antenna. (b) Deformation mechanism of the SMA springs [248].*

Fig. 49. *Mechanically self-deformable 4-D-printed metasurface. The photographs of the printed prototype in (a) unfolding and (b) folding states. Comparison of full-wave simulated and measured results of LHCP and RHCP output waves in (c) folding and (d) unfolding states [249].*

When exposed to external stimuli, SMMs in the former category mechanically drive the other functional electronic components and thus can be utilized as actuators [247], [248]. Fig. 48(a) shows a metasurface antenna that obtains extensive beam-steering capabilities by applying dc excitation to four independently controllable spiral-shaped SMAs [248]. Diverse positionings of the metasurface become achievable by manipulating the power supply to the SMA springs, as depicted in Fig. 48(b), where biased voltages cause them to contract while remaining stretched in the absence of power. By precisely configuring the bias voltage and the duration of stimuli, the radiated beam covers 360° azimuthal directions with an elevation angle of ±30° [248]. Although the SMA springs are not manufactured through 4-D printing [248], their implementation showcases a viable method for designing SMA-driven smart antennas. By integrating 4-D printing technology into the fabrication of SMA components, more comprehensive mechanical deformations can be realized.

Similarly, embedding 4-D-printed actuators in between the unit cells of the metasurface allows a single metasurface to simultaneously accomplish beam splitting between left-hand circularly polarized (LHCP) and right-hand circularly polarized (RHCP) waves, as well as beam-steering [249]. As shown in Fig. 49(a), 4-D-printed SMPs connect the two rows of unit cells on the metasurface, which can be mechanically folded to the compact state in Fig. 49(b) and revert to the memorized unfolding state upon heating. The beam directions corresponding to the folded and unfolded states of the metasurface are depicted in Fig. 49(c) and (d), respectively. The beam splitting function is achieved through phase distribution on the metasurface, while the beam-steering capability of output waves depends on the spatial modulation mechanism [249]. Taking advantage of 4-D printing, a 2.4-GHz pattern reconfigurable origami antenna array was developed, as illustrated in Fig. 50(a) [250]. Inspired by foldable RF electronic devices, 4-D printing not only enhances the robustness of the device but also incorporates a heat-resistant core with
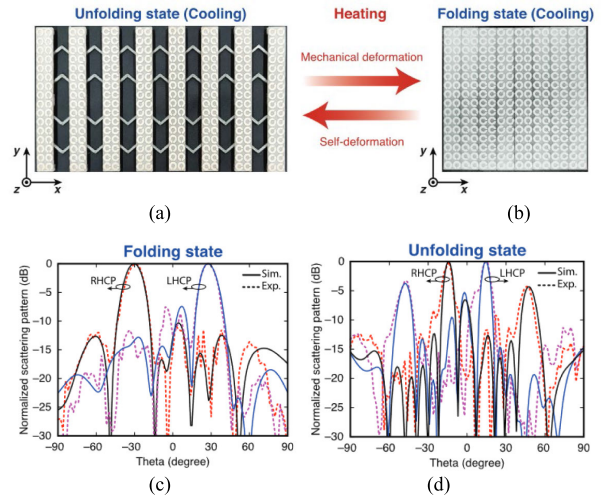
SMP hinges interconnecting the substrates of the antenna units [250]. These SMP hinges possess adequate stiffness to effectively mitigate twisting and breakage of the conductive layer on the surface. Through thermal stimulation, the antenna can achieve beam direction deflection up to 50° [250]. Fig. 50(b) demonstrates the shape deformation process of the 4-D-printed hinge.
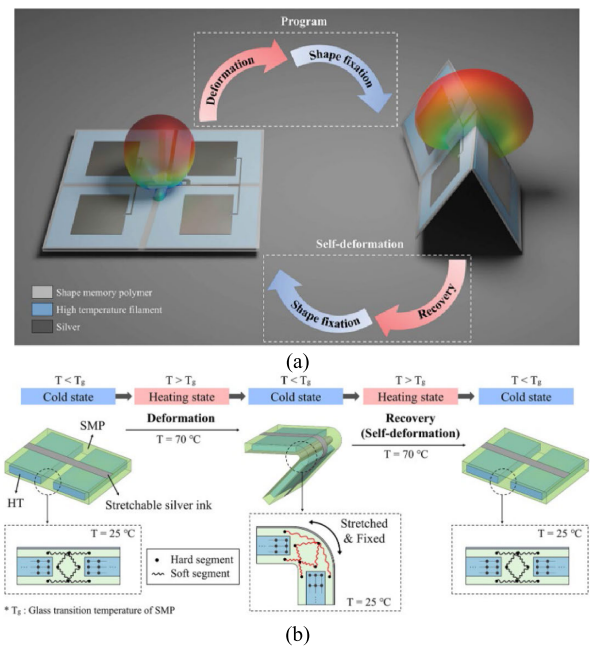
Fig. 50. *(a) Shape morphing of a 4-D-printed multimaterial Miura origami antenna array. (b) Shape deformation process of the proposed antenna [250].*
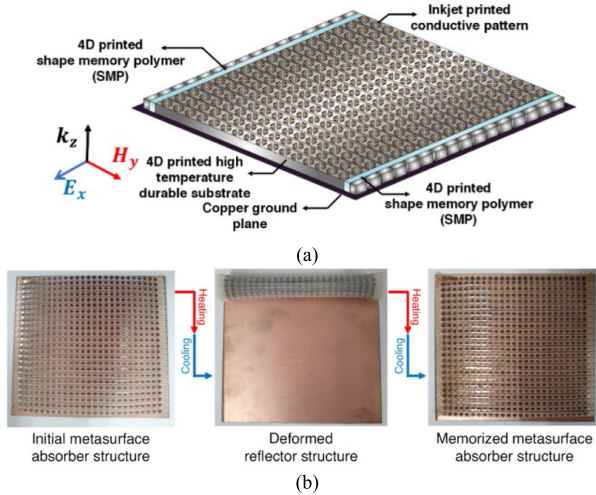
Fig. 51. *Four-dimensional-printed shape memory metasurface absorber. (a) Overall structure. (b) SMP drives the metasurface hinges to switch between an absorber and a reflector [251].*

Fig. 52. *Four-dimensional printing facilitates electronic device packaging. (a) Inkjet-printed patch antennas on unfolded cube surfaces. (b) Folded cube [253]. (c) Foldable monopole array from temporary to permanent state [254].*

Fig. 51 illustrates a metasurface absorber featured with SMP hinges on both sides. Upon heating, the hinges induce the array to curl toward one side, revealing the metallic reflector [251]. As shown in Fig. 51(a), the metasurface includes an inkjet-printed conductive pattern on the top, 4-D-printed high-temperature durable substrate, 4-D-printed SMP hinges, and a metallic plate [251]. The deformation process of the metasurface, enabled by the SMP hinges, is demonstrated in Fig. 51(b). The 4-D-printed SMP hinges can also be utilized to facilitate the design of packaged RF electronic devices, as demonstrated in Fig. 52 [253], [254]. These hinges at the joints of the origami structures can be metallized by direct inkjet printing with CI, which is suitable for energy harvest by converting the captured RF energy into dc with the rectifier circuit [255]. The origami structure encapsulates the rectifier circuit internally through a 4-D-printed SMP, as shown in Fig. 52(b). Fig. 52(c) illustrates another example of 4-D printin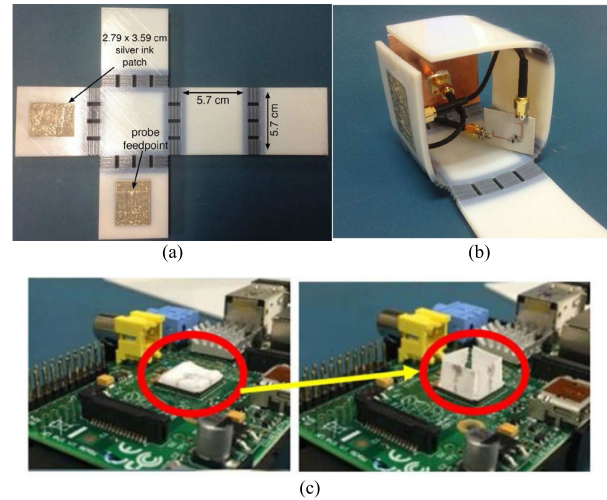g for antenna array packaging, where the SMP enables the antennas to be folded into a 2-D planar structure and then revert their preprogrammed shape upon heating to 60 °C [254]. This highlights the potential of implementing 4-D-printed SMPs in packaging, paving the way for future applications that could integrate with heat sinks, origami metamaterials, and various other reactive and compact structures [255].

Cold programming technology enables each hinge unit to deform independently, allowing for bending at various angles and thus providing limitless possibilities in shape reconfigurability [211]. Adding microchannels in the strips and injecting them with liquid metal (e.g., EGaIn), as shown in Fig. 53, make these strips conductive shape variable components [211], enabling smooth configurations without interrupting the operation of electronic devices. These transformable structures may be used as substrates or structural matrices for fabricating shape-morphing antennas with optimized reconfigurable radiation patterns.

The other primary type of 4-D-printed electronic devices uses SMMs as the principal functional electronic components, leveraging deformation capabilities. Although employing SMAs in 4-D printing is still in its exploratory phase, their distinctive mechanical properties and various driving methods present significant potential for developing reconfigurable chiral metamaterial electronic devices [256]. As demonstrated in Fig. 54, the bending directions of SMA strips can transition among left-handed circularly polarized, right-handed circularly polarized, and nonchiral meta-atom geometries by adjusting the ambient temperatures [257]. It is worth highlighting that this SMA structure can be readily fabricated using 4-D printing technology, resulting in improved controllability and enhanced shape memory capabilities.

The 4-D printing technology facilitates an innovative method for developing stealth and hallucination devices [258]. Fig. 55 illustrates a convertible metasurface capable of switching between EM stealth and hallucination functions, which was manufactured using a 4-D printing process with the aid of FDM technology and liquid metal
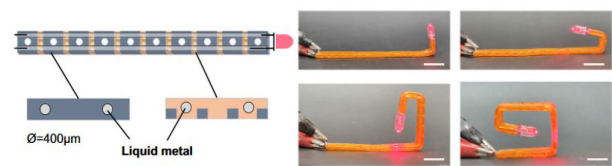
Fig. 53. *Four-dimensional-printed cold-programmed shape deformative electronic device filled with liquid metal [211].*

(a)

(b)
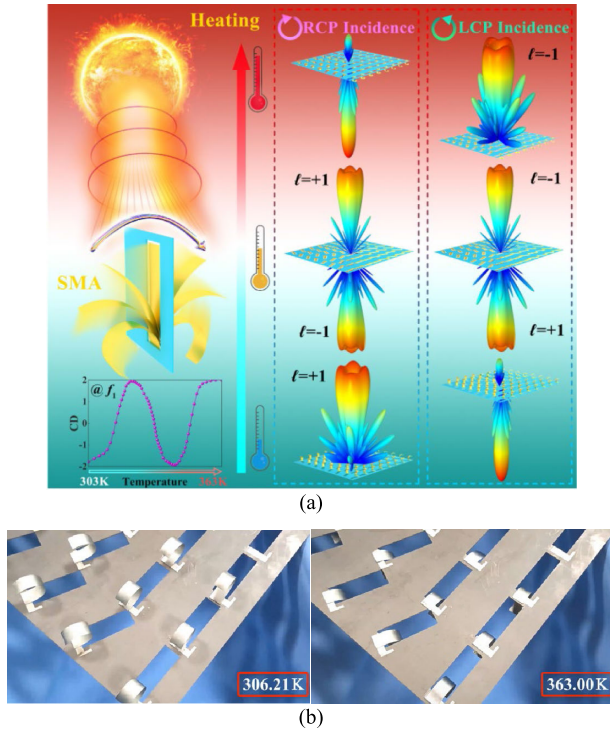
Fig. 54. *Example of thermal responsive chiral metamaterial using SMA. (a) Proposed structure and its EM performance. (b) Array deformation at different stimulating temperatures [257].*

(a)

(b)

Fig. 55. *EM stealth and hallucination convertible metasurface. (a) Operation mode switching when metasurface undergoes deformation under external stimuli. The bottom left image shows the meta-atom geometry, while the bottom right image shows the simulated reflectivity under normal incidence at 6.6-GHz E_y polarization. (b) Fabricated sample in its original and deformed shapes [258].*

injection molding. The flat-structured metasurface can establish a phantom target with a "V" groove feature, while the triangular-structured metasurface can simulate the ground plane and establish a triangular stealth region. This 4-D-printed structure is thermally deformable, enabling dynamic variation in phase distribution.

Fig. 56 shows an FSS of a Miura structure, which can be folded to achieve adjustable frequency and bandwidth, as well as insensitivity to oblique incidence [259], [260]. The substrate was processed using SLA equipment and was made of fl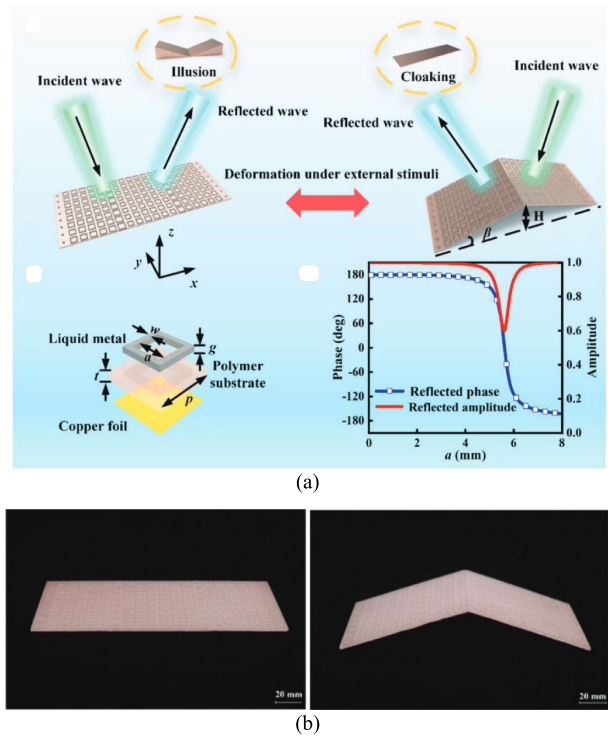exible elastomer photosensitive resin, while the conductive dipoles were printed using SNP ink through an inkjet printer [260]. Before printing, conductive traces were subjected to 90 s of UV treatment to improve the adhesion of SNP ink. Subsequently, a low-temperature gradient sintering process was developed to ensure that the resin substrate was not damaged during SNP ink sintering [259]. Based on a series of empirical tests, six layers of silver printing were selected to compensate for the loss of resolution and 3-D sample tilt [260].

To design flexible electronic devices, SMPs integrated with conductive materials (e.g., SNP ink and carbon nanotubes) serve as viable alternatives to SMAs. As exemplified by the temperature sensor and the connector in Fig. 57, thermal stimulation leads to the closure of the circuits and subsequent illumination of the LEDs [111]. Beyond the basic implementations as a circuit breaker or connector, the SMP-conductor hybrid can act as an EM

wave radiator. Fig. 58 depicts a frequency-memorizing antenna [247]. Its reconfigurability is attained by stretching the director. Fig. 59 illustrates another intelligent antenna whose spiral structure was 4-D-printed with SMP and then treated with copper plating [252]. It efficiently and cost-effectively addresses multiband operation, impedance matching, and pattern synthesis challenges through real-time reprogramming and deformation. First,

(a)   (b)
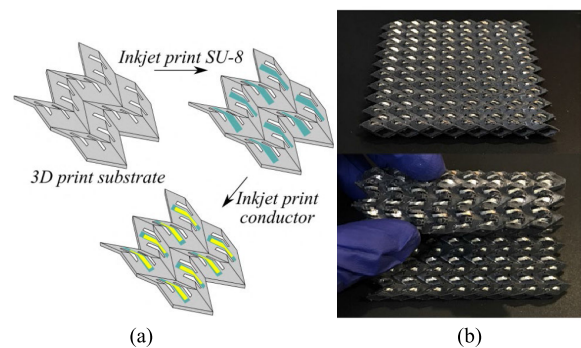
Fig. 56. *Four-dimensional-printed tunable Miura shape FSS. (a) Fabrication process. (b) Fabricated samples [259], [260].*

(a)

(b)
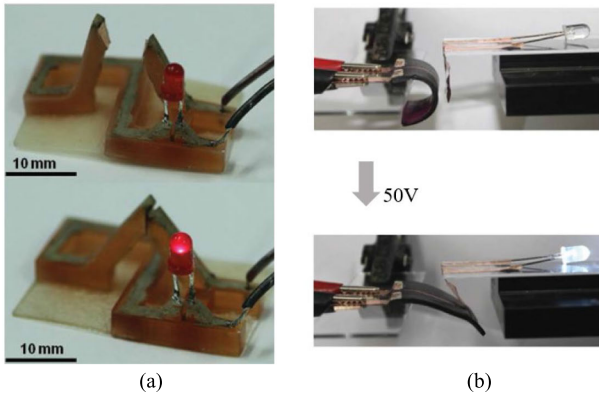
Fig. 57. *Flexible electronic sensor. (a) Temperature sensor in its off-state (top) and on-state (bottom). (b) Connector closes the circuit at a voltage of 50 V [111].*

(a)   (b)

Fig. 59. *Spiral antenna made of 4-D-printed SMP with copper coating. (a) Extended state with a total axial length of 100 mm. (b) Compressed state with a total axial length of 40 mm [252].*

the SMP blend was optimized to enhance its ductility at room temperature. Then, the conductivity of the electroplated copper was experimentally validated by four-point probe tests. Lastly, the RF performance was assessed concerning its deformation behavior. This study suggests that future designs might be preselected and simulated according to specific RF responses. Fig. 60 shows a thermally adaptive spiral inductor designed and manufactured using 4-D-printed SMPs with silver ink coatings [261]. The effectiveness of this spiral inductor is determined by factors such as the number of turns and the inner and outer diameters of the spiral. The engineered inductor is encased within a square grid, serving the dual purpose of grounding and stabilizing the frame. Its characteristics, such as inductance, Q-factor values, resonant frequency, and shape restoration capabilities, are investigated through both numerical and experimental approaches.

Compared with direct heating, the Joule heating method is more convenient, efficient, and controllable in driving, as exhibited in Fig. 61(a) [262]. Conductive materials, such as carbon nanofibers, carbon nanotubes, metal nanoparticles, and graphene, can be doped to SMPs to introduce resistivity without reducing their shape recovery performance [256]. The highly conductive

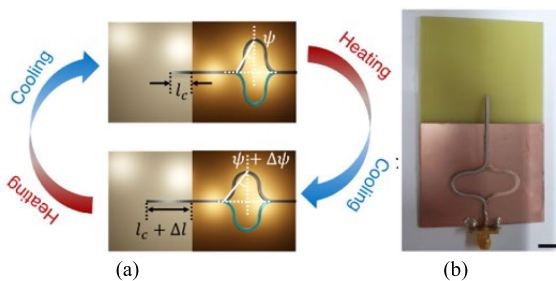nanocomposite material structure has been successfully applied to high-performance electrical equipment, including room-temperature printed conductive components, microstructure fiber sensors, flexible and lightweight supports for EMI shielding, and low-voltage triggered intelligent fixtures [263], as shown in Fig. 61(b). Magnetic materials can be integrated into SMPs to design conical spiral antennas, achieving frequency reconfigurability, as shown in Fig. 61(c) [225]. The simulated and experimental results indicate that the antenna's resonant frequency can be easily tuned, ranging from 2.15 to 3.26 GHz, while the simulated radiation pattern attains similar contours. Due to the shape-locking ability provided by magnetic SMPs, the reconfigured antenna can maintain its new shape without the intervention of external fields, thereby reducing overall energy consumption [225].

(a)

(b)

Fig. 60. *Thermal spiral inductor using 4-D-printed shape memory Kirigami. (a) FDM process to print the proposed SMP-based spiral inductor. (b) Fabricated inductor from various viewpoints [261].*

(a)   (b)

Fig. 58. *Frequency memorizing mmA. (a) Initial and memorized state (top) and programmed state (bottom). (b) Fabricated prototype sample (scale bar is 10 mm) [247].*

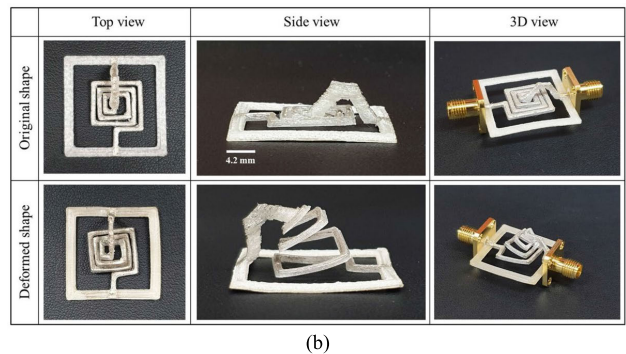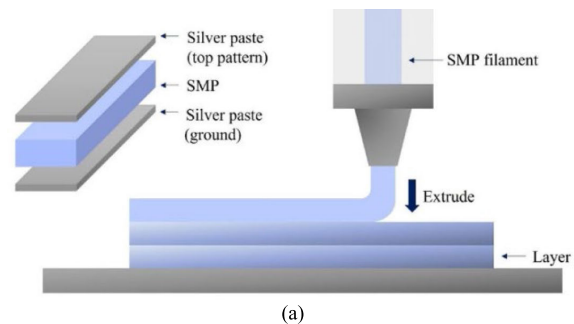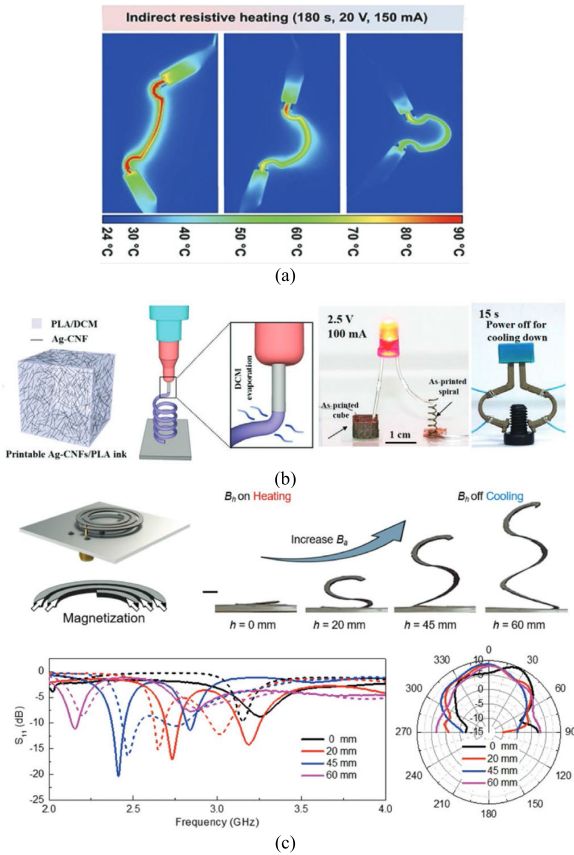**Fig. 61.** *Four-dimensional-printed SMC electronic devices. (a) Joule heating shape recovery process of 4-D printing electronic components [262]. (b) Highly conductive composites and electroactive smart grippers for 4-D printing [263]. (c) Spiral antennas processed with magnetized SMPs [225].*

SMPs are widely used across numerous applications due to their exceptional shape deformation capabilities and diverse driving mechanisms. The 4-D-printed SMPs find extensive applications in fields such as medicine, robotics, and bionics, particularly in scenarios requiring substantial shape variations. However, achieving conductive properties in SMPs typically involves electroplating, incorporating conductive particles, or combining them with liquid metals. In contrast, SMAs possess inherent conductive properties, yet their processes are complex, challenging to control precisely, and have higher material costs. SMAs excel in mechanical and material properties and are primarily employed in the medical field to withstand stress or act as support structures. In electronic devices, SMAs can serve as the core functional component while fulfilling structural functions, enabling concurrent changes in functionality and shape, thereby offering significant potential for further development.

VI. 4-D ORIGAMI AND RECONFIGURABLE PHASED ARRAYS AND REFLECTARRAYS

Origami, the Japanese art of paper folding, has transcended its traditional realm to become a compelling avenue for realizing shape-changing and morphing RF structures and antennas. Compared with the conventional reconfigurable antennas using p-i-n didoes/varactors, origami is nonswitch-based by utilizing morphing origami structures. It introduces deployable mechanisms that are simple yet effective, offering significant advantages when applied to reflectarrays [264]. Additionally, these structures provide unmatched frequency response tunability for FSSs and unprecedented beam-scanning angles and radiation pattern reconfigurability when applied to phased array antenna designs. While the integration of 4-D printing technologies into the development of origami-inspired RF electronics offers significant potential, particularly in creating dynamic, deployable, and reconfigurable RF systems (with reconfigurable frequency, radiation pattern, and polarization), several challenges must be addressed to realize the capabilities of this emerging technology fully. A holistic implementation of a shape-changing, origami-inspired RF structure necessitates the confluence of three interdependent efforts: hardware realization materials (Section VI-A), a method for mechanical control if shape-change is utilized intentionally or a technique for determining the geometrical configuration if an uncontrolled external stimulus affects the shape utilizing reliably foldable hinges (Section VI-B), and if the structure is a phased array antenna, a digital control scheme for 4-D beam-shaping and/or electronic calibration (Section VI-C). Therefore, this section delves into the synergy between AM processes, including 3-D and inkjet printing, the realization of complex morphing RF/mm-wave structures, and fully integrated communication systems and phased arrays.

A. Flexible Materials for 4-D Morphing RF Structures

One of the primary challenges lies in the material limitations of current 4-D printing technologies for RF applications, which not only must exhibit desirable shape-memory characteristics, but also possess the electrical properties required for high-frequency performance. Additionally, the mechanical properties of these materials must be carefully engineered to withstand the stresses associated with repeated folding and unfolding, a key aspect of origami-based designs. For 4-D-printed origami and reconfigurable devices, accurately assessing the electrical characteristics of flexible materials stands as a foundational step, given the potential variations in dielectric properties among materials of the same type from different manufacturers due to fabrication methods and material composition. Traditional flexible devices utilize commercially available flexible substrates like polyethylene terephthalate (PET) and Kapton. Kapton exhibits exceptional resilience to high temperatures and maintains a consistent thermal expansion coefficient across a broad operational temperature range spanning from $-269\,°C$ to $400\,°C$. PET is popular for its transparent and semicrystalline nature. However, a significant drawback of these commercially available materials

is their inability to accommodate complex typologies or facilitate heterogeneous multilayer integration. To address this limitation, 3-D-printed flexible materials emerge as a viable solution for customized designs. Within this context, previous studies investigated different types of 3-D-printed flexible materials from Formlabs 3 (SLA printer) and Ultimaker S3 (FDM printer) through wideband characterization spanning 26–40 GHz [265]. Notably, materials such as Flexible 80A and Elastic 50A from Formlabs exhibit larger dielectric constants and loss tangents, while polypropylene (PP) from Ultimaker showcases an exceptionally low loss tangent of 0.001, making it preferable for mm-wave flexible modules. Another critical challenge involves the potential for plastic deformations during flex-cycling experiments, which can compromise the long-term mechanical and electrical stability of morphing RF structures. This issue is particularly concerning for repeated folding and unfolding cycles. Notably, Hu et al. [266] present a significant advancement in addressing this challenge, demonstrating that flexible 3-D "ramp" interconnects can maintain stable performance after thousands of flexing/unflexing cycles, thereby offering a promising solution for enhancing the durability of these structures in practical applications.

B. Origami-Inspired FSSs and Phased Array Antennas

Reflectarray antennas combine parabolic reflectors' best features and phased array antennas, offering narrow beams and high-gain radiation patterns. Recent research has explored integrating 4-D printing and origami principles to advance reflectarray technology. Pioneering work by Cui et al. [267], [268] showcased a first-of-its-kind fully 3-D-printed mm-wave reflectarray. Using Formlabs FLGR02 Flexible photopolymer, this reflectarray features a novel one-shot deployable Kirigami-inspired flat-foldable dielectric-based unit cell. Formlabs FLGR02, characterized by a dielectric constant of 2.82 and a loss tangent of 0.027 at 29 GHz, offers favorable mechanical properties with a tensile strength of 7.78.5 MPa and 8% elongation. Building on this, subsequent research [269] presents a refined Kirigami-inspired deployable reflectarray utilizing Formlabs Flexible80A, a flexible resin-based photopolymer characterized by a dielectric constant of 2.763 and a loss tangent of 0.042 at 30 GHz, coupled with a Young's modulus of 4.4 MPa. The element design [Fig. 62(a)] showcases a two-stage snapping-like structure inspired by Kirigami principles, allowing for a 66% retraction to save space. The fabricated reflectarrays, depicted in both retracted and folded states [Fig. 62(b)], demonstrate the practical implementation of these concepts. Additionally, the bifocal measurement setup [Fig. 62(c)] illustrates the measured realized gain of approximately 25 dBi at boresight, validating the efficacy of the proposed design approach.

Another category of microwave devices that have greatly benefited from 4-D printing is FSSs. These structures manipulate EM waves by absorption, reflection, or
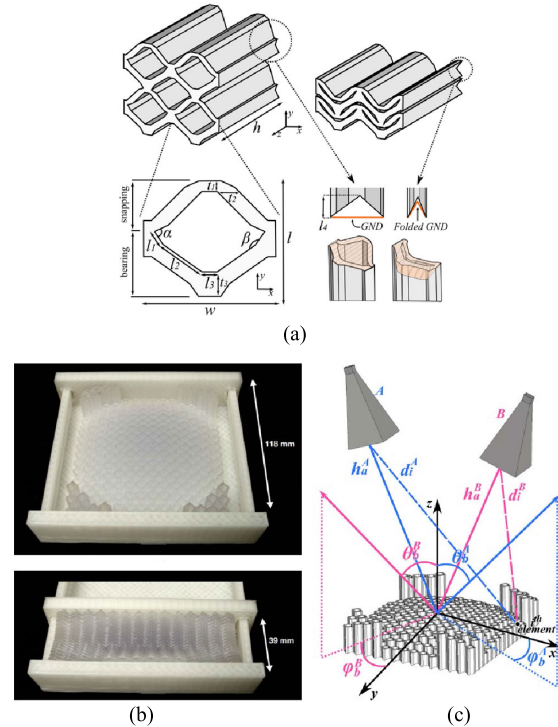
Fig. 62. *Three-dimensional-printed Kirigami-inspired bifocal beam-scanning dielectric reflectarray antenna for one-shot deployability in mm-wave application. (a) Element design showing deployed and folded states. (b) Fabricated 3-D-printed sample. (c) Bifocal beam scanning reflectarray setup [269].*

transmission through periodic metallic array geometries arranged on a dielectric substrate. Shape-changing structures have, in turn, led researchers toward developing continuous-range tunable FSSs. In Fig. 63(a) and (b), a 4-degree-of-freedom (DOF) "eggbox" origami-inspired FSS is presented [270], [271]. The cross-dipole conductors are fully additive inkjet-printed using SNP ink on a 110-μm-thick cellulose paper substrate, characterized at 7.5 GHz with a dielectric constant of 3.4 and a loss tangent of 0.015. Origami principles are then used to manipulate the "eggbox" structure; a centrosymmetric structure that can be folded or rotated along two axes. This demonstration marks a significant advancement compared to previously utilized "Miura-Ori" origami structures, which offer fewer degrees of control. The measurement results [Fig. 63(c) and (d)] demonstrate a wide range of frequency control, with a 25% fractional bandwidth achieved for different eggbox origami bend angles and across vertical and horizontal polarisations.

Actuating an origami FSS was then tackled by Nauroze and Tentzeris [272], [273]. Through an additive design methodology, the authors realize a multilayer FSS with an integrated thermal actuation mechanism featuring unprecedented high mechanical strength. A unit-cell stack is shown in Fig. 64(a), with the three-layer FSS constituting two outer cellulose paper substrates onto which

(a)

(b)

(c)   (d)

Fig. 63. *(a) Three-step additive fabricated process for the fabrication of the eggbox-enabled FSS unit cell. (b) Demonstration of the 4-DOF tuning methodology folding and rotating. (c) Vertical (y-axis) and (d) horizontal (x-axis) polarization simulation and measurement results [270], [271].*

hinge structures, requiring electromechanical codesign strategies.

Addressing these challenges, Al Jamal et al. [274] presented the first origami-inspired phased array operating at 28 GHz with on-structure integrated beamformer ICs and a face-to-face feeding network connecting all four faces of the utilized "eggbox" origami, enabled by "arch" hinge interconnects [Fig. 65(a)]. The "eggbox" origami, foldable along two planes and multifaceted, allows the phased array to achieve 360° beam-steering in the azimuth plane with multibeam patterns. The fabricated prototype [Fig. 65(b)] is additively manufactured using inkjet and SLA 3-D printing, and measurements demonstrate the exploration of radiation pattern reconfigurability through 2-DOF, offering simultaneous electrical beam-steering and mechanical shape-change adaptability, a previously unexplored dimension [Fig. 65(c)–(e)]. Folding the eggbox phased array along the y-axis enables a seamless transition in the radiation pattern, transforming it from four independent beams to a quas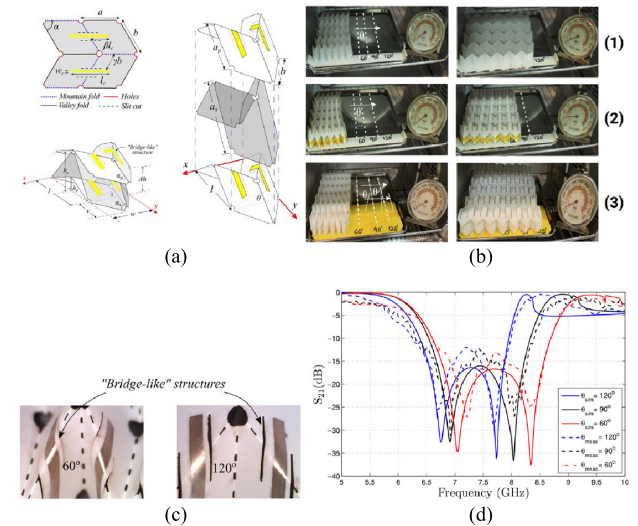i-isotropic pattern and finally to two beams along the y-axis. By folding along the x-axis instead, symmetrical patterns can be achieved. For a given bend angle, the position of the pattern's nulls, beamwidth, and gain can then be independently controlled by providing the right phase conditions to the 16 radiating elements using the beamformer ICs. More generally, highly integrated RF origami-inspired structures necessitate foldable hinge interconnects tailored for RF applications. That is when connecting antennas and RF circuitry across different facets of the origami structure through TLs, it is crucial not only to realize flexible hinge structures and

conductive traces are inkjet-printed and an intermediate heat-sensitive polyester film. This film facilitates the actuation of the Miura Ori structure and maintains optimum interlayer distances as the MiuraFSS structure is folded to preserve the desired frequency response. The fabricated prototype, depicted in Fig. 64(b), is actuated between 60° and 120° with temperatures ranging from 35 °C to 50 °C. Perforations are strategically employed to avoid substrate cracking or breakage, and "bridgelike" slot structures facilitate the inkjet-printed dipoles folding in a smooth, curved fashion along the fold lines, as demonstrated in Fig. 64(c). The measured response of the FSS exhibits excellent agreement with the simulation, as shown in Fig. 64(d).

Thus far, the 4-D origami structures presented have required no active devices, enabling easy scalability by allowing many individual unit cells to be fabricated and then assembled in any desired configuration. However, the realization of an origami-inspired shape-changing and fully integrated *phased array* antenna demands beamformer ICs. Moreover, suppose different antenna elements on different faces of the origami structure are to be connected through a feeding network. This introduces the challenge of realizing metalized conductors over foldable

(a)   (b)

(c)   (d)

Fig. 64. *Thermally actuated origami-inspired Miura FSS. (a) Unit-cell design and multilayer stackup. (b) Thermal actuation of a (1) single-layer polyester film-based FSS, and multilayer sandwiched between two (2) cellulose and (3) polyester-based single-layer FSS structures. (c) Bridge-like structures used for different folding angles. (d) Frequency response for different folding angles [272], [273].*
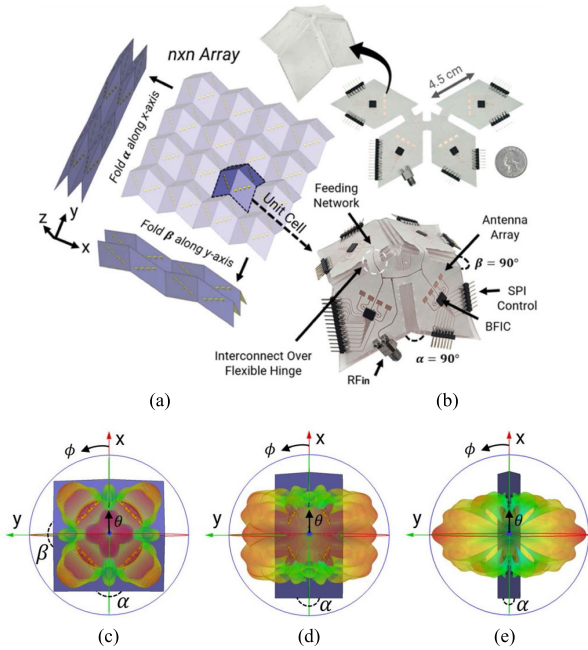
Fig. 65. *Four-dimensional origami-inspired, radio frequency integrated circuit (RFIC)-based, and fully integrated phased array incorporating foldable "arch" interconnects. (a) n × n array of an "eggbox" origami. (b) Fabrication process, and fabricated unit cell on a flexible 3-D-printed substrate. (c)–(e) Radiation pattern reconfigurability for different folding angles [274].*

maintain electrical continuity but also to ensure stable RF performance, particularly with respect to IL. The mechanical distortion these lines experience during shape changes must be carefully managed to maintain consistent RF characteristics. As aforementioned, Al Jamal et al. [274] present the first additively manufactured mm-wave hinge interconnect with an "arch" topology that exhibits near-constant IL of 0.02 dB/mm across various folding angles and cycles at 28 GHz. Other foldable interconnects at lower frequency bands include liquid metal hinges for a 2.4-GHz origami-inspired antenna [275] and a PCB-milled surrogate hinge structure for a 2.45-GHz antenna array [276]. Any instability in electrical performance due to folding should be either mitigated or intentionally leveraged to introduce controllable frequency and/or pattern reconfigurability. It is also to be noted that mm-wave hinge interconnects are more challenging to realize not only due to the pronounced losses at higher frequencies but also due to the smaller scale of the antenna radiators.

C. 4-D Phased Array Calibration

The emergence of flexible phased array systems has drawn considerable attention due to their adaptable beam steerability and deployable structures capable of supporting diverse platforms on virtually any conformal surface. A tile-based phased array, manufactured via additive techniques, presents a lightweight, flexible, and highly scalable solution, accompanied by reduced costs and fabrication

durations. However, the primary challenge faced by such conformal phased array systems lies in maintaining optimal performance amidst varying deformations, necessitating calibration of both the amplitude and phase distribution of antenna elements. In response to this challenge, novel approaches have been proposed to achieve shape calibration and phase correction of the conformal phased array systems. Addressing these challenges requires interdisciplinary collaboration between material scientists, engineers, and designers. Advances in multimaterial 4-D printing, the development of novel SMMs with tailored electrical properties, and improved fabrication techniques are all critical areas of research. Additionally, integrating simulation tools that can accurately predict the behavior of shape-changing 4-D-printed origami structures under various conditions will be essential for optimizing their design and performance in RF applications.

He and Tentzeris [277] employed an additively manufactured in-package flex sensor to enable precise bending prediction and self-calibration of flexible phased arrays. The dimensions of the inkjet-printed proof-of-concept flex sensor are depicted in Fig. 66. To cover both North-South (NS) and East-West (EW) bending axes, the sensor is printed in a cross pattern, with additional dimensions possible for sensing local deformations in larger arrays. For accurate strain resistance measurement, the change in resistance is incorporated into a Wheatstone-bridge configuration, with the output voltage of the Wheatstone bridge being the difference in voltage between the unknown strain resistance voltage divider and a known voltage divider. This difference is then amplified using an instrumentation amplifier and read using a microcontroller unit (MCU). A systematic test structure was devised to characterize the flexing under test swiftly and reliably, with data collected at eight sequential notches corresponding to bend radii of roughly 155, 80, 60, 50, 45, 40, 37.5, and 34.5 mm, encompassing 16 distinct bend classes. Using discriminant analysis (LDA), classification was performed based on feature vectors representing the percent change
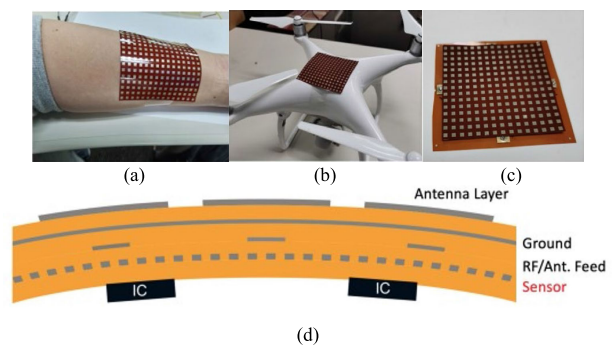
Fig. 66. *Demonstration of applications of flexible phased array antenna that includes (a) wearable technologies, (b) conformal structures, and (c) inkjet-printed patch array with (d) inkjet-printed flex sensor.*

(a)

(b)   (c)
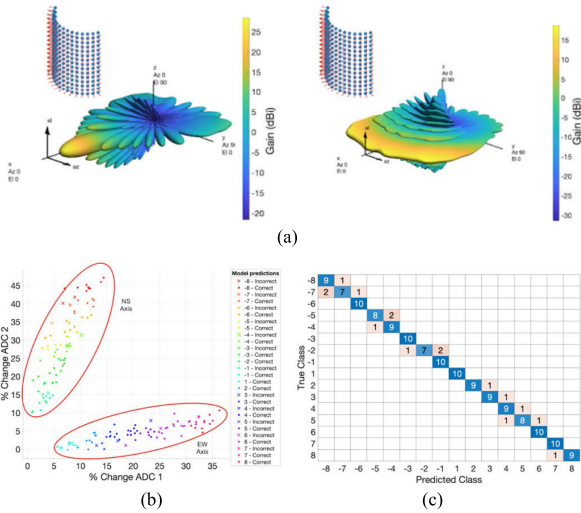
Fig. 67. *(a) Calibrated phased array using sensor data (right) versus uncalibrated equal phasing (left). (b) 160 data points collected, with false predictions marked as "x." The two groups shown are the two NS and EW bend axis measurements.*
(c) Confusion matrix of the LDA model, which demonstrates that this is a good model as most of the predictions lie on the diagonal.

Fig. 68. *Demonstration of the proposed camera-enabled calibration method.*

in voltage readings for both NS and EW axes. Fivefold cross-validation was employed to assess the model's accuracy, which is crucial for correct bend prediction to mitigate significant gain errors, as demonstrated in Fig. 67(a). The confusion matrix depicted in Fig. 67(c) highlights the excellent correlation between true class and predicted class, with minimal misclassifications. This approach was evaluated using a 15×15 conformal array setup employing 29-GHz patch antenna elements spaced $\lambda/2$ apart, demonstrating an average gain error cost of 1.04 dB per misclassification, with an overall average gain error of 0.071 dB across the entire dataset, showcasing substantial improvement compared to equal phase feeding configurations. Demonstrating notable efficacy, the sensor achieved an accuracy rate of 90% in predicting bend radii in both directions across the plane of a 29-GHz 15×15 element phased array model. While this method showcased effectiveness in cylindrical phased arrays, they encountered constraints when applied to scenarios involving irregular surfaces or nonuniform spacings, consequently limiting resolution.

More recently, a new approach was proposed to utilize smartphones equipped with integrated 3-D depth cameras and LiDAR sensors (Fig. 68) alongside an innovative computer vision algorithm designed to detect bend angles between neighboring subarray tiles to achieve the capability of on-the-fly adaptive shape calibration and phase correction [278]. A 2×1 tiled phased array was utilized as a test vehicle to demonstrate the proposed calibration approach, similar to the one presented in [279]. The beamforming integrated circuit (BFIC) (Anokiwave AWS-0102) uses serial peripheral interface (SPI) communication to
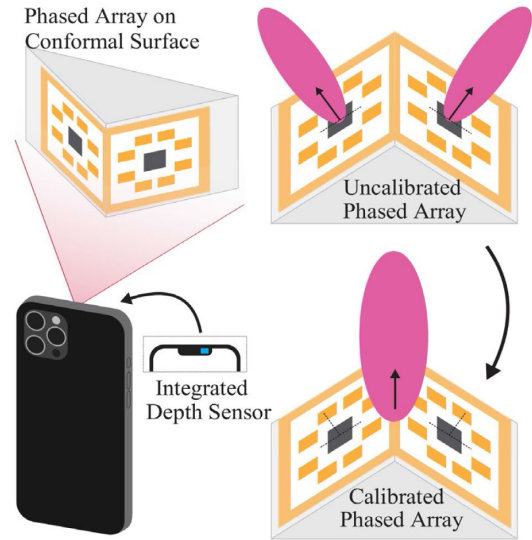
control the amplitude and phase of each antenna element. A microstrip-to-microstrip transition was utilized to attach individual tiles to the flexible tiling layer [279]. When the 2×1 tiled phased array is bent at an angle θ, each array tile has the main lobe direction off from boresight by the angle θ, leading to reduced realized gain and lower radiation efficiency. By calibrating the phased array, a phase shift will be applied to each antenna element using SPI control from BFIC, to steer the main lobe of each array tile by the angle θ to correct the radiation pattern and refocus the main beam to boresight for optimal performance.

The initial stage of the algorithm involves processing raw data obtained from the smartphone camera to detect the normal vector of the sample holder for the bent-tiled phased array. The standard Hough transform (SHT) is then employed to extract information from the detected
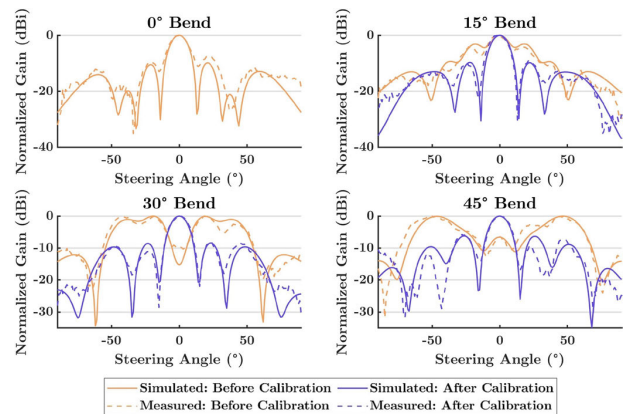
Fig. 69. *Comparison of simulated and measured radiation patterns of phased array calibration results in bend configurations of 0°, 15°, 30°, and 45°.*

lines, determining the line equations for calibration. Subsequently, the algorithm computes the Z-axis rotation angle by refining the detection region to focus solely on the phased array and applying a second SHT edge detection for the tiling layer. With the phased array's edge and previously computed normal vector, the XY plane and Z-axis are rotated using a 3-D rotation matrix. After calibration, data points along the phased array's edge line are sampled, and a linear curve fitting algorithm is applied to determine the bend angle of the phased array, which is calculated as the average of the arc tangent of the slopes.

To assess the algorithm's validity, the phased array was positioned on various 3-D-printed angular blocks, spanning angles from $5°$ to $85°$. The results indicate the algorithm's capability to produce accurate outcomes, with angular errors below $0.8°$ for each bent sample. Fig. 69 displays the measured radiation patterns for each configuration, indicating that the calibrated phased array successfully achieves impressive beamforming patterns, particularly noticeable at larger bend angles. At a $45°$ bend angle, the array consolidates two beams from each tile into a single beam, correcting the main lobe direction from $\pm 47°$ to $0°$. The calibrated phased array demonstrates a minimum 7-dB gain increase and over 5-dB reduction in sidelobe level across different bend angles.

VII. CONCLUSION

This article provides an overview of the latest advancements in AME encompassing conductive and dielectric multimaterials, alongside the exploration of 4-D printing and origami shape-memory electronic devices by delving five critical AME processing techniques: FDM [90], [139], AJP [140], PI [142], [143], TIP [141], [280], [281], [282], [283], and DIW [144], [145], [284], [285]. A detailed design guideline and illustrative examples utilizing various 3-D printing technologies are outlined. The emerging concept of 4-D printing is also introduced and juxtaposed with traditional 3-D printing methods, with discussions on different SMMs and associated printing techniques. The 4-D printing allows the use of SMMs in intelligent electronics, adding the dimension of time to the manufacturing or training

process, which sets it apart from conventional 3-D-printed electronics. This article showcases design examples for future wireless communications and sensing applications, offering insights into shape-memory training and stimuli methods. The 4-D origami and reconfigurable phased arrays and reflectarrays are explored by highlighting shape-morphing RF structures for electronic function reconfigurations such as radiation patterns, frequencies, polarisations, and beam-steering. These advancements hold promise for applications in smart phones, small satellites, and wearable electronic devices. This comprehensive review aims to equip electronic engineers with an in-depth understanding of cutting-edge 3-D/4-D printing technologies for intelligent reconfigurable devices, anticipating their significance in the coming decade. The step-by-step guidelines provided serve as valuable resources, aiding engineers in AME throughout the entire process, from conceptual design to fabrication and implementation.

Advanced AM technologies, especially when integrated with SMMs, unlock significant potential for designing and fabricating novel, high-performance, and reconfigurable electronic devices. However, further technological advancements and developments are not unnecessary in achieving widespread real-world applications. First, the range of accessible SMMs for AM is not sufficiently diversified, and material scientists currently aim for optimization of the mechanical and electrical properties, including the types, speed, and accuracy of stimulus responses, the antioxidation and durability of SMAs, and the strength of SMPs. In addition, the techniques for printing SMMs with high-resolution, time-efficiency, and cost-effectiveness have not been well-developed and widely adopted in the industries. The yield rates for multimaterial and highly integrated 4-D printing remain low, and specific printing platforms are often restricted to certain categories of printing materials. Furthermore, there is a lack of a systematic design methodology that precisely details the characteristics of different SMMs, as well as comprehensive CAD software that specifically addresses the nuances of heat treatment, mechanical loading, and memory training, with a focus on achieving bidirectional SMEs. ∎

REFERENCES

[1] *Additive Manufacturing in Industry 4.0*. Accessed: Jan. 10, 2024. [Online]. Available: https://www.esa-automation.com/en/additive-manufacturing-in-industry-4-0/

[2] *Reed Bus. Information*, New Scientist, London, U.K., 1974.

[3] H. Kodama, "Automatic method for fabricating a three-dimensional plastic model with photo-hardening polymer," *Rev. Sci. Instrum.*, vol. 52, no. 11, pp. 1770–1773, Nov. 1981.

[4] *Wikipedia*. [Online]. Available: https://en.wikipedia.org/wiki/Stereolithography

[5] D. Freedman, "Layer-by-layer: The evolution of 3-D printing - IEEE spectrum." Accessed: Jan. 10, 2024. [Online]. Available: https://spectrum.ieee.org/layerbylayer-the-evolution-of-3d-printing

[6] S. Crump, J. Comb, W. Priedeman Jr., and R. Zinniel, "Process of support removal for fused deposition modeling," U.S. Patent 5 503 785, Apr. 2, 1996.

[7] N. Charoo et al., "Selective laser sintering 3D printing—An overview of the technology and pharmaceutical applications," *Drug Dev. Ind. Pharm.*, vol. 46, no. 6, pp. 869–877, Jun. 2020.

[8] J. Beaman and C. Deckard, "Selective laser sintering with assisted powder handling," U.S. Patent 4 816 938, Jul. 3, 1990.

[9] K. G. Cooper, "Rapid prototyping technology: Selection and application," in *Mechanical Engineering*, no. 133. New York, NY, USA: Marcel Dekker, 2001.

[10] F. Ribeiro, "3D printing with metals," *Comput. Control Eng. J.*, vol. 9, no. 1, pp. 31–38, Feb. 1998.

[11] Y. Jiang et al., "Recent advances in 3D printed sensors: Materials, design, and manufacturing," *Adv. Mater. Technol.*, vol. 8, no. 2, 2023, Art. no. 2200492.

[12] Engineering.com. *Voxel8 Continues Multi-Material 3D Printing Revolution*. Accessed: Jan. 10, 2024. [Online]. Available: https://www.engineering.com/story/voxel8-continues-the-multi-material-3d-printing-revolution

[13] *Additively Manufactured Electronics Technology*, IPC International, Bannockburn, IL, USA, Oct. 2023.

[14] T. Prater, N. Werkheiser, and F. Ledbetter, "An overview of NASA's in-space manufacturing project," in *Future In-Space Operations (FISO) Working Group Seminar Series*, no. M17-6341.

NASA, 2017.

[15] C. Guo et al., "A 3-D printed E-plane waveguide magic-T using air-filled coax-to-waveguide transitions," *IEEE Trans. Microw. Theory Techn.*, vol. 67, no. 12, pp. 4984–4994, Dec. 2019.

[16] T. Skaik et al., "Evaluation of 3-D printed monolithic G-band waveguide components," *IEEE Trans. Compon., Packag., Manuf. Technol.*, vol. 13, no. 2, pp. 240–248, Feb. 2023.

[17] B. Yao et al., "Dual-band bandpass filter with high selectivity based on 3D printable groove gap waveguide," *IET Microw., Antennas Propag.*, vol. 17, no. 10, pp. 827–831, Aug. 2023.

[18] M. Dionigi, C. Tomassoni, G. Venanzoni, and R. Sorrentino, "Simple high-performance metal-plating procedure for stereolithographically 3-D-printed waveguide components," *IEEE Microw. Wireless Compon. Lett.*, vol. 27, no. 11, pp. 953–955, Nov. 2017.

[19] B. Zhang, Y.-X. Guo, H. Zirath, and Y. P. Zhang, "Investigation on 3-D-printing technologies for millimeter- wave and terahertz applications," *Proc. IEEE*, vol. 105, no. 4, pp. 723–736, Apr. 2017.

[20] B. Zhang and H. Zirath, "A metallic 3-D printed e-band radio front end," *IEEE Microw. Wireless Compon. Lett.*, vol. 26, no. 5, pp. 331–333, May 2016.

[21] B. Zhang and H. Zirath, "A 3D printed metallic radio front end for E-band applications," *IEEE Microw. Wireless Compon. Lett.*, vol. 26, no. 5, pp. 331–333, May 2016.

[22] M. Palandoken, C. Murat, A. Kaya, and B. Zhang, "A novel 3-D printed microwave probe for ISM band ablation systems of breast cancer treatment applications," *IEEE Trans. Microw. Theory Techn.*, vol. 70, no. 3, pp. 1943–1953, Mar. 2022.

[23] S. Verploegh, M. Coffey, E. Grossman, and Z. Popovic, "Properties of 50–110-GHz waveguide components fabricated by metal additive manufacturing," *IEEE Trans. Microw. Theory Techn.*, vol. 65, no. 12, pp. 5144–5153, Dec. 2017.

[24] L. Zhu, I. W. Rossuck, R. Payapulli, S.-H. Shin, and S. Lucyszyn, "3-D printed W-band waveguide twist with integrated filtering," *IEEE Microw. Wireless Technol. Lett.*, vol. 33, no. 6, pp. 659–662, Jun. 2023.

[25] J. Rico-Fernández, F. V. Vidarsson, M. Arrebola, N. J. G. Fonseca, and O. Quevedo-Teruel, "Compact and lightweight additive manufactured parallel-plate waveguide half-luneburg geodesic lens multiple-beam antenna in the Ka-band," *IEEE Antennas Wireless Propag. Lett.*, vol. 22, pp. 684–688, 2023.

[26] Z. Chen et al., "Circular polarized 3-D-printed dielectric loaded antenna using inset waveguide-to-dielectric transition for 5G millimeter-wave application," *IEEE Antennas Wireless Propag. Lett.*, vol. 19, pp. 1929–1932, 2020.

[27] G.-L. Huang, C.-Z. Han, W. Xu, T. Yuan, and X. Zhang, "A compact 16-way high-power combiner implemented via 3-D metal printing technique for advanced radio-frequency electronics system applications," *IEEE Trans. Ind. Electron.*, vol. 66, no. 6, pp. 4767–4776, Jun. 2019.

[28] G.-L. Huang, S.-G. Zhou, and T. Yuan, "Design of a compact wideband feed cluster with dual-polarized sum- and difference-patterns implemented via 3-D metal printing," *IEEE Trans. Ind. Electron.*, vol. 65, no. 9, pp. 7353–7362, Sep. 2018.

[29] H. Yang et al., "A D-band waveguide diplexer based on copper additive manufacturing," *IEEE Trans. Compon., Packag., Manuf. Technol.*, vol. 13, no. 8, pp. 1271–1277, Aug. 2023.

[30] B. Zhang and H. Zirath, "Metallic 3-D printed rectangular waveguides for millimeter-wave applications," *IEEE Trans. Compon., Packag., Manuf. Technol.*, vol. 6, no. 5, pp. 796–804, May 2016.

[31] L. Qian, R. Martinez, M. Salek, T. Skaik, M. Attallah, and Y. Wang, "Compact monolithic 3D-printed wideband filters using pole-generating

resonant irises," *IEEE J. Microw.*, vol. 3, no. 3, pp. 1028–1039, Jul. 2023.

[32] A. Mostaani, Y. Wang, L. Qian, A. E.-M.-A. Mohamed, M. M. Attallah, and T. Skaik, "Compact self-supportive filters suitable for additive manufacturing," *IEEE Trans. Compon., Packag., Manuf. Technol.*, vol. 13, no. 12, pp. 1966–1972, Dec. 2023.

[33] X. Wen et al., "WR-3.4 band waveguide and bandpass filters using copper additive manufacturing," *IEEE Trans. Microw. Theory Techn.*, vol. 71, no. 3, pp. 1190–1200, Mar. 2023.

[34] O. A. Peverini et al., "Integration of an H-plane bend, a twist, and a filter in Ku/K-band through additive manufacturing," *IEEE Trans. Microw. Theory Techn.*, vol. 66, no. 5, pp. 2210–2219, May 2018.

[35] Y. Chen et al., "3-D printed dual-band filter based on spherical dual-mode cavity," *IEEE Microw. Wireless Compon. Lett.*, vol. 31, no. 9, pp. 1047–1050, Sep. 2021.

[36] G. Zhang et al., "3-D printed filtering rat-race couplers using hemispherical cavity resonator," *IEEE Trans. Microw. Theory Techn.*, vol. 71, no. 11, pp. 4922–4932, Nov. 2023.

[37] C. Guo, X. Shang, J. Li, F. Zhang, M. J. Lancaster, and J. Xu, "A lightweight 3-D printed X-band bandpass filter based on spherical dual-mode resonators," *IEEE Microw. Wireless Compon. Lett.*, vol. 26, no. 8, pp. 568–570, Aug. 2016.

[38] E. López-Oliver et al., "3-D-printed compact bandpass filters based on conical posts," *IEEE Trans. Microw. Theory Techn.*, vol. 69, no. 1, pp. 616–628, Jan. 2021.

[39] G. Venanzoni, C. Tomassoni, M. Dionigi, M. Mongiardo, and R. Sorrentino, "Design and fabrication of 3-D printed inline coaxial filters with improved stopband," *IEEE Trans. Microw. Theory Techn.*, vol. 68, no. 7, pp. 2633–2643, Jul. 2020.

[40] G. Venanzoni, M. Dionigi, C. Tomassoni, and R. Sorrentino, "3-D-printed quasi-elliptical evanescent mode filter using mixed electromagnetic coupling," *IEEE Microw. Wireless Compon. Lett.*, vol. 28, no. 6, pp. 497–499, Jun. 2018.

[41] X. Yang et al., "Design of dual-band filtering antenna based on 3-D printed half-mode gap waveguide quadruple-mode resonator," *IEEE Antennas Wireless Propag. Lett.*, vol. 23, pp. 468–472, 2024.

[42] B. Zhang, R. Li, L. Wu, H. Sun, and Y. Guo, "A highly integrated 3-D printed metallic K-band passive front end as the unit cell in a large array for satellite communication," *IEEE Antennas Wireless Propag. Lett.*, vol. 17, no. 11, pp. 2046–2050, Nov. 2018.

[43] B. Zhang et al., "A metallic 3-D printed airborne high-power handling magneto-electric dipole array with cooling channels," *IEEE Trans. Antennas Propag.*, vol. 67, no. 12, pp. 7368–7378, Dec. 2019.

[44] B. Zhang et al., "A K-band 3-D printed focal-shifted two-dimensional beam-scanning lens antenna with nonuniform feed," *IEEE Antennas Wireless Propag. Lett.*, vol. 18, pp. 2721–2725, 2019.

[45] Q. Chen, F. Cui, and B. Zhang, "A 3-D printed ultrawideband magnetoelectric dipole antenna with ridged waveguide aperture-coupled feeding," *IEEE Antennas Wireless Propag. Lett.*, vol. 22, pp. 814–818, 2023.

[46] Z. Zhu, Y. Yang, D. Mcgloin, S. Liao, and Q. Xue, "3-D printed all-dielectric dual-band broadband reflectarray with a large frequency ratio," *IEEE Trans. Antennas Propag.*, vol. 69, no. 10, pp. 7035–7040, Oct. 2021.

[47] J. Zhu, Y. Yang, S. Liao, and Q. Xue, "Additively manufactured metal-only waveguide-based millimeter-wave broadband achromatic reflectarrays," *IEEE Trans. Antennas Propag.*, vol. 71, no. 7, pp. 6185–6190, Jul. 2023.

[48] J. Zhu, S. Liao, and Q. Xue, "3-D printed millimeter-wave metal-only dual-band circularly polarized reflectarray," *IEEE Trans. Antennas Propag.*, vol. 70, no. 10, pp. 9357–9364,

Oct. 2022.

[49] J. H. Barton, C. R. Garcia, E. A. Berry, R. Salas, and R. C. Rumpf, "3-D printed all-dielectric frequency selective surface with large bandwidth and field of view," *IEEE Trans. Antennas Propag.*, vol. 63, no. 3, pp. 1032–1039, Mar. 2015.

[50] G.-B. Wu, Y.-S. Zeng, K. F. Chan, B.-J. Chen, S.-W. Qu, and C. H. Chan, "High-gain filtering reflectarray antenna for millimeter-wave applications," *IEEE Trans. Antennas Propag.*, vol. 68, no. 2, pp. 805–812, Feb. 2020.

[51] G.-L. Huang, S.-G. Zhou, and T.-H. Chio, "Highly-efficient self-compact monopole antenna system with integrated comparator network for RF industrial applications," *IEEE Trans. Ind. Electron.*, vol. 64, no. 1, pp. 674–681, Jan. 2017.

[52] C. Gu et al., "A D-band 3D-printed antenna," *IEEE Trans. THz Sci. Technol.*, vol. 10, no. 5, pp. 433–442, Sep. 2020.

[53] S. Wang et al., "Radar cross-section reduction of helical antenna by replacing metal with 3-D printed zirconia ceramic," *IEEE Antennas Wireless Propag. Lett.*, vol. 19, pp. 350–354, 2020.

[54] R. Colella, A. Michel, and L. Catarinucci, "Compact 3-D-printed circularly polarized antenna for handheld UHF RFID readers," *IEEE Antennas Wireless Propag. Lett.*, vol. 17, pp. 2021–2025, 2018.

[55] X. Yu et al., "3-D printed parts for a multilayer phased array antenna system," *IEEE Antennas Wireless Propag. Lett.*, vol. 17, pp. 2150–2154, 2018.

[56] S. Moscato et al., "Infill-dependent 3-D-printed material based on NinjaFlex filament for antenna applications," *IEEE Antennas Wireless Propag. Lett.*, vol. 15, pp. 1506–1509, 2016.

[57] B. S. Cook and A. Shamim, "Inkjet printing of novel wideband and high gain antennas on low-cost paper substrate," *IEEE Trans. Antennas Propag.*, vol. 60, no. 9, pp. 4148–4156, Sep. 2012.

[58] S. Kim, Y. Ren, H. Lee, A. Rida, S. Nikolaou, and M. M. Tentzeris, "Monopole antenna with inkjet-printed EBG array on paper substrate for wearable applications," *IEEE Antennas Wireless Propag. Lett.*, vol. 11, pp. 663–666, 2012.

[59] A. Chauraya et al., "Inkjet printed dipole antennas on textiles for wearable communications," *IET Microw., Antennas Propag.*, vol. 7, no. 9, pp. 760–767, Jun. 2013.

[60] M. D. Wu et al., "Design and measurement of a 220 GHz wideband 3-D printed dielectric reflectarray," *IEEE Antennas Wireless Propag. Lett.*, vol. 17, no. 11, pp. 2094–2098, Nov. 2018.

[61] X. Liu et al., "Ultrabroadband all-dielectric transmitarray designing based on genetic algorithm optimization and 3-D print technology," *IEEE Trans. Antennas Propag.*, vol. 69, no. 4, pp. 2003–2012, Apr. 2021.

[62] A. Massaccesi et al., "3D-printable dielectric transmitarray with enhanced bandwidth at millimeter-waves," *IEEE Access*, vol. 6, pp. 46407–46418, Aug. 2018.

[63] B. Zhang et al., "Dielectric and metallic jointly 3D-printed mmWave hyperbolic lens antenna," *IET Microw., Antennas Propag.*, vol. 13, no. 11, pp. 1934–1939, Sep. 2019.

[64] D. Zhou, X. Huang, and Z. Du, "Analysis and design of multilayered broadband radar absorbing metamaterial using the 3-D printing technology-based method," *IEEE Antennas Wireless Propag. Lett.*, vol. 16, pp. 133–136, 2017.

[65] E. Dogan, A. Bhusal, B. Cecen, and A. K. Miri, "3D printing metamaterials towards tissue engineering," *Appl. Mater. Today*, vol. 20, Sep. 2020, Art. no. 100752.

[66] C. Casarini, V. Romero-Garcia, J.-P. Groby, B. Tiller, J. F. C. Windmill, and J. C. Jackson, "Fabrication and characterization of 3D printed thin plates for acoustic metamaterials applications," *IEEE Sensors J.*, vol. 19, no. 22, pp. 10365–10372, Nov. 2019.

[67] S. Ghosh and S. Lim, "Perforated lightweight broadband metamaterial absorber based on 3-D printed honeycomb," *IEEE Antennas Wireless Propag. Lett.*, vol. 17, no. 12, pp. 2379–2383, Dec. 2018.

[68] C. Casarini, B. Tiller, C. Mineo, C. N. Macleod, J. F. C. Windmill, and J. C. Jackson, "Enhancing the sound absorption of small-scale 3-D printed acoustic metamaterials based on Helmholtz resonators," *IEEE Sensors J.*, vol. 18, no. 19, pp. 7949–7955, Oct. 2018.

[69] C. R. Garcia et al., "3D printing of anisotropic metamaterials," *Prog. Electromagn. Res. Lett.*, vol. 34, pp. 75–82, 2012.

[70] B. Nie, H. Lu, T. Skaik, Y. Liu, and Y. Wang, "A 3D-printed subterahertz metallic surface-wave Luneburg lens multibeam antenna," *IEEE Trans. THz Sci. Technol.*, vol. 13, no. 3, pp. 297–301, May 2023.

[71] J. Zhu, Y. Yang, D. McGloin, S. Liao, and Q. Xue, "Sub-terahertz 3-D printed all-dielectric low-cost low-profile lens-integrated polarization beam splitter," *IEEE Trans. THz Sci. Technol.*, vol. 11, no. 4, pp. 433–442, Jul. 2021.

[72] F. Zhou, W. Cao, B. Dong, T. Reissman, W. Zhang, and C. Sun, "Additive manufacturing of a 3D terahertz gradient-refractive index lens," *Adv. Opt. Mater.*, vol. 4, no. 7, pp. 1034–1040, Jul. 2016.

[73] X. He, Y. Yang, L. Deng, S. Li, and B. Feng, "3D printed sub-terahertz all-dielectric lens for arbitrary manipulation of quasi-nondiffractive orbital angular momentum waves," *ACS Appl. Mater. Interfaces*, vol. 13, no. 17, pp. 20770–20778, May 2021.

[74] G.-B. Wu, K. F. Chan, and C. H. Chan, "3-D printed terahertz lens to generate higher order Bessel beams carrying OAM," *IEEE Trans. Antennas Propag.*, vol. 69, no. 6, pp. 3399–3408, Jun. 2021.

[75] J. Zhu et al., "3-D printed planar dielectric linear-to-circular polarization conversion and beam-shaping lenses using coding polarizer," *IEEE Trans. Antennas Propag.*, vol. 68, no. 6, pp. 4332–4343, Jun. 2020.

[76] H. Yi, S. W. Qu, K. B. Ng, C. H. Chan, and X. Bai, "3-D printed millimeter-wave and terahertz lenses with fixed and frequency scanned beam," *IEEE Trans. Antennas Propag.*, vol. 64, no. 2, pp. 442–449, Feb. 2016.

[77] J. C. Zhang et al., "A 6G meta-device for 3D varifocal," *Sci. Adv.*, vol. 9, no. 4, Jan. 2023, Art. no. eadf8478.

[78] Y.-X. Xie, G.-B. Wu, W.-Q. Deng, S.-Y. Zhu, and C. H. Chan, "A 3-D printed ultra-wideband achromatic metalens antenna," *IEEE Open J. Antennas Propag.*, vol. 4, pp. 713–723, 2023.

[79] G. B. Wu, K. F. Chan, K. M. Shum, and C. H. Chan, "Millimeter-wave and terahertz OAM discrete-lens antennas for 5G and beyond," *IEEE Commun. Mag.*, vol. 60, no. 1, pp. 34–39, Jan. 2022.

[80] G.-B. Wu, Y.-S. Zeng, K. F. Chan, S.-W. Qu, J. Shaw, and C. H. Chan, "3-D printed 3-D near-field focus-scanning lens for terahertz applications," *IEEE Trans. Antennas Propag.*, vol. 70, no. 11, pp. 10007–10016, Nov. 2022.

[81] G. B. Wu, K. F. Chan, S. W. Qu, K. F. Tong, and C. H. Chan, "Orbital angular momentum (OAM) mode-reconfigurable discrete dielectric lens operating at 300 GHz," *IEEE Trans. THz Sci. Technol.*, vol. 10, no. 5, pp. 480–489, Sep. 2020.

[82] G.-B. Wu, K. F. Chan, S.-W. Qu, and C. H. Chan, "A 2-D beam-scanning Bessel launcher for terahertz applications," *IEEE Trans. Antennas Propag.*, vol. 68, no. 8, pp. 5893–5903, Aug. 2020.

[83] G.-B. Wu, Y.-S. Zeng, K. F. Chan, S.-W. Qu, and C. H. Chan, "3-D printed circularly polarized modified Fresnel lens operating at terahertz frequencies," *IEEE Trans. Antennas Propag.*, vol. 67, no. 7, pp. 4429–4437, Jul. 2019.

[84] G. Wu, Y. Zeng, K. F. Chan, S. Qu, and C. Chan, "High-gain circularly polarised lens antenna for terahertz applications," *IEEE Antennas Wireless Propag. Lett.*, vol. 18, no. 5, pp. 921–925, Mar. 2019.

[85] A. C. Paolella, C. D. Fisher, C. Corey, D. Foster, and D. Silva-Saez, "3-D printed millimeter-wave lens systems at 39 GHz," *IEEE Microw. Wireless Compon. Lett.*, vol. 28, no. 6, pp. 464–466, Jun. 2018.

[86] A. Shastri et al., "3D printing of millimetre wave and low-terahertz frequency selective surfaces

using aerosol jet technology," *IEEE Access*, vol. 8, pp. 177341–177350, 2020.

[87] A. H. Allah, G. A. Eyebe, and F. Domingue, "Fully 3D-printed microfluidic sensor using substrate integrated waveguide technology for liquid permittivity characterization," *IEEE Sensors J.*, vol. 22, no. 11, pp. 10541–10550, Jun. 2022.

[88] I. Piekarz, J. Sorocki, M. T. Craton, K. Wincza, S. Gruszczynski, and J. Papapolymerou, "Application of aerosol jet 3-D printing with conductive and nonconductive inks for manufacturing mm-wave circuits," *IEEE Trans. Compon., Packag., Manuf. Technol.*, vol. 9, no. 3, pp. 586–595, Mar. 2019.

[89] M. Abt et al., "Aerosol-printed highly conductive Ag transmission lines for flexible electronic devices," *IEEE Trans. Compon., Packag., Manuf. Technol.*, vol. 8, no. 10, pp. 1838–1844, Oct. 2018.

[90] P. Deffenbaugh, T. Weller, and K. Church, "Fabrication and microwave characterisation of 3-D printed transmission lines," *IEEE Microw. Wireless Compon. Lett.*, vol. 25, no. 12, pp. 823–825, Dec. 2015.

[91] R. A. Ramirez, E. A. Rojas-Nastrucci, and T. M. Weller, "Laser-assisted additive manufacturing of mm-wave lumped passive elements," *IEEE Trans. Microw. Theory Techn.*, vol. 66, no. 12, pp. 5462–5471, Dec. 2018.

[92] D. Sokol, M. Yamada, and J. Nulman, "Design and performance of additively manufactured in-circuit board planar capacitors," *IEEE Trans. Electron Devices*, vol. 68, no. 11, pp. 5747–5752, Nov. 2021.

[93] C. Ding, S. Lu, L. Liu, K. D. T. Ngo, and G.-Q. Lu, "Additive manufacturing of hetero-magnetic coupled inductors," *IEEE Trans. Compon., Packag., Manuf. Technol.*, vol. 11, no. 6, pp. 1028–1034, Jun. 2021.

[94] L. Qian et al., "A narrowband 3-D printed Invar spherical dual-mode filter with high thermal stability for OMUXs," *IEEE Trans. Microw. Theory Techn.*, vol. 70, no. 4, pp. 2165–2173, Apr. 2022.

[95] T. Skaik et al., "A 3-D printed 300 GHz waveguide cavity filter by micro laser sintering," *IEEE Trans. THz Sci. Technol.*, vol. 12, no. 3, pp. 274–281, May 2022.

[96] M. Li, Y. Yang, F. Iacopi, and J. Nulman, "Additively manufactured multi-layer bandpass filter based on vertically integrated composite right and left handed resonator," in *Proc. IEEE Asia–Pacific Microw. Conf. (APMC)*, Nov. 2020, pp. 175–177.

[97] M. Li, Y. Yang, F. Iacopi, M. Yamada, and J. Nulman, "Compact multilayer bandpass filter using low-temperature additively manufacturing solution," *IEEE Trans. Electron Devices*, vol. 68, no. 7, pp. 3163–3169, Jul. 2021.

[98] M. Li, Y. Yang, Y. Zhang, and F. Iacopi, "3-D printed vertically integrated composite right/left-handed transmission line and its applications to microwave circuits," *IEEE Trans. Microw. Theory Techn.*, vol. 72, no. 6, pp. 3311–3321, Jun. 2024.

[99] A. Vallecchi, D. Cadman, W. G. Whittow, J. Vardaxoglou, E. Shamonina, and C. J. Stevens, "3-D printed bandpass filters with coupled vertically extruded split ring resonators," *IEEE Trans. Microwave Theory Techn.*, vol. 67, no. 11, pp. 4341–4352, Nov. 2019.

[100] Z. Zhai, F. Lin, Y. Yang, and H. Sun, "Additively manufactured wideband low-profile bidirectional 2-D beam-scanning antenna using double folded transmitarrays with curved polarizers," *IEEE Trans. Antennas Propag.*, vol. 72, no. 1, pp. 476–486, Jan. 2024.

[101] M. Li, Y. Yang, Y. Zhang, F. Iacopi, S. Ram, and J. Nulman, "A fully integrated conductive and dielectric additive manufacturing technology for microwave circuits and antennas," in *Proc. 50th Eur. Microw. Conf. (EuMC)*, Jan. 2021, pp. 392–395.

[102] M. Li, Y. Yang, F. Iacopi, J. Nulman, and S. Chappel-Ram, "3D-printed low-profile single-substrate multi-metal layer antennas and array with bandwidth enhancement," *IEEE Access*, vol. 8, pp. 217370–217379, 2020.

[103] J. Zhu et al., "Additively manufactured

millimeter-wave dual-band single-polarization shared aperture Fresnel zone plate metalens antenna," *IEEE Trans. Antennas Propag.*, vol. 69, no. 10, pp. 6261–6272, Oct. 2021.

[104] J. Lai and Y. Yang, "A 3D printed terahertz metamaterial lens for beam-steering applications," in *IEEE MTT-S Int. Microw. Symp. Dig.*, Jun. 2023, pp. 692–695.

[105] J. Zhu, M. Li, J. Lai, and Y. Yang, "Multimaterial additively manufactured transmissive spin-decoupled polarization-maintaining metasurfaces," *Laser Photon. Rev.*, vol. 17, no. 12, Dec. 2023, Art. no. 2300433.

[106] J. Zhu, Y. Yang, F. Wang, J. Lai, and M. Li, "3D printed spin-decoupled transmissive metasurfaces based on versatile broadband cross-polarization rotation meta-atom," *Adv. Opt. Mater.*, vol. 11, no. 4, Feb. 2023, Art. no. 2202416.

[107] J. Zhu, Y. Yang, J. Lai, and M. Li, "3-D printed noninterleaved reflective metasurfaces supporting dual-band spin-decoupled quadruplex channel independent beam-shaping with controllable energy distribution," *IEEE Trans. Microw. Theory Techn.*, vol. 72, no. 2, pp. 1196–1205, Feb. 2024.

[108] J. Zhu, Y. Yang, J. Lai, and J. Nulman, "Additively manufactured polarization insensitive broadband transmissive metasurfaces for arbitrary polarization conversion and wavefront shaping," *Adv. Opt. Mater.*, vol. 10, no. 21, Nov. 2022, Art. no. 2200928.

[109] J. Zhu, Y. Yang, N. Hu, S. Liao, and J. Nulman, "Additively manufactured multi-material ultrathin metasurfaces for broadband circular polarisation decoupled beams and orbital angular momentum generation," *ACS Appl. Mater. Interface*, vol. 13, no. 49, pp. 59460–59470, 2021.

[110] J. Kwon, Y. Takeda, R. Shiwaku, S. Tokito, K. Cho, and S. Jung, "Three-dimensional monolithic integration in flexible printed organic transistors," *Nature Commun.*, vol. 10, no. 1, pp. 10–54, Jan. 2019.

[111] M. Zarek, M. Layani, I. Cooperstein, E. Sachyani, D. Cohn, and S. Magdassi, "3D printing of shape memory polymers for flexible electronic devices," *Adv. Mater.*, vol. 28, no. 22, pp. 4449–4454, Jun. 2016.

[112] S. Das, P. Martin, G. Vasilyev, R. Nandi, N. Amdursky, and E. Zussman, "Processable, ion-conducting hydrogel for flexible electronic devices with self-healing capability," *Macromolecules*, vol. 53, no. 24, pp. 11130–11141, Dec. 2020.

[113] S. Zhang et al., "A convenient, low-cost graphene UV-cured additive manufacturing electronic process to achieve flexible sensors," *Chem. Eng. J.*, vol. 451, Jan. 2023, Art. no. 138521.

[114] S. Sundaram, D. S. Kim, M. A. Baldo, R. C. Hayward, and W. Matusik, "3D-printed self-folding electronics," *ACS Appl. Mater. Interface*, vol. 9, no. 37, pp. 32290–32298, Sep. 2017.

[115] G. Chen, Y. Li, M. Bick, and J. Chen, "Smart textiles for electricity generation," *Chem. Rev.*, vol. 120, no. 8, pp. 3668–3720, Apr. 2020.

[116] K. Keum, J. W. Kim, S. Y. Hong, J. G. Son, S. Lee, and J. S. Ha, "Flexible/stretchable supercapacitors with novel functionality for wearable electronics," *Adv. Mater.*, vol. 32, no. 51, Dec. 2020, Art. no. e2002180.

[117] K. Shen, J. Ding, and S. Yang, "3D printing quasi-solid-state asymmetric micro-supercapacitors with ultrahigh areal energy density," *Adv. Energy Mater.*, vol. 8, no. 20, Jul. 2018, Art. no. 1800408.

[118] Y. Ma et al., "Flexible hybrid electronics for digital healthcare," *Adv. Mater.*, vol. 32, no. 15, Apr. 2020, Art. no. e1902062.

[119] J. Wei et al., "Bioinspired 3D printable, self-healable, and stretchable hydrogels with multiple conductivities for skin-like wearable strain sensors," *ACS Appl. Mater. Interface*, vol. 13, no. 2, pp. 2952–2960, Jan. 2021.

[120] Y. Niu et al., "The new generation of soft and wearable electronics for health monitoring in varying environment: From normal to extreme conditions," *Mater. Today*, vol. 41, pp. 219–242,

Dec. 2020.

[121] R. Liu et al., "Shape memory polymers for body motion energy harvesting and self-powered mechanosensing," *Adv. Mater.*, vol. 30, no. 8, Feb. 2018, Art. no. 1705195.

[122] L. Wang, D. Chen, K. Jiang, and G. Shen, "New insights and perspectives into biological materials for flexible electronics," *Chem. Soc. Rev.*, vol. 46, no. 22, pp. 6764–6815, 2017.

[123] D. Yang et al., "3D/4D printed tunable electrical metamaterials with more sophisticated structures," *J. Mater. Chem. C*, vol. 9, no. 36, pp. 12010–12036, 2021.

[124] A. Lendlein and R. Langer, "Biodegradable, elastic shape-memory polymers for potential biomedical applications," *Science*, vol. 296, no. 5573, pp. 1673–1676, May 2002.

[125] Y. Liu, H. Du, L. Liu, and J. Leng, "Shape memory polymers and their composites in aerospace applications: A review," *Smart Mater. Struct.*, vol. 23, no. 2, Feb. 2014, Art. no. 023001.

[126] E. García-Marín, J. L. Masa-Campos, P. Sánchez-Olivares, and J. A. Ruiz-Cruz, "Evaluation of additive manufacturing techniques applied to Ku-band multilayer corporate waveguide antennas," *IEEE Antennas Wireless Propag. Lett.*, vol. 17, no. 11, pp. 2114–2118, Nov. 2018.

[127] M. Ferrando-Rocher, J. I. Herranz-Herruzo, A. Valero-Nogueira, and B. Bernardo-Clemente, "Performance assessment of gap-waveguide array antennas: CNC milling versus three-dimensional printing," *IEEE Antennas Wireless Propag. Lett.*, vol. 17, no. 11, pp. 2056–2060, Nov. 2018.

[128] F. Sun, Y. Li, L. Ge, and J. Wang, "Millimeter-wave magneto-electric dipole antenna array with a self-supporting geometry for time-saving metallic 3-D printing," *IEEE Trans. Antennas Propag.*, vol. 68, no. 12, pp. 7822–7832, Dec. 2020.

[129] J.-M. Poyanco, F. Pizarro, and E. Rajo-Iglesias, "Cost-effective wideband dielectric planar lens antenna for millimeter wave applications," *Sci. Rep.*, vol. 12, p. 4204, Mar. 2022.

[130] J. Persad and S. Rocke, "A survey of 3D printing technologies as applied to printed electronics," *IEEE Access*, vol. 10, pp. 27289–27319, 2022.

[131] Y. Park, I. Yun, W. Chung, W. Park, D. Lee, and J. Park, "High-resolution 3D printing for electronics," *Adv. Sci.*, vol. 9, no. 8, 2022, Art. no. e210462.

[132] *Voxel8 3D Electronics Printer*, Aniwaa, Singapore.

[133] U. Shaukat, E. Rossegger, and S. Schlögl, "A review of multi-material 3D printing of functional materials via vat photopolymerization," *Polymers*, vol. 14, no. 12, p. 2449, Jun. 2022.

[134] H. Chen, L. Guo, W. Zhu, and C. Li, "Recent advances in multi-material 3D printing of functional ceramic devices," *Polymers*, vol. 14, no. 21, p. 4635, Oct. 2022.

[135] S. M. F. Kabir, K. Mathur, and A.-F.-M. Seyam, "A critical review on 3D printed continuous fiber-reinforced composites: History, mechanism, materials and properties," *Compos. Struct.*, vol. 232, Jan. 2020, Art. no. 111476.

[136] R. Kumar and R. Kumar, "3D printing of food materials: A state of art review and future applications," *Mater. Today, Proc.*, vol. 33, pp. 1463–1467, Jan. 2020.

[137] H. Yin, Q. Liang, Y. Duan, J. Fan, and Z. Li, "3D printing of a thermally programmable conformal metasurface," *Adv. Mater. Technol.*, vol. 7, no. 7, Jul. 2022, Art. no. 2101479.

[138] M. Liang, C. Shemelya, E. MacDonald, R. Wicker, and H. Xin, "3-D printed microwave patch antenna via fused deposition method and ultrasonic wire mesh embedding technique," *IEEE Antennas Wireless Propag. Lett.*, vol. 14, pp. 1346–1349, 2015.

[139] E. A. Rojas-Nastrucci, T. Weller, V. L. Aida, F. Cai, and J. Papapolymerou, "A study on 3D-printed coplanar waveguide with meshed and finite ground planes," in *Proc. WAMICON*, Jun. 2014, pp. 1–3.

[140] F. Cai, Y.-H. Chang, K. Wang, C. Zhang, B. Wang, and J. Papapolymerou, "Low-loss 3-D multilayer transmission lines and interconnects fabricated by additive manufacturing technologies," *IEEE Trans. Microw. Theory Techn.*, vol. 64, no. 10, pp. 3208–3216, Oct. 2016.

[141] L. Ivy et al., "Laser-induced graphene pressure sensors manufactured via inkjet PCB printer: Locally producing super-sensitive and cost-effective circular diaphragm pressure gauges," in *Proc. IEEE Int. Conf. Flexible Printable Sensors Syst. (FLEPS)*, Jul. 2022, pp. 1–4.

[142] J. Zhu and Y. Yang, "3-D printed transmission-reflection-integrated metasurface for spin-decoupled full-space quadruplex channels independent phase modulation," *IEEE Trans. Microw. Theory Techn.*, vol. 72, no. 8, pp. 4790–4800, Aug. 2024.

[143] M. Li and Y. Yang, "Single- and multiple-material additively manufactured electronics: A further step from the microwave-to-terahertz regimes," *IEEE Microw. Mag.*, vol. 24, no. 1, pp. 30–45, Jan. 2023.

[144] Y. Yang, "Free-standing printed electronics with direct ink writing," *Nature Electron.*, vol. 7, no. 8, pp. 630–631, Aug. 2024.

[145] S. Ling et al., "Tension-driven three-dimensional printing of free-standing field's metal structures," *Nature Electron.*, vol. 7, no. 8, pp. 671–683, Jul. 2024.

[146] M. Li, J. Liu, Z. Hu, and Y. Yang, "3D broadband FSS with through holes and low profile for UHF and SHF applications," in *Proc. Int. Symp. Antennas Propag. (ISAP)*, Oct. 2022, pp. 443–444.

[147] J.-Y. Lin and Y. Yang, "3D sub-terahertz dual-mode cavity resonator and its application to dual-polarized frequency selective surface," in *Proc. IEEE Asia–Pacific Microw. Conf. (APMC)*, Nov. 2021, pp. 494–496.

[148] Z. Yin, J. Cai, J. Zhu, J. Lai, and Y. Yang, "A 3D printed beam-shaping transmissive metasurface for antenna-in-package applications," in *Proc. IEEE Int. Symp. Radio-Freq. Integr. Technol. (RFIT)*, Aug. 2023, pp. 26–28.

[149] S. W. Kwok et al., "Electrically conductive filament for 3D-printed circuits and sensors," *Appl. Mater. Today*, vol. 9, pp. 167–175, Dec. 2017.

[150] F. Wasserfall, D. Ahlers, N. Hendrich, and J. Zhang, "3D-printable electronics—Integration of SMD placement and wiring into the slicing process for FDM fabrication," in *Proc. Int. Solid Freeform Fabr. Symp.*, Jan. 2016, pp. 1826–1837.

[151] A. Bandyopadhyay and B. Heer, "Additive manufacturing of multi-material structures," *Mater. Sci. Eng. R-Rep.*, vol. 129, pp. 1–16, Jul. 2018.

[152] E. García-Tuñon et al., "Printing in three dimensions with graphene," *Adv. Mater.*, vol. 27, no. 10, pp. 1688–1693, Mar. 2015.

[153] C. Zhang et al., "Additive-free MXene inks and direct printing of micro-supercapacitors," *Nature Commun.*, vol. 10, no. 1, p. 1795, Apr. 2019.

[154] Y. Lin et al., "Printable fabrication of a fully integrated and self-powered sensor system on plastic substrates," *Adv. Mater.*, vol. 31, no. 5, Feb. 2019, Art. no. 1804285.

[155] S.-Y. Wu, C. Yang, W. Hsu, and L. Lin, "3D-printed microelectronics for integrated circuitry and passive wireless sensors," *Microsyst. Nanoeng.*, vol. 1, no. 1, pp. 1–9, Jul. 2015.

[156] S. Ready, G. Whiting, T. Ng, G. Whiting, and T. Ng, "Multi-material 3D printing," in *Proc. NIP Digit. Fabr. Conf.*, vol. 30, Jan. 2014, pp. 120–123.

[157] A. D. Valentine, "Hybrid 3D printing of soft electronics," *Adv. Mater.*, vol. 29, no. 40, Oct. 2017, Art. no. 1703817.

[158] P. I. Deffenbaugh, D. M. Stramel, and K. H. Church, "Increasing the reliability of 3D printing a Wi-Fi sensor device," in *Proc. Int. Symp. Microelectron.*, Oct. 2016, no. 1, pp. 240–244.

[159] J. Li, Y. Wang, J. He, H. Liu, and G. Xiang, "Rapid production of customised electronic systems via multifunctional additive manufacturing technology," in *Proc. IEEE 3rd Int. Conf. Integr. Circuits Microsyst. (ICICM)*, Nov. 2018, pp. 298–301.

[160] G. T. Carranza, U. Robles, C. L. Valle, J. J. Gutierrez, and R. C. Rumpf, "Design and hybrid additive manufacturing of 3-D/volumetric electrical circuits," *IEEE Trans. Compon., Packag., Manuf. Technol.*, vol. 9, no. 6, pp. 1176–1183, Jun. 2019.

[161] B. Subeshan, Y. Baddam, and E. Asmatulu, "Current progress of 4D-printing technology," *Prog. Additive Manuf.*, vol. 6, no. 3, pp. 495–516, Aug. 2021.

[162] S. Joshi et al., "4D printing of materials for the future: Opportunities and challenges," *Appl. Mater. Today*, vol. 18, Mar. 2020, Art. no. 100490.

[163] X. Kuang et al., "Advances in 4D printing: Materials and applications," *Adv. Funct. Mater.*, vol. 29, no. 2, Jan. 2019, Art. no. 1805290.

[164] E. S. Keneth et al., "Untethered magneto-thermal flexible actuators for soft robotics," *Sens. Actuators A, Phys.*, vol. 363, Dec. 2023, Art. no. 114683.

[165] Y. Wang, E. S. Keneth, A. Kamyshny, G. Scalet, F. Auricchio, and S. Magdassi, "4D multimaterial printing of programmable and selective light-activated shape-memory structures with embedded gold nanoparticles," *Adv. Mater. Technol.*, vol. 7, no. 5, May 2022, Art. no. 2101058.

[166] E. Sachyani Keneth et al., "Pre-programmed tri-layer electro-thermal actuators composed of shape memory polymer and carbon nanotubes," *Soft Robot.*, vol. 7, no. 2, pp. 123–129, Apr. 2020.

[167] E. S. Keneth, R. Lieberman, M. Rednor, G. Scalet, F. Auricchio, and S. Magdassi, "Multi-material 3D printed shape memory polymer with tunable melting and glass transition temperature activated by heat or light," *Polymers*, vol. 12, no. 3, pp. 710–722, Mar. 2020.

[168] Y. Dong et al., "4D printed hydrogels: Fabrication, materials, and applications," *Adv. Mater. Technol.*, vol. 5, no. 6, Jun. 2020, Art. no. 2000034.

[169] B. M. B. Dos Santos, G. Littlefair, and S. Singamneni, "From 3D to 4D printing: A review," *Mater. Today Proc.*, Jun. 2023.

[170] S. Wei et al., "Laser powder bed fusion additive manufacturing of NiTi shape memory alloys: A review," *Int. J. Extreme Manuf.*, vol. 5, no. 3, Sep. 2023, Art. no. 032001.

[171] J. Zhan, J. Wu, R. Ma, K. Li, J. Lin, and L. E. Murr, "Tuning the functional properties by laser powder bed fusion with partitioned repetitive laser scanning: Toward editable 4D printing of NiTi alloys," *J. Manuf. Processes*, vol. 101, pp. 1468–1481, Sep. 2023.

[172] J. Leng, X. Lan, Y. Liu, and S. Du, "Shape-memory polymers and their composites: Stimulus methods and applications," *Prog. Mater. Sci.*, vol. 56, no. 7, pp. 1077–1135, Sep. 2011.

[173] H. Chu et al., "4D printing: A review on recent progresses," *Micromachines*, vol. 11, no. 9, p. 796, Aug. 2020.

[174] J. Choi, O.-C. Kwon, W. Jo, H. J. Lee, and M.-W. Moon, "4D printing technology: A review," *3D Printing Additive Manuf.*, vol. 2, no. 4, pp. 159–167, Dec. 2015.

[175] R. Sajjad et al., "A review of 4D printing—Technologies, shape shifting, smart polymer based materials, and biomedical applications," *Adv. Ind. Eng. Polym. Res.*, vol. 7, no. 1, pp. 20–36, Jan. 2024.

[176] W. M. Sokolowski and S. C. Tan, "Advanced self-deployable structures for space applications," *J. Spacecraft Rockets*, vol. 44, no. 4, pp. 750–754, Jul. 2007.

[177] A. Zolfagharian, A. Kaynak, and A. Kouzani, "Closed-loop 4D-printed soft robots," *Mater. Des.*, vol. 188, Mar. 2020, Art. no. 108411.

[178] Y. Tang, B. Dai, B. Su, and Y. Shi, "Recent advances of 4D printing technologies toward soft tactile sensors," *Frontiers Mater.*, vol. 8, Apr. 2021.

[179] A. Zolfagharian, A. Z. Kouzani, S. Y. Khoo, A. A. A. Moghadam, I. Gibson, and A. Kaynak, "Evolution of 3D printed soft actuators," *Sens. Actuators A, Phys.*, vol. 250, pp. 258–272, Oct. 2016.

[180] J. Delaey, P. Dubruel, and S. Van Vlierberghe, "Shape-memory polymers for biomedical

applications," *Adv. Funct. Mater.*, vol. 30, no. 44, 2020, Art. no. 1909047.

[181] K. McLellan, Y.-C. Sun, and H. E. Naguib, "A review of 4D printing: Materials, structures, and designs towards the printing of biomedical wearable devices," *Bioprinting*, vol. 27, Aug. 2022, Art. no. e00217.

[182] *Additive Manufacturing-general Principles-terminology*, document ISO/ASTM 52900:2021(en), 2015.

[183] T. DebRoy et al., "Additive manufacturing of metallic components—Process, structure and properties," *Prog. Mater. Sci.*, vol. 92, pp. 112–224, Mar. 2018.

[184] H. Li, X. Gao, and Y. Luo, "Multi-shape memory polymers achieved by the spatio-assembly of 3D printable thermoplastic building blocks," *Soft Matter*, vol. 12, no. 13, pp. 3226–3233, 2016.

[185] S. Chen, Q. Zhang, and J. Feng, "3D printing of tunable shape memory polymer blends," *J. Mater. Chem. C*, vol. 5, no. 33, pp. 8361–8365, 2017.

[186] X. Wan, L. Luo, Y. Liu, and J. Leng, "Direct ink writing based 4D printing of materials and their applications," *Adv. Sci.*, vol. 7, no. 16, Aug. 2020, Art. no. 2001000.

[187] C. A. Spiegel, M. Hackner, V. P. Bothe, J. P. Spatz, and E. Blasco, "4D printing of shape memory polymers: From macro to micro," *Adv. Funct. Mater.*, vol. 32, no. 51, Dec. 2022, Art. no. 2110580.

[188] Y. Y. C. Choong, S. Maleksaeedi, H. Eng, J. Wei, and P.-C. Su, "4D printing of high performance shape memory polymer using stereolithography," *Mater. Des.*, vol. 126, pp. 219–225, Jul. 2017.

[189] Q. Ge, A. H. Sakhaei, H. Lee, C. K. Dunn, N. X. Fang, and M. L. Dunn, "Multimaterial 4D printing with tailorable shape memory polymers," *Sci. Rep.*, vol. 6, no. 1, p. 31110, Aug. 2016.

[190] A. S. Gladman, E. A. Matsumoto, R. G. Nuzzo, L. Mahadevan, and J. A. Lewis, "Biomimetic 4D printing," *Nature Mater.*, vol. 15, no. 4, pp. 413–418, Apr. 2016.

[191] D. Abolhasani, S. Han, C. VanTyne, N. Kang, and Y. Moon, "Powder bed fusion of two-functional Cu-Al-Ni shape memory alloys utilised for 4D printing," *J. Alloys Compounds*, vol. 922, Nov. 2022, Art. no. 166528.

[192] J. C. Chekotu, R. Goodall, D. Kinahan, and D. Brabazon, "Control of Ni-Ti phase structure, solid-state transformation temperatures and enthalpies via control of L-PBF process parameters," *Mater. Des.*, vol. 218, Jun. 2022, Art. no. 110715.

[193] H. Jiang, R. Xi, X. Li, S. Kustov, J. Van Humbeeck, and X. Wang, "Structure, martensitic transformation, and damping properties of functionally graded NiTi shape memory alloys fabricated by laser powder bed fusion," *Materials*, vol. 15, no. 14, p. 5073, Jul. 2022.

[194] S. Dadbakhsh, M. Speirs, J. Kruth, J. Schrooten, J. Luyten, and J. Van Humbeeck, "Effect of SLM parameters on transformation temperatures of shape memory nickel titanium parts," *Adv. Eng. Mater.*, vol. 16, no. 9, pp. 1140–1146, Sep. 2014.

[195] L. Sun et al., "Stimulus-responsive shape memory materials: A review," *Mater. Des.*, vol. 33, pp. 577–640, Jan. 2012.

[196] X. Wan, Y. He, Y. Liu, and J. Leng, "4D printing of multiple shape memory polymer and nanocomposites with biocompatible, programmable and selectively actuated properties," *Additive Manuf.*, vol. 53, May 2022, Art. no. 102689.

[197] M. Behl and A. Lendlein, "Shape-memory polymers," *Mater. Today Kidlington Eng.*, vol. 10, no. 4, pp. 20–28, Apr. 2007.

[198] W. Huang, Z. Ding, C. Wang, J. Wei, Y. Zhao, and H. Purnawali, "Shape memory materials," *Mater. Today*, vol. 13, no. 7, pp. 54–61, 2010.

[199] A. Lendlein and O. E. C. Gould, "Reprogrammable recovery and actuation behaviour of shape-memory polymers," *Nature Rev. Mater.*, vol. 4, no. 2, pp. 116–133, Jan. 2019.

[200] P. Mather, X. Luo, and I. Rousseau, "Shape memory polymer research," *Annu. Rev. Mater. Res.*,

vol. 39, no. 1, pp. 445–471, Aug. 2009.

[201] I. A. Rousseau, "Challenges of shape memory polymers: A review of the progress toward overcoming SMP's limitations," *Polym. Eng. Sci.*, vol. 48, no. 11, pp. 2075–2089, Nov. 2008.

[202] R. T. Shafranek, S. C. Millik, P. T. Smith, C.-U. Lee, A. J. Boydston, and A. Nelson, "Stimuli-responsive materials in additive manufacturing," *Prog. Polym. Sci.*, vol. 93, pp. 36–67, Jun. 2019.

[203] N. Sabahi, W. Chen, C.-H. Wang, J. J. Kruzic, and X. Li, "A review on additive manufacturing of shape-memory materials for biomedical applications," *JOM*, vol. 72, no. 3, pp. 1229–1253, Mar. 2020.

[204] L. Sun and W. M. Huang, "Nature of the multistage transformation in shape memory alloys upon heating," *Metal Sci. Heat Treatment*, vol. 51, nos. 11–12, pp. 573–578, Nov. 2009.

[205] I. Mihalcz, "Fundamental characteristics and design method for nickel-titanium shape memory alloy," *Periodica Polytechnica Mech. Eng.*, vol. 45, no. 1, pp. 75–86, 2001.

[206] H. Meng and G. Li, "A review of stimuli-responsive shape memory polymer composites," *Polymer*, vol. 54, no. 9, pp. 2199–2221, Apr. 2013.

[207] Q. Zhao, W. Zou, Y. Luo, and T. Xie, "Shape memory polymer network with thermally distinct elasticity and plasticity," *Sci. Adv.*, vol. 2, no. 1, Jan. 2016, Art. no. e1501297.

[208] Q. Zhao, H. J. Qi, and T. Xie, "Recent progress in shape memory polymer: New behavior, enabling materials, and mechanistic understanding," *Prog. Polym. Sci.*, vols. 49–50, pp. 79–120, Oct. 2015.

[209] F. Migneco, Y.-C. Huang, R. K. Birla, and S. J. Hollister, "Poly(glycerol-dodecanoate), a biodegradable polyester for medical devices and tissue engineering scaffolds," *Biomaterials*, vol. 30, no. 33, pp. 6479–6484, Nov. 2009.

[210] A. Garle, S. Kong, U. Ojha, and B. M. Budhlall, "Thermoresponsive semicrystalline poly(ε-caprolactone) networks: Exploiting cross-linking with cinnamoyl moieties to design polymers with tunable shape memory," *ACS Appl. Mater. Interface*, vol. 4, no. 2, pp. 645–657, Feb. 2012.

[211] L. Yue et al., "Cold-programmed shape-morphing structures based on grayscale digital light processing 4D printing," *Nature Commun.*, vol. 14, no. 1, Sep. 2023, Art. no. 1.

[212] J. M. Jani, M. Leary, A. Subic, and M. A. Gibson, "A review of shape memory alloy research, applications and opportunities," *Mater. Des.*, vol. 56, pp. 1078–1113, Apr. 2014.

[213] W. J. Buehler and F. E. Wang, "A summary of recent research on the nitinol alloys and their potential application in ocean engineering," *Ocean Eng.*, vol. 1, no. 1, pp. 105–120, Jul. 1968.

[214] K. Otsuka and X. Ren, "Physical metallurgy of Ti-Ni-based shape memory alloys," *Prog. Mater. Sci.*, vol. 50, no. 5, pp. 511–678, Jul. 2005.

[215] K. C. Atli, I. Karaman, and R. D. Noebe, "Work output of the two-way shape memory effect in $Ti_{50.5}Ni_{24.5}Pd_{25}$ high-temperature shape memory alloy," *Scripta Mater.*, vol. 65, no. 10, pp. 903–906, Nov. 2011.

[216] C. Hayrettin, O. Karakoc, I. Karaman, J. H. Mabe, R. Santamarta, and J. Pons, "Two way shape memory effect in NiTiHf high temperature shape memory alloy tubes," *Acta Mater.*, vol. 163, pp. 1–13, Jan. 2019.

[217] X. Ren and K. Otsuka, "Origin of rubber-like behaviour in metal alloys," *Nature*, vol. 389, no. 6651, pp. 579–582, Oct. 1997.

[218] P. Wu, T. Yu, M. Chen, and D. Hui, "Effect of printing speed and part geometry on the self-deformation behaviors of 4D printed shape memory PLA using FDM," *J. Manuf. Processes*, vol. 84, pp. 1507–1518, Dec. 2022.

[219] C. Ambulo, J. Burroughs, J. Boothby, H. Kim, M. Shankar, and T. Ware, "Four-dimensional printing of liquid crystal elastomers," *ACS Appl. Mater. Interface*, vol. 9, no. 42, pp. 37332–37339, Oct. 2017.

[220] T. van Manen, S. Janbaz, K. M. B. Jansen, and A. A. Zadpoor, "4D printing of reconfigurable

metamaterials and devices," *Commun. Mater.*, vol. 2, no. 1, Jun. 2021, Art. no. 1.

[221] F. Momeni, X. Liu, and J. Ni, "A review of 4D printing," *Mater. Des.*, vol. 122, pp. 42–79, May 2017.

[222] M. Bodaghi, A. R. Damanpack, and W. H. Liao, "Triple shape memory polymers by 4D printing," *Smart Mater. Struct.*, vol. 27, no. 6, May 2018, Art. no. 065010.

[223] J. Zhang et al., "Advances in 4D printed shape memory polymers: From 3D printing, smart excitation, and response to applications," *Adv. Mater. Technol.*, vol. 7, no. 9, Sep. 2022, Art. no. 2101568.

[224] C. Lin et al., "4D-printed biodegradable and remotely controllable shape memory occlusion devices," *Adv. Funct. Mater.*, vol. 29, no. 51, Dec. 2019, Art. no. 1906569.

[225] Q. Ze et al., "Magnetic shape memory polymers with integrated multifunctional shape manipulation," *Adv. Mater.*, vol. 32, no. 4, Jan. 2020, Art. no. 1906657.

[226] X. Wan, F. Zhang, Y. Liu, and J. Leng, "CNT-based electro-responsive shape memory functionalized 3D printed nanocomposites for liquid sensors," *Carbon*, vol. 155, pp. 77–87, Dec. 2019.

[227] Y. S. Alshebly et al., "Bioinspired pattern-driven single-material 4D printing for self-morphing actuators," *Sustainability*, vol. 14, no. 16, p. 10141, Aug. 2022.

[228] A. Zolfagharian, A. Kaynak, S. Y. Khoo, and A. Kouzani, "Pattern-driven 4D printing," *Sens. Actuators A, Phys.*, vol. 274, pp. 231–243, May 2018.

[229] D. Kim, I. Ferretto, C. Leinenbach, and W. Lee, "3D and 4D printing of complex structures of Fe–Mn–Si-based shape memory alloy using laser powder bed fusion," *Adv. Mater. Interface*, vol. 9, no. 13, May 2022, Art. no. 2200171.

[230] M. A. Wagner, J. L. Ocana-Pujol, A. Hadian, F. Clemens, and R. Spolenak, "Filament extrusion-based additive manufacturing of NiTi shape memory alloys," *Mater. Des.*, vol. 225, Jan. 2023, Art. no. 111418.

[231] Y. Cao et al., "Large tunable elastocaloric effect in additively manufactured Ni–Ti shape memory alloys," *Acta Mater.*, vol. 194, pp. 178–189, Aug. 2020.

[232] W. Chen, Q. Yang, S. Huang, S. Huang, J. J. Kruzic, and X. Li, "Laser power modulated microstructure evolution, phase transformation and mechanical properties in NiTi fabricated by laser powder bed fusion," *J. Alloys Compounds*, vol. 861, Apr. 2021, Art. no. 157959.

[233] W. J. Lee, B. Weber, and C. Leinenbach, "Recovery stress formation in a restrained Fe–Mn–Si-based shape memory alloy used for prestressing or mechanical joining," *Construct. Building Mater.*, vol. 95, pp. 600–610, Oct. 2015.

[234] D. Kim, I. Ferretto, W. Kim, C. Leinenbach, and W. Lee, "Effect of post-heat treatment conditions on shape memory property in 4D printed Fe–17Mn–5Si–10Cr–4Ni shape memory alloy," *Mater. Sci. Eng., A*, vol. 852, Sep. 2022, Art. no. 143689.

[235] M. Mohri, I. Ferretto, H. Khodaverdi, C. Leinenbach, and E. Ghafoori, "Influence of thermomechanical treatment on the shape memory effect and pseudoelasticity behavior of conventional and additive manufactured Fe–Mn–Si–Cr–Ni-(V,C) shape memory alloys," *J. Mater. Res. Technol.*, vol. 24, pp. 5922–5933, May 2023.

[236] I. F. Ituarte, F. Nilsén, V. K. Nadimpalli, M. Salmi, J. Lehtonen, and S.-P. Hannula, "Towards the additive manufacturing of Ni-Mn-Ga complex devices with magnetic field induced strain," *Additive Manuf.*, vol. 49, Jan. 2022, Art. no. 102485.

[237] J. Zhang, B. Song, L. Yang, R. Liu, L. Zhang, and Y. Shi, "Microstructure evolution and mechanical properties of TiB/Ti_6Al_4V gradient-material lattice structure fabricated by laser powder bed fusion," *Compos. B, Eng.*, vol. 202, Dec. 2020, Art. no. 108417.

[238] X. Wang et al., "Effect of process parameters on the phase transformation behavior and tensile properties of NiTi shape memory alloys fabricated by selective laser melting," *Additive Manuf.*, vol. 36, Dec. 2020, Art. no. 101545.

[239] S. Saedi, A. S. Turabi, M. T. Andani, C. Haberland, M. Elahinia, and H. Karaca, "Thermomechanical characterization of Ni-rich NiTi fabricated by selective laser melting," *Smart Mater. Struct.*, vol. 25, no. 3, Feb. 2016, Art. no. 035005.

[240] M. Elahinia, N. S. Moghaddam, M. T. Andani, A. Amerinatanzi, B. A. Bimber, and R. F. Hamilton, "Fabrication of NiTi through additive manufacturing: A review," *Prog. Mater. Sci.*, vol. 83, pp. 630–663, Oct. 2016.

[241] J. K. Allafi, X. Ren, and G. Eggeler, "The mechanism of multistage martensitic transformations in aged Ni-rich NiTi shape memory alloys," *Acta Mater.*, vol. 50, no. 4, pp. 793–803, Feb. 2002.

[242] W. Guo et al., "Study on the junction zone of NiTi shape memory alloy produced by selective laser melting via a stripe scanning strategy," *Intermetallics*, vol. 126, Nov. 2020, Art. no. 106947.

[243] N. S. Moghaddam et al., "Anisotropic tensile and actuation properties of NiTi fabricated with selective laser melting," *Mater. Sci. Eng., A*, vol. 724, pp. 220–230, May 2018.

[244] J. Lou, H. He, Y. Li, C. Zhu, Z. Chen, and C. Liu, "Effects of high o contents on the microstructure, phase-transformation behaviour, and shape-recovery properties of porous NiTi-based shape-memory alloys," *Mater. Des.*, vol. 106, pp. 37–44, Sep. 2016.

[245] M. Mohammadi et al., "Sustainable robotic joints 4D printing with variable stiffness using reinforcement learning," *Robot. Comput.-Integr. Manuf.*, vol. 85, Feb. 2024, Art. no. 102636.

[246] H. Soleimanzadeh, B. Rolfe, M. Bodaghi, M. Jamalabadi, X. Zhang, and A. Zolfagharian, "Sustainable robots 4D printing," *Adv. Sustain. Syst.*, vol. 7, no. 12, Sep. 2023, Art. no. 2300289.

[247] H. Jeong, E. Park, and S. Lim, "Frequency memorizing shape morphing microstrip monopole antenna using hybrid programmable 3-dimensional printing," *Additive Manuf.*, vol. 58, Oct. 2022, Art. no. 102988.

[248] S. I. H. Shah, A. Sarkar, R. Phon, and S. Lim, "Two-dimensional electromechanically transformable metasurface with beam scanning capability using four independently controllable shape memory alloy axes," *Adv. Opt. Mater.*, vol. 8, no. 22, Nov. 2020, Art. no. 2001180.

[249] R. Phon, Y. Kim, E. Park, H. Jeong, and S. Lim, "Mechanical and self-deformable spatial modulation beam steering and splitting metasurface," *Adv. Opt. Mater.*, vol. 9, no. 19, Oct. 2021, Art. no. 2100821.

[250] S. Park, E. Park, M. Lee, and S. Lim, "Shape-morphing antenna array by 4D-printed multimaterial miura origami," *ACS Appl. Mater. Inter.*, vol. 15, no. 42, pp. 49843–49853, Oct. 2023.

[251] H. Jeong, E. Park, and S. Lim, "Four-dimensional printed shape memory metasurface to memorise absorption and reflection functions," *ACS Appl. Mater. Interface*, vol. 13, no. 49, pp. 59487–59496, Dec. 2021.

[252] T. Cersoli et al., "4D printed shape memory polymers: Morphology and fabrication of a functional antenna," *Recent Prog. Mater.*, vol. 4, no. 2, Apr. 2022, Art. no. 2.

[253] J. Kimionis, M. Isakov, B. S. Koh, A. Georgiadis, and M. M. Tentzeris, "3D-printed origami packaging with inkjet-printed antennas for RF harvesting sensors," *IEEE Trans. Microw. Theory Techn.*, vol. 63, no. 12, pp. 4521–4532, Dec. 2015.

[254] R. Bahr, A. Nauroze, W. Su, and M. M. Tentzeris, "Self-actuating 3D printed packaging for deployable antennas," in *Proc. IEEE 67th Electron. Compon. Technol. Conf. (ECTC)*, May 2017, pp. 1425–1430.

[255] S. I. H. Shah, S. Bashir, M. Ashfaq, A. Altaf, and H. Rmili, "Lightweight and low-cost deployable origami antennas—A review," *IEEE Access*, vol. 9, pp. 86429–86448, 2021.

[256] M. Rafiee, R. Farahani, and D. Therriault, "Multi-material 3D and 4D printing: A survey," *Adv. Sci.*, vol. 7, no. 12, 2020, Art. no. 1902307.

[257] L. Jiang et al., "Temperature-adaptive reconfigurable chiral metamaterial for tailoring circular dichroism based on shape memory alloy," *Mater. Design*, vol. 225, Jan. 2023, Art. no. 111496.

[258] Q. Liang, Z. Li, J. Xu, Y. Duan, Z. Yang, and D. Li, "A 4D-printed electromagnetic cloaking and illusion function convertible metasurface," *Adv. Mater. Technol.*, vol. 8, no. 23, Mar. 2023, Art. no. 2202020.

[259] Y. Cui, S. A. Nauroze, and M. M. Tentzeris, "Novel 3D-printed reconfigurable origami frequency selective surfaces with flexible inkjet-printed conductor traces," in *IEEE MTT-S Int. Microw. Symp. Dig.*, Jun. 2019, pp. 1367–1370.

[260] Y. Cui, S. A. Nauroze, R. Bahr, and M. M. Tentzeris, "A novel additively 4D printed origami-inspired tunable multi-layer frequency selective surface for mm-wave IoT, RFID, WSN, 5G, and smart city applications," in *IEEE MTT-S Int. Microw. Symp. Dig.*, Jun. 2021, pp. 86–89.

[261] Y. Kim, R. Phon, H. Jeong, Y. Kim, and S. Lim, "Thermal spiral inductor using 3D printed shape memory Kirigami," *Sci. Rep.*, vol. 12, no. 1, p. 22246, Dec. 2022.

[262] J. N. Rodriguez, C. Zhu, E. B. Duoss, T. S. Wilson, C. M. Spadaccini, and J. P Lewicki, "Shape-morphing composites with designed micro-architectures," *Sci. Rep.*, vol. 6, pp. 27933–27943, Jun. 2016.

[263] H. Wei et al., "Direct 3D printing of hybrid nanofiber-based nanocomposites for highly conductive and shape memory applications," *ACS Appl. Mater. Interface*, vol. 11, no. 27, pp. 24523–24532, Jul. 2019.

[264] J. Costantine, Y. Tawk, S. E. Barbin, and C. G. Christodoulou, "Reconfigurable antennas: Design and applications," *Proc. IEEE*, vol. 103, no. 3, pp. 424–437, Mar. 2015, doi: 10.1109/JPROC.2015.2396000.

[265] K. Hu, Y. Zhou, S. K. Sitaraman, and M. M. Tentzeris, "Additively manufactured flexible on-package phased array antennas for 5G/mmWave wearable and conformal digital twin and massive MIMO applications," *Sci. Rep.*, vol. 13, no. 1, Aug. 2023.

[266] K. Hu, Y. Zhou, S. K. Sitaraman, and M. M. Tentzeris, "Flexible/conformal inkjet-printed 3-D 'Ramp' interconnects for 5G/mmWave system-on-package designs and wearable applications," *IEEE Trans. Compon., Packag., Manuf. Technol.*, vol. 14, no. 8, pp. 1329–1336, Aug. 2024.

[267] Y. Cui, A. Eid, and M. M. Tentzeris, "A 3D-printed mm-wave deployable origami dielectric reflectarray antenna," in *Proc. IEEE Int. Symp. Antennas Propag. North Amer. Radio Sci. Meeting*, Montreal, QC, Canada, Jul. 2020, pp. 1679–1680.

[268] Y. Cui, S. A. Nauroze, R. Bahr, and E. M. Tentzeris, "3D printed one-shot deployable flexible 'Kirigami' dielectric reflectarray antenna for mm-wave applications," in *IEEE MTT-S Int. Microw. Symp. Dig.*, Los Angeles, CA, USA, Aug. 2020, pp. 1164–1167.

[269] Y. Cui, R. Bahr, S. A. Nauroze, T. Cheng, T. S. Almoneef, and M. M. Tentzeris, "3D printed 'Kirigami'-inspired deployable bi-focal beam-scanning dielectric reflectarray antenna for mm-wave applications," *IEEE Trans. Antennas Propag.*, vol. 70, no. 9, pp. 7683–7690, Sep. 2022.

[270] Y. Cui, R. Bahr, S. V. Rijs, and M. Tentzeris, "A novel 4-DOF wide-range tunable frequency selective surface using an origami 'Eggbox' structure," *Int. J. Microw. Wireless Technol.*, vol. 13, no. 7, pp. 727–733, Sep. 2021.

[271] Y. Cui, S. Van Rijs, R. Bahr, and M. Tentzeris, "A novel fully inkjet printed dual-polarization broadband tuneable FSS using origami 'Eggbox' structure," in *Proc. 50th Eur. Microw. Conf. (EuMC)*, Jan. 2021, pp. 760–763.

[272] S. A. Nauroze and M. M. Tentzeris, "A thermally actuated fully inkjet-printed origami-inspired multilayer frequency selective surface with continuous-range tunability using polyester-based substrates," *IEEE Trans. Microw. Theory Techn.*, vol. 67, no. 12, pp. 4944–4954, Dec. 2019.

[273] S. A. Nauroze and M. M. Tentzeris, "Fully inkjet-printed tunable hybrid n-Ripple Miura (n-RiM) frequency selective surfaces," in *Proc. IEEE Int. Symp. Antennas Propag. USNC-URSI Radio Sci. Meeting*, Atlanta, GA, USA, 2019, pp. 2019–2020.

[274] H. A. Jamal, C. Hu, N. Wille, K. Zeng, and M. M. Tentzeris, "Beyond planar: An additively manufactured, origami-inspired shape-changing, and RFIC-based phased array for near-limitless radiation pattern reconfigurability in 5G/mm-wave applications," *IEEE Microw. Wireless Technol. Lett.*, vol. 34, no. 6, pp. 841–844, Jun. 2024.

[275] A. K. Mishra, N. E. Russo, H. S. An, C. L. Zekios, S. V. Georgakopoulos, and R. F. Shepherd, "Robotic antennas using liquid metal origami," *Adv. Intell. Syst.*, vol. 6, no. 8, Aug. 2024.

[276] M. Hamza, C. L. Zekios, and S. V. Georgakopoulos, "A thick origami reconfigurable and packable patch array with enhanced beam steering," *IEEE Trans. Antennas Propag.*, vol. 68, no. 5, pp. 3653–3663, May 2020.

[277] X. He and M. M. Tentzeris, "In-package additively manufactured sensors for bend prediction and calibration of flexible phased arrays and flexible hybrid electronics," in *IEEE MTT-S Int. Microw. Symp. Dig.*, Atlanta, GA, USA, Jun. 2021, pp. 327–330.

[278] M. Joshi, K. Hu, C. A. Lynch, Y. Cui, G. Soto-Valle, and M. M. Tentzeris, "Computer vision enabled calibration of additively manufactured conformal phased arrays utilizing 3-D depth sensing camera," *IEEE Trans. Microw. Theory Techn.*, early access, May 9, 2024, doi: 10.1109/TMTT.2024.3396412.

[279] K. Hu, G. Soto–Valle, Y. Cui, and M. M. Tentzeris, "Flexible and scalable additively manufactured tile-based phased arrays for satellite communication and 50 mm wave applications," in *IEEE MTT-S Int. Microw. Symp. Dig.*, Denver, CO, USA, Jun. 2022, pp. 691–694.

[280] L. Yang, A. Rida, R. Vyas, and M. M. Tentzeris, "RFID tag and RF structures on a paper substrate using inkjet-printing technology," *IEEE Trans. Microw. Theory Techn.*, vol. 55, no. 12, pp. 2894–2901, Dec. 2007.

[281] A. Rida, L. Yang, R. Vyas, and M. M. Tentzeris, "Conductive inkjet-printed antennas on flexible low-cost paper-based substrates for RFID and WSN applications," *IEEE Antennas Propag. Mag.*, vol. 51, no. 3, pp. 13–23, Jun. 2009.

[282] L. Yang, R. Zhang, D. Staiculescu, C. P Wong, and M. M. Tentzeris, "A novel conformal RFID-enabled module utilizing inkjet-printed antennas and carbon nanotubes for gas-detection applications," *IEEE Antennas Wireless Propag. Lett.*, vol. 8, pp. 653–656, 2009.

[283] J. Bito, R. Bahr, J. G. Hester, S. A. Nauroze, A. Georgiadis, and M. M. Tentzeris, "A novel solar and electromagnetic energy harvesting system with a 3-D printed package for energy efficient Internet-of-Things wireless sensors," *IEEE Trans. Microw. Theory Techn.*, vol. 65, no. 5, pp. 1831–1842, May 2017.

[284] Z. Wang et al., "A magnetic soft robot with multimodal sensing capability by multimaterial direct ink writing," *Additive Manuf.*, vol. 61, Jan. 2023, Art. no. 103320.

[285] M. A. S. R. Saadi et al., "Direct ink writing: A 3D printing technology for diverse materials," *Adv. Mater.*, vol. 34, no. 28, Jul. 2022, Art. no. 2108855.
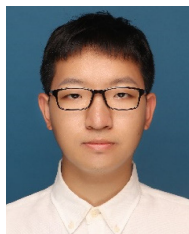
ABOUT THE AUTHORS

Yang Yang (Senior Member, IEEE) was born in Bayan Nur, Inner Mongolia, China. He received the Ph.D. degree in electronic engineering from the Department of Electrical and Computer Systems Engineering, Monash University, Clayton, Australia, in 2013.
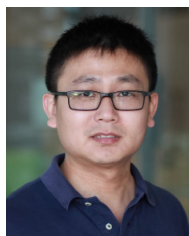
He served as a GSP Engineer at Rain Bird Australia from July 2012 to April 2015. He then joined Macquarie University as a Senior Postdoctoral Research Associate in April 2015. In 2016, he moved to the State Key Laboratory of Terahertz and Millimeter Waves at City University of Hong Kong. Later that year, in December 2016, he joined the University of Technology Sydney (UTS), where he currently holds the position of Associate Professor and leads the 3D Millimetre-Wave and Terahertz Circuits and Antennas group at UTS Tech Laboratory. His research focuses on intelligent radio frequency (RF) materials and additive manufacturing techniques for developing 3D millimetre-wave and terahertz devices, radio frequency integrated circuits (RFICs), and metasurfaces, with applications in 5G/6G wireless communications, CubeSat technologies, and biomedical engineering.

Dr. Yang has been recognised in Stanford/Elsevier's Top 2% Scientist Rankings for five consecutive years, from 2019 to 2023. He has over 260 international publications in microwave, millimetre-wave and terahertz circuits and antennas. In 2022, he received the Linkage Infrastructure, Equipment and Facilities (LIEF) Award funded by the Australian Research Council to establish the national laboratory of the Australian 3D Terahertz Beam Measurement Platform (500 GHz). He is a current Associate Editor of IEEE Transactions on Microwave Theory and Techniques, Associate Editor of IEEE Transactions on Materials for Electron Devices, Associate Editor of IEEE Microwave and Wireless Technology Letters, Guest Editor of Proceedings of the IEEE (Special Session in Additively Manufactured Electronic Components in Multi-Material 3D and 4D Printing) and Area Editor of *Microwave Optical Technology Letters*. He was the Associate Editor of IEEE Access from 2018 to 2022 and a Guest Editor of IEEE Antennas and Wireless Propagation Letters in 2022. He is the current Chair of the IEEE NSW AP-S/MTT-S Joint Chapter and received the 2022 Outstanding IEEE MTT-S Chapter Award and 2023 Outstanding IEEE AP-S Chapter Award. He is the Founder and Inaugural Chair of the IEEE MTT-S Technical Committee Microwave Materials and Processing Technologies (TC-17), Vice Chair of the IEEE MTT-S Education Committee and Vice Chair of the IEEE NSW Electron Device Society.

Xuyi Zhu (Student Member, IEEE) was born in Xuzhou, China. He received the B.E. degree from Shenyang Aerospace University, Shenyang, China, in 2016, the M.S. degree in radio physics from Sichuan University, Chengdu, China, in 2021, where he is currently pursuing the Ph.D. degree at the College of Electronics and Information Engineering.

His research interests include millimeter-wave antenna arrays, reflector antennas, lens antennas, metasurface, and 3D/4D printing technologies for RF devices.

Hani Al Jamal (Graduate Student Member, IEEE) received the B.E. degree (Hons.) in electrical and computer engineering from American University of Beirut, Beirut, Lebanon, and a minor in applied mathematics in 2022. He is currently pursuing the Ph.D. degree in electrical and computer engineering at Georgia Institute of Technology, Atlanta, GA, USA.

He is currently a Research Assistant with the ATHENA Research Group, Georgia Institute of Technology, where he is involved in utilizing additive manufacturing techniques to design highly integrated, conformal, and morphing RF front-end circuits, antennas, and packaging up to mm-wave frequencies.

Mr. Jamal was a recipient of the 2024 IEEE MTT-S IMS Best Student Paper Award.

Xiaojing Lv (Member, IEEE) received the Doctorate degree in electrical and electronic engineering from the University of Adelaide, South Australia, in 2021.
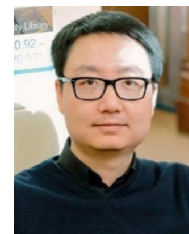
He is currently a Postdoctoral Research Fellow at the Wireless Communications and Networking Laboratory, Tech Laboratory, and a Lecturer at the School of Electrical and Data Engineering, University of Technology Sydney. His research focuses on computational electromagnetics, advanced metamaterial structures, frequency-selective surface filters, antenna arrays, CubeSat antennas, and multi-material additive manufacturing.

Dr. Lv was awarded the Australian Government's Research Training Program Scholarship from 2017 to 2021 and won First Place in the Early Career Paper Competition at the IEEE MTT-S International Microwave Symposium (IMS) in 2024.

Zhiwei Yin (Graduate Student Member, IEEE) was born in Nantong, Jiangsu, China, in 1995. He received the B.Sc. and M.S degrees from Nantong University, Nantong, in 2017 and 2020, respectively. He is currently pursuing the Ph.D. degree at the Faculty of Engineering and Information Technology, University of Technology Sydney (UTS), Sydney, NSW, Australia.

From 2017 to 2018, he worked on Base Station Antenna Research and Development (BSA Research and Development) at COMMSCOPE. His current research interests include couplers, phase shifters, power dividers, radio frequency integrated circuit (RFIC), multi-beam antenna, and 3-D printing technology.

Kexin Hu (Student Member, IEEE) received the B.S. degree in electrical engineering from Nanjing University of Aeronautics and Astronautics, Nanjing, China, in 2017, and the M.S. degree in electrical and computer engineering from The Ohio State University, Columbus, OH, USA, in 2020. She is currently pursuing the Ph.D. degree in electrical and computer engineering at Georgia Institute of Technology, Atlanta, GA, USA, under the supervision of Prof. M. Tentzeris at the ATHENA Research Laboratory.

Her main research interests include utilizing additive manufacturing techniques to enable low-cost and scalable flexible hybrid electronics, heterogeneous packaging, and phased arrays for 5G and mmWave applications.

Marvin Joshi (Graduate Student Member, IEEE) received the B.S. and M.S. degrees in electrical engineering from The University of Tennessee, Knoxville, TN, USA, in 2020 and 2022, respectively. He is currently pursuing the Ph.D. degree in electrical engineering at Georgia Institute of Technology, Atlanta, GA, USA.

He is also a third-year Research Assistant with the ATHENA Laboratory, Georgia Institute of Technology, under the supervision of Prof. M. Tentzeris. His current research interests include the integration of RADAR and artificial intelligence/machine learning with RF modules, specifically mmIDs for localization and tracking applications.

Nathan Wille (Member, IEEE) received the B.S. degree in electrical engineering from the University of Wisconsin - Madison, Madison, WI, USA, in 2022.

From August 2022 to May 2024, he was a Research Assistant with ATHENA Research Group, Georgia Institute of Technology, while earning his M.S. degree in electrical engineering. As a Research Assistant, he used additive manufacturing workflows to develop and fabricate reconfigurable RF structures on 3D packages, with an emphasis on foldable interconnect design for 3D foldable RF systems. He is currently works as an Associate Systems Engineer at Northrop Grumman Corporation.

Mengze Li (Member, IEEE) was born in Hunan, China, in 1994. She received the B.Eng. degree in electrical engineering and automation from Hunan University, Hunan, in 2015, the M.Eng. degree in electronic field and microwave technology from Xiamen University, Xiamen, China, in 2018, and the Ph.D. degree from the Faculty of Engineering and Information Technology, University of Technology Sydney (UTS), Sydney, NSW, Australia, in 2023.

From 2017 to 2018, she was a Visiting Student with the Faculty of Engineering and Information Technology, University of Technology Sydney. She is currently a Lecturer with the School of Microelectronics (School of Integrated Circuits), Nanjing University of Science and Technology, Nanjing, China. Her current research interests include microstrip filters, multiplexers, power dividers, radio frequency integrated circuits (RFIC), reflectarrays, low-temperature co-fired ceramic (LTCC) technology, and 3-D printing technology.

Bing Zhang (Senior Member, IEEE) was born in Taiyuan, China. He received the B.E. degree in electrical and electronic engineering from the Civil Aviation University of China, Tianjin, China, in 2004, the M.E. degree in electrical and electronic engineering from Shanxi University, Taiyuan, China, in 2008, and the Ph.D. degree in electrical and electronic engineering from Nanyang Technological University, Singapore, in 2012.
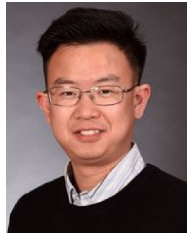
He was a Visiting Scholar with the University of Nice Sophia Antipolis, Nice, France, in May 2012, and a Visiting Scientist with Telecom Bretagne, Brest, France, in November 2014 and April 2015. He was a Postdoctoral Researcher with the Microwave Electronics Laboratory, Department of Microtechnology and Nanoscience, Chalmers University of Technology, Gothenburg, Sweden, from November 2012 to October 2015. He was a Research Fellow with the Department of Electrical and Computer Engineering, National University of Singapore from 2016 to 2017. He joined the College of Electronics and Information Engineering, Sichuan University, as a Full Professor in 2017. His research interests include design and codesign of RF passive and active devices, mmWave and THz antennas, packaging of mmWave and THz devices, Antenna-in-Package, 3-D printing technologies for millimeter-wave and THz applications, and wireless power transfer.

Dr. Zhang is the recipient of the Best Student Paper Award in APCAP 2012, the Young Scientist Award of URSI Commission B in 2013, and the APMC2019 Prize in Antennas.

Zhen Luo received the Ph.D. degree in mechanical engineering from the National Engineering Research Center for CAD, Huazhong University of Science & Technology, Wuhan, China, in 2005.

He has held academic positions at prominent institutions including Shanghai Jiao-Tong University, the Chinese University of Hong Kong, the University of Sydney, the University of New South Wales, and the University of Technology Sydney (UTS). He has been an Associate Professor with the School of Mechanical Engineering at UTS since 2017, where he leads the Advanced Metacomposite Materials & Structures (AMMS) research group. His interdisciplinary work focuses on advanced engineering materials and structures, particularly in aerospace and space. His research interests include integrates numerical simulation, design optimization and additive manufacturing techniques, with applications in electromagnetic, elastic, acoustic, and thermal absorbers and cloaking devices. Especially. He has published 252 peer-reviewed research articles, including 146 papers published in JCR Q1 journals, attracted over 8 200 citations with an h-index of 52 (Google Scholar). He has secured $6 million in research funding, including five ARC Discovery Projects (Australian Research Council), and has successfully engaged with government and industry stakeholders.

Dr. Luo is an internationally recognized research scientist in computational materials design through topological optimization. His accolades, including the World's Top 2% Research Scientists (Stanford University, since 2019), ScholarGPS Highly Ranked Scholar (Top 0.05% scholars worldwide, 2017-2022, # 6 Topology Optimization and #84 Mathematical Optimization) and the IAAM Scientist Award (2020), as well as his recent appointments to the ARC Selection Advisory Committee (NIDG, 2024-2026) and the ARC Expert Panel (ICAS), underscore his international reputation, impact, and leadership in research. He holds editorial roles in five international journals, including Structural Multidisciplinary Optimization (JCR Q1), Frontiers in Bioengineering and Biotechnology - Biomechanics (JCR Q1), and Applied Sciences (JCR Q1). He is also co-chair of the 6th International Conference on Materials Science and Manufacturing Engineering (MSME 2025) and general chair of the 1st International Conference on Design and Manufacturing in Advanced Materials and Structures (DMAMS 2025). He was selected as a Fellow of the International Association of Advanced Materials (IAAM) in 2023. He is also an active member of several esteemed professional societies, including the International Association of Computational Mechanics (IACM), the International Society for Structural and Multidisciplinary Optimization (ISSMO), and the American Society of Mechanical Engineers (ASME).

Shlomo Magdassi is a professor at The Hebrew University of Jerusalem's Institute of Chemistry. His research centers on micro and nanomaterials, with a focus on their applications in functional 2D and 3D printing, printed electronics and soft robotics. Over the course of his career, he has published more than 360 papers, edited four books, and holds approximately 300 patents and applications. Besides publications, his research outcome includes the creation of numerous commercial activities, including start-up companies, licensing agreements, and worldwide sales.

Dr. Magdassi recognition of his contributions, he was awarded the 2022 Johann Gutenberg Prize by the Society for Imaging Science and Technology, The Israel Chemical Society Award for Outstanding Scientist in 2024, and he is also a Fellow of the National Academy of Inventors.

Manos Tentzeris (Fellow, IEEE) received the Diploma degree (Hons.) in electrical and computer engineering from the National Technical University of Athens, Athens, Greece, and the M.S. and Ph.D. degrees in electrical engineering and computer science from the University of Michigan, Ann Arbor, MI, USA, in 1993 and 1998, respectively.

He was a Visiting Professor with the Technical University of Munich, Munich, Germany, in 2002, GTRI-Ireland, Athlone, Ireland, in 2009, and LAASCNRS, Toulouse, France, in 2010, and a Humboldt Guest Professor with FAU, Nuremberg, Germany, in 2019. He is currently the Ed and Pat Joy Chair Professor with the School of Electrical and Computer Engineering, Georgia Institute of Technology, Atlanta, GA, USA, where he heads the ATHENA Research Group (20 researchers). He was the Head of the GT ECE Electromagnetics Technical Interest Group, the Georgia Electronic Design Center Associate Director of RFID/Sensors Research, the Georgia Institute of Technology NSF-Packaging Research Center Associate Director of RF Research, and the RF Alliance Leader. He has helped develop academic programs in 3-D/inkjet-printed RF electronics and modules, fexible electronics, origami and morphing electromagnetics, highly integrated/multilayer packaging for RF, millimeter-wave, sub-THz, and wireless applications using ceramic and organic fexible materials, paper-based RFIDs and sensors, wireless sensors and biosensors, wearable electronics, energy harvesting and wireless power transfer, nanotechnology applications in RF, and SOP-integrated (UWB, multiband, mmW, and conformal) antennas. He has authored more than 850 papers in refereed journals and conference proceedings, seven books, and 26 book chapters.

Dr. Tentzeris is a member of the URSI-Commission D and the MTT-15 Committee, an Associate Member of EuMA, a member of the Technical Chamber of Greece, and a Fellow of the Electromagnetic Academy, He was a recipient/co-recipient of the 2024 IEEE MTT-S IMS Best Student Paper Award, the 2024 Georgia Tech Outstanding Achievement in Research Innovation Award, the 2023 Proceedings of IEEE Best Paper Award, the 2022 Georgia Tech Outstanding Doctoral Thesis Advisor Award, the 2021 IEEE Antennas and Propagation Symposium (APS) Best Student Paper Award, the 2019 Humboldt Research Prize, the 2017 Georgia Institute of Technology Outstanding Achievement in Research Program Development Award, the 2016 Bell Labs Award Competition Third Prize, the 2015 IET Microwaves, Antennas, and Propagation Premium Award, the 2014 Georgia Institute of Technology ECE Distinguished Faculty Achievement Award, the 2014 IEEE RFID-TA Best Student Paper Award, the 2013 IET Microwaves, Antennas and Propagation Premium Award, the 2012 FiDiPro Award in Finland, the iCMG Architecture Award of Excellence, the 2010 IEEE Antennas and Propagation Society Piergiorgio L. E. Uslenghi Letters Prize Paper Award, the 2011 International Workshop on Structural Health Monitoring Best Student Paper Award, the 2010 Georgia Institute of Technology Senior Faculty Outstanding Undergraduate Research Mentor Award, the 2009 IEEE Transactions on Components and Packaging Technologies Best Paper Award, the 2009 E. T. S. Walton Award from the Irish Science Foundation, the 2007 IEEE AP-S Symposium Best Student Paper Award, the 2007 IEEE MTT-S IMS Third Best Student Paper Award, the 2007 ISAP 2007 Poster Presentation Award, the 2006 IEEE MTT-S Outstanding Young Engineer Award, the 2006 Asia-Pacific Microwave Conference Award, the 2004 IEEE Transactions on Advanced Packaging Commendable Paper Award, the 2003 NASA Godfrey "Art" Anzic Collaborative Distinguished Publication Award, the 2003 IBC International Educator of the Year Award, the 2003 IEEE CPMT Outstanding Young Engineer Award, the 2002 International Conference on Microwave and Millimeter-Wave Technology Best Paper Award (Beijing, China), the 2002 Georgia Institute of Technology–ECE Outstanding Junior Faculty Award, the 2001 ACES Conference Best Paper Award, the 2000 NSF CAREER Award, and the 1997 Best Paper Award of the International Hybrid Microelectronics and Packaging Society. He was the General Co-Chair of the 2023 IEEE Wireless Power Transfer Technology Conference and Expo (WPTCE) in San Diego and the 2019 IEEE APS Symposium in Atlanta. He was the TPC Chair of the IEEE MTT-S IMS 2008 Symposium and the Chair of the 2005 IEEE CEM-TD Workshop. He is the Vice-Chair of the RF Technical Committee (TC16) of the IEEE CPMT Society. He is the Founder and the Chair of the RFID Technical Committee (TC24) of the IEEE MTT-S and the Secretary/Treasurer of the IEEE C-RFID. He has served as an Associate Editor for IEEE Transactions on Microwave Theory and Techniques, IEEE Transactions on Advanced Packaging, and the *International Journal on Antennas and Propagation*. He has given more than 150 invited talks to various universities and companies all over the world. He is currently IEEE EPS Distinguished Lecturer. He has served as one of the IEEE MTT-S Distinguished Microwave Lecturers and as one of the IEEE CRFID Distinguished Lecturers.